Development of Burr Prediction System for End Milling

July 2015

KRUY, Sothea

A Thesis for the Degree of Ph.D. in Engineering

Development of Burr Prediction System for End Milling

July 2015

Graduate School of Science and Technology
Keio University

KRUY, Sothea

Development of Burr Prediction System for End Milling

July 2015

A thesis submitted in partial fulfilment of the requirements for the degree
of Doctor of Philosophy in Engineering

Keio University

Graduate School of Science and Technology
School of Integrated Design Engineering

KRUY, Sothea

Table of Contents

List of Figures

List of Tables

ACKNOWLEDGMENT

ABSTRACT

In modern industry, the precision of machined workpiece plays important roles in the industrial applications. Edge imperfections are often introduced on workpiece as a result of plastic deformation during machining. These imperfections are known as burrs. A burr has been basically defined as a thin ridge or area of roughness produced when cutting or shaping metal. A burr leads to an undesirable workpiece edge that must be removed to enhance the level of precision of the part. This not only lowers the production quality, but also causes various problems such as attachment errors or mechanical problems. Thus, deburring processes are needed. However, even with the current sophisticated automation of production processes, deburring is often done by hand, and is a large obstacle to raising the efficiency of manufacturing processes. In addition, the cost of deburring a precision workpiece can be a significant addition to the cost of the finished parts. Thus, the control of burr formation is a research topic of great significance for industrial applications.

Predicting the positions and dimensions of burrs can be used as a countermeasure. This prediction can not only automate the deburring process but can also be applied to perform tool paths testing to reduce burr. Traditional studies on burr prediction have been based on experimental data. These methods are effective in processing methods with a limited number of parameters. However, they are not practical for complex machining with many parameters such as end milling, which would require large amount of experimental data for all its parameters.

In this paper, a system is proposed that uses a machining simulation to predict the positions and dimensions of burr in the end milling process as a preventive method. This system is based on burr formation models, the cutting conditions, and analytical cutting force mode. This system does not require a large quantity of experimental data like the systems used in traditional studies. Two kinds of burr models were used: rollover burr and Poisson burr. Orthogonal and oblique cuts were also applied in the system based on different positions. A Windows based program was developed to illustrate the machining process using a PC-based numerical control (NC) simulator that consisted of a geometric simulator and physical

simulator. The geometric simulator utilized feature identification and cutting condition identification. The physical simulator contained a cutting force model that was used to calculate the force in the feed direction that led to burr form. The proposed system was compared with experimental data for different workpiece materials for validation. It was verified that top and exit burrs could be predicted in up milling and down milling. The predicted and experimental results were found to agree under most of cutting conditions. In addition, a tool path planning scheme was included in the system to avoid tool exits. This method provides a feasible way of suppressing exit burr formation in an automatic manner, and thus reduces the need for deburring. Moreover, the results of a study of the burr size variation based on the tool flank wear in relationship to the cutting edge radius wear are also discussed. This study can be summarized as follows.

1. A burr prediction method for end milling was proposed based on an examination of the motion and shape of the cutting tool in two burr models for two-dimensional orthogonal cutting and three-dimensional oblique cutting.

2. A prediction method was developed for the thickness and height of a burr based on the burr formation mechanisms and calculation of the cutting force module using a cutting constant in end milling.

3. The usefulness of the burr prediction method and system was verified by performing cutting experiments in several kinds of material with a machining center (milling machine). It was verified that both the predicted and experimental results were found to agree under most of cutting conditions.

4. A method for tool path planning under a window framing scheme was proposed for burr minimization. The entrance burr for tool path in down milling seemed to be reduced burr size, but machine time was increased. The window framing method with roll-ending technique in down milling is a good method to avoid tool exit, thus minimizing burr.

5. A new model was proposed to understand the burr formation and tool wear behavior of a solid carbide tool during dry end milling. The tool flank wear was shown to have significant influence on the cutting force, and increase in cutting resulted in a substantial increase in the burr size.

CHAPTER 1

1. Motivation and Introduction

1.1 Overview of issues regarding burrs

In recent years, advances in computer technology have been introduced in manufacturing processes in order to improve manufacturing techniques in response to the demands placed by designers on workpiece performance and functionality. The computers behind these techniques, such as computer aided design (CAD), computer aided manufacturing (CAM), manufacturing planning and control systems (MP & CS), automated materials handling (AMH), flexible manufacturing systems (FMS) and robotics, have been used for easier communication between humans and machines. Recently, these techniques have focused on the development of computer integrated manufacturing (CIM); however, some specific areas such as cleaning, deburring, and surface finishing have not drawn much attention.

In the manufacturing environment, a burr has been defined as an excess of material beyond the edge of a workpiece as a result of the plastic deformation that occurs in cutting and shearing operations. Precision, high productivity manufacturing often requires a deburring or finishing operation. Burrs, together with chips, have been among the most troublesome obstacles to high productivity and the automation of machining processes. The current deburring methods involve manual operations or additional machining with abrasive or finishing tools. Although these are workable solutions, there have several limitations. They are tedious and time consuming. Deburring is usually the last process performed during part production. Thus, it can damage a part with high value or produces an undesirable part dimension. In addition, precautions have to be taken to ensure the safety of workers during the deburring process.

In the early 1970s, researchers gave much attention to the study of burr formation and deburring techniques. Many methods have been suggested to minimize burr formation or remove burrs. Gillespie and Blotter[1] were among the first researchers to study burr formation. They pointed out that deburring and edge finishing on precision workpieces may constitute as much as 30% of the part cost. They believed that burr technology was complex and it required academic excellence, as well as industrial experience. They classified the basic burr formation mechanisms into four basic types, the Poisson, rollover, tear, and cut-off burr formation mechanisms, using an approximation based on the classical plastic deformation mechanism. Other researchers have studied the costs associated with burrs and the basic mechanism for burr formation in machining. The German automotive and machine tool industries showed the costs of burr minimization, deburring, and part cleaning. In their study, the increased costs from burrs were caused by manpower and cycle time increases of about 15%, a 2% share in the rejection rate, and a 4% share in the machine breakdown times[7], as shown in Fig. 1.1. Chern and Dornfeld[2] and Ko and Dornfeld[3] gave more details for a rollover model in orthogonal and oblique cutting. Hashimura et al.[4] and Park and Dornfeld[5] conducted research analyses of the burr formation mechanism in orthogonal cutting including the influence of material properties based on a simulated analysis using the finite element method (FEM). Hashimura et al.[4] also provided schematic views of the burr formation mechanism in different types of workpiece materials, including both ductile and brittle materials. Ota et al.[17] proposed the basic burr prediction system; however, their study conducted only for basic shape and the cutting force model was based on cutting constant, which was determined through an experimental test. They did not proposed any specific method for tool path planning for burr minimization or consider the flank wear effect on burr formation.

1.2 Significance of research

Although several researchers have expressed a desire to understand the formation of burrs in more detail, it is not possible to accurately predict the burr size and location using the basic burr formation models. However, embedding a combination of databases on burr properties and burr formation models in a system would make it possible to predict the burrs sizes and locations on precision components. This system could inform the designer or production planner of the effect of certain design changes on the potential for burr formation,

which should make it possible to reduce the occurrence and severity of burrs on precision components.

Manpower

Ø 15% max. 20%

Extended cycle times

Ø 15% max. 20%

Reject Remachining

Ø 2% max. 5%

Machine breakdown

Ø 4% max. 10%
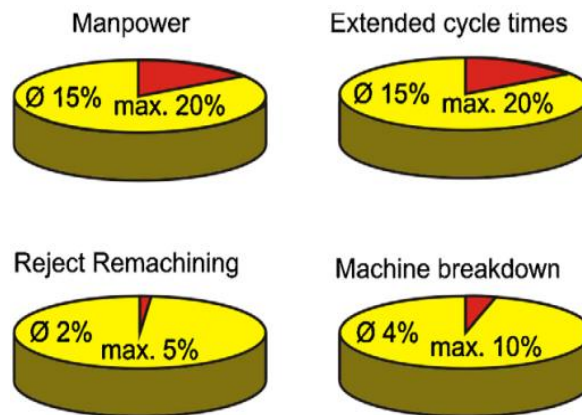
Fig. 1.1 Share of manufacturing effort caused by burrs[7].

1.3 Research objectives

To date, various methods[1,2,3,4,5] have been proposed for the development of burr prediction systems; however, there is no unique system that can be used as a preventive method and that can be applied in practical use. The objective of this thesis is to develop a system for predicting the positions and dimensions of the burrs formed, along with tool path planning for burr minimization and a model to predict the burrs cause by flank wear in the end milling process. This system is a represented in a CAD framework to illustrate the machining process upon a PC-based NC simulator that includes a database of workpiece material properties, tool geometry data, a cutting force model, cutting conditions, and a burr formation model. That information was applied to predict the burr positions and dimensions. Using this approach makes it possible to optimize the factors that affect burr formation, and thus burrs can be minimized.

1.4 Organization of dissertation

Chapter 1 gives an overview of the issues regarding burrs and the significance of this research, along with the objective of this study. A short review of the previous research on burr formation also given.

Chapter 2 provides background information on burr formation, including burr definitions, and describes the burrs from milling operations, mechanics of burr formation, and analytical models. In addition, burr classification is introduced, along with the types of burrs, parameters that influence burr formation, and burr measurement. The details of two kinds of burr models, the Poisson and rollover burr models, are presented.

Chapters 3 and 4 describe the burr prediction method and development of a burr prediction system. The system architecture of the burr development system in end milling is also illustrated. The development of a geometric simulator is proposed, including a Z-map model, an NC program analysis model, and the identification of up milling and down milling. A physical simulator method is proposed that utilizes three cutting states. A mechanistic forces model, which is an important factor influencing burrs, is illustrated in detail. The identification of the burrs formed in an NC simulation is also explained, and the burr models are applied in end milling. A study was conducted on tool path planning for burr minimization. The influence of the flank wear on burr formation was identified using a cutting edge radius wear analytical model.

In order to verify the proposed burr prediction system for end milling, machining experiments had to be conducted under various cutting conditions. Chapter 5 describes ten experiments that were conducted with a new end milling tool, along with another ten experiments using an end milling tool with flank wear. The experiments were conducted using different kinds of workpiece materials, including steel with 0.45% carbon, aluminum alloy AlMg0.5Si, gray cast iron 250, and stainless steel 6 in 20×20×30-mm sections. The discussion describes the influence of these conditions on the burr sizes. Experimental tests were also conducted to evaluate the burr prediction relation to the flank wear in the end milling. A summary of the thesis is given in chapter 6.

CHAPTER 2

2. Literature Review

2.1 Burr descriptions and classification

2.1.1 Burr definitions

In the Oxford English Dictionary, a burr is described as a rough ridge or edge left on metal or another substance after cutting, punching, etc.; e.g., the roughness produced on a copper plate by the graver, the rough neck left on a bullet in casting, or the ridge left on paper, etc. by a puncture. In most cases, a burr is defined as a thin ridge or area of roughness produced in cutting or shaping metal. According to ISO 13715[6], the edge of a workpiece is defined as having a burr when it has an overhang greater than zero, as shown in Fig. 2.1 (c). Chern and Dornfeld[2] defines a burr as the plastically deformed material left and attached to a workpiece after machining. Based on Ko's finding[3], a burr was defined as an "undesirable projection of material formed as the result of plastic flow from a cutting or shearing operation." Thus, a burr has been defined as an excess of material beyond the edge of a workpiece as a result of the plastic deformation that occurs in cutting and shearing operations.

A burr's geometry was defined by Aurich et al.[7], as shown in Fig. 2.1 (a) and (b). He described basic burr parameters using a random cross-section as follows:

- The burr root b_f: the thickness of the burr root
- The burr height h_o: the distance between the ideal edge of the workpiece and the highest point in the cross section
- The burr root radius r_f: the radius of a circle positioned at the burr root
- The burr thickness b_g: the thickness parallel to the burr root area at a distance of r_f

(a) Burr geometry[7]

$$g = \frac{4 \cdot b_r + 2 \cdot r_f + b_g + h_0}{8}$$

b_r : Burr root thickness
f_r : Burr root radius
b_g : Burr thickness
h_0 : Burr height
v : Effective exit surface angle

Burr value:

(b) Burr profile in cross direction[7]

(c) Definitions of burrs according to ISO 13715[6]
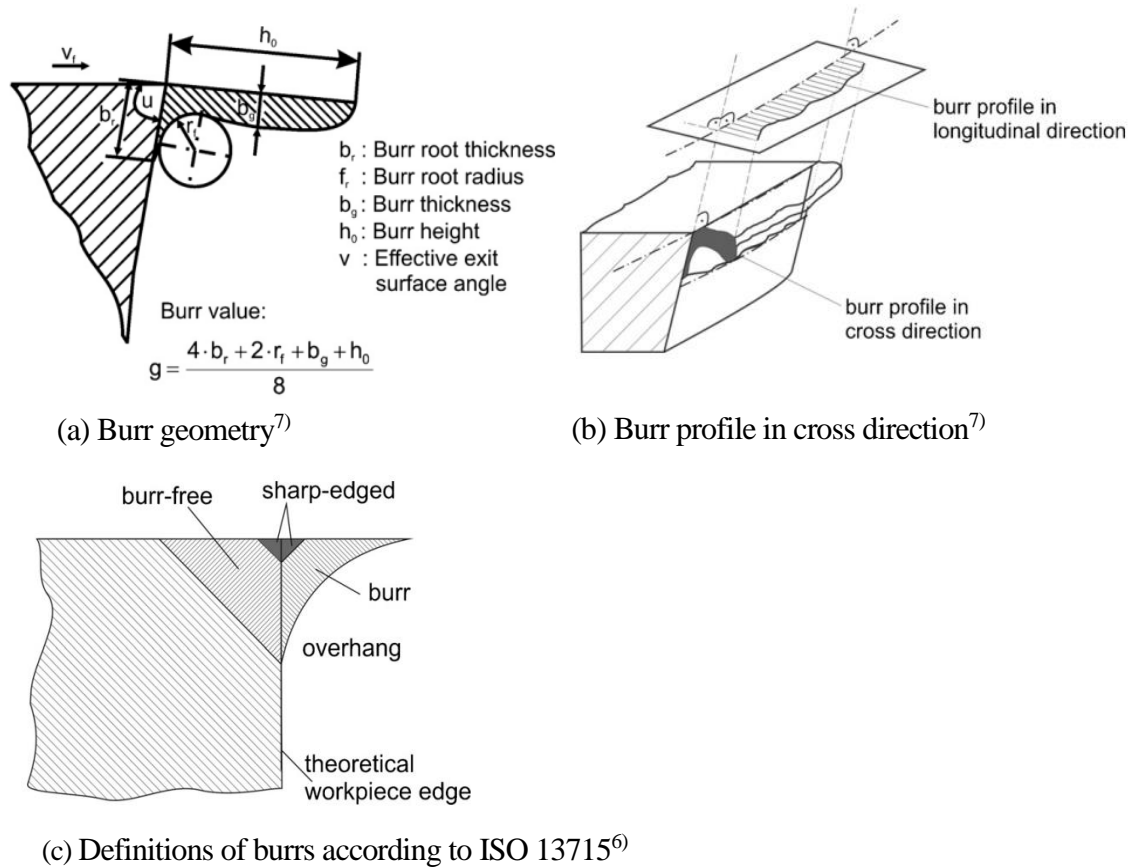
Fig. 2.1 Definitions and geometry of a burr[6,7].

2.1.2 Burr from milling operations

The type of burr found in face milling operations was observed by Chern and Dornfeld[2] to be dependent on the in-plane exit angle. He reported five types of burrs, as illustrated in Fig. 2.2: (a) the knife-type burr, (b) curl-type burr, (c) wave-type burr, (d) edge breakout, and (e) secondary burr.

An end mill can produce eight different burrs in a single slotting operation. These burrs all occur on different edges. For example, in a bottom cutting profiling operation, six edges are produced, and a different group of burrs occurs on each edge, as shown in Fig. 2.3. Gillespie and Blotter[1] classified slot milling according to the burr locations, burr shapes and burr formation mechanisms. An exit burr forms when the minor edge of the tool moves away from the workpiece edge. A side burr is defined as occurring on the major edge of the tool cut side surface of the workpiece, and a top burr is defined as a burr attached to the top surface of the

workpiece edge. In Figure. 2.3, the burrs along edges 3, 7, and 9 are the results of chips rolling over, rather than having been sheared from the workpiece[1]. The burrs on edges 1, 2, and 10 are the results of lateral deformation due to Poisson's ratio. The burrs along edges 4 and 6 result from material flowing in a direction 180° away from the direction of tool travel. The burrs along edges 8 and 5 vary noticeably along each edge. These are combinations of entrance and rollover burrs.

(a) knife-type burr   (b) curl-type burr   (e) secondary burr

(c) wave-type burr   (d) edge breakout
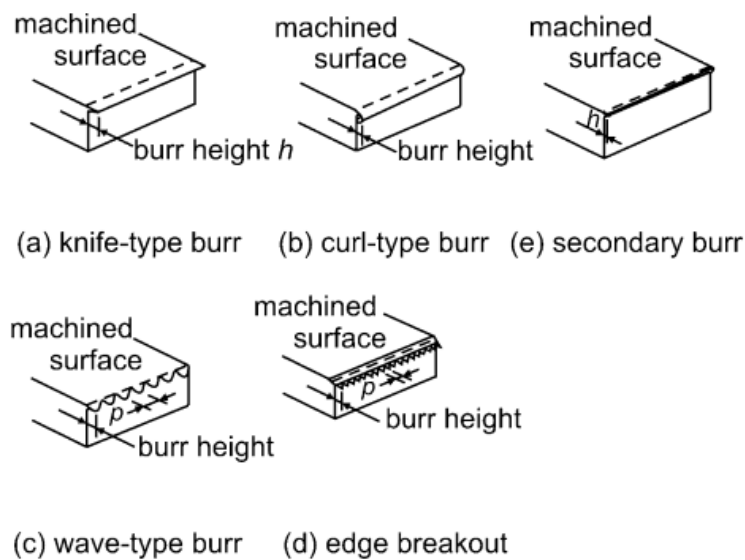
Fig. 2.2 Five types of burrs observed in face milling[2].

Gillespie and Blotter[1] also conducted a basic study on the exit side burr along edge 3 shown in Fig. 2.3. They stated that this burr formed based on multiple cuts of the cutter teeth rubbing numerous tightly stacked flaps of material, causing it to roll over repeatedly until the burr fully formed. They showed that the height of this burr is directly proportional to the radial depth of cut as and approximately 0.6 times the cutter diameter. At this radial depth of cut, the material ahead of the cutter tears. Thus, the rollover burr height can be up to 0.6 times the cutter diameter.
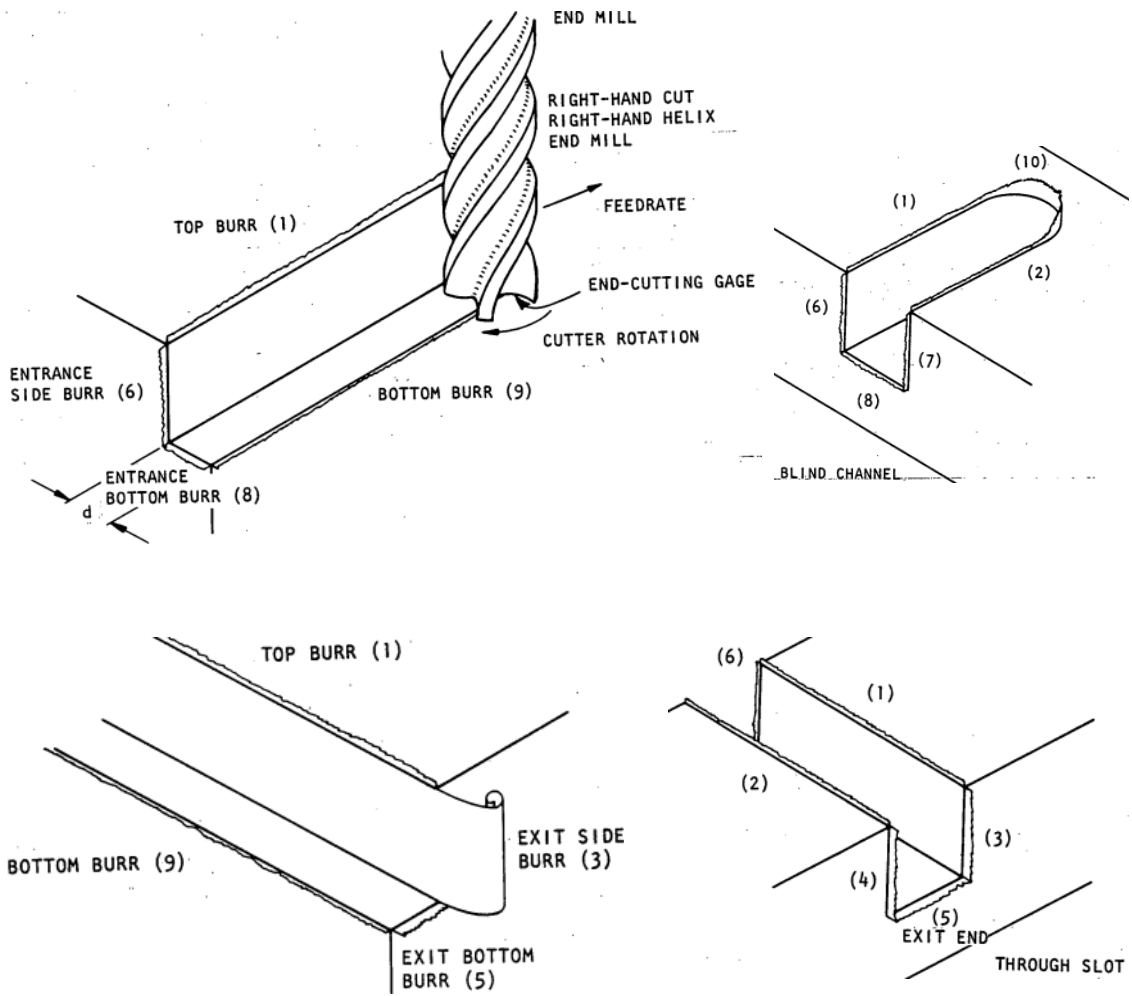
Fig. 2.3 Identification of burr locations in end milling[1].
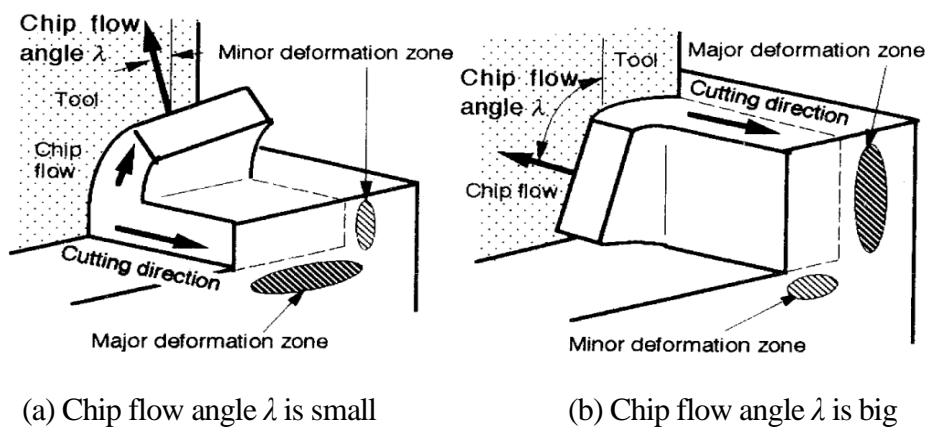
(a) Chip flow angle λ is small   (b) Chip flow angle λ is big

Fig. 2.4 Relationship between chip flow angle and region chip deformation[8].

Hashimura et al.[8] studied the effects of the in-plane exit angle and rake angles on the burr height and thickness. In their study, they used the geometric concept of the chip flow direction to explain the effect of milling tool geometries such as the axial and radial rake angles on the burr formation mechanism on transition and machined surfaces, as shown in Fig. 2.4. The burrs are large in the zone of major deformation in contrast to those in the minor deformation zone. In addition, their study showed the effect of the exit order of the tool edges on burr formation. They classified the ideal geometric relations of three points on the tool edge (A, B, and C), which were determined by the geometry and cutting conditions, as shown in Fig. 2.5. The distance between the spindle and workpiece edge L and feed rate f can be defined in Eqs. (2.1) and (2.2), respectively.

$$L = R \cos \psi_{exit} \tag{2.1}$$
$$f = W / \sin \psi_{exit} \tag{2.2}$$

where R is the radius of the cutting tool, W is the undeformed chip thickness at the exit point, and ψ_{exit} is the in-plane exit angle.

(a) Geometric relationship

(b) Exit order A → C
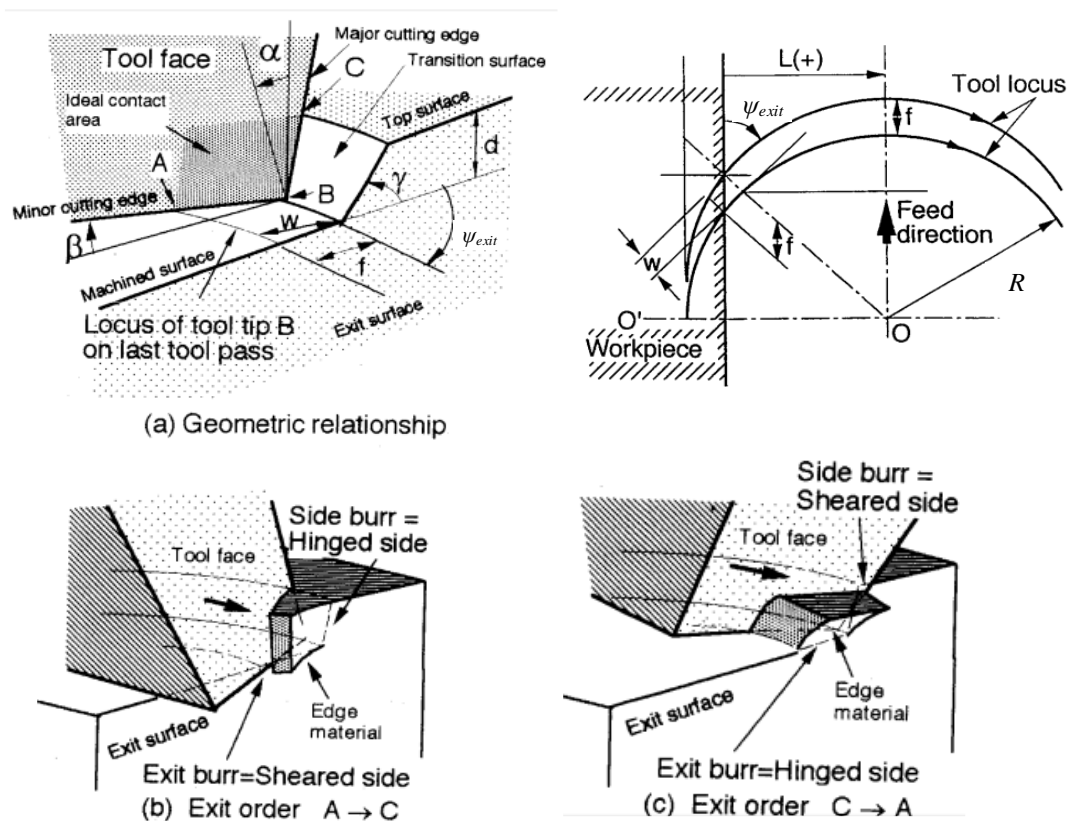
(c) Exit order C → A

Fig. 2.5 Exit order and burr formation process[8].

9

2.2 Mechanics of burr formation

Gillespie and Blotter[1] classified the basic mechanisms of burr formation into four basic types, the Poisson, rollover, tear, and cut-off burr, formation mechanisms, using an approximation based on the classical plastic deformation mechanism. When the cutting tool presses the workpiece, Poisson burrs protrude horizontally. This type of burr depends on the Poisson ratio of the material. When the cutting tool reaches the cutting end of the material, the removed material is rolled over along the edge due to the higher plastic deformation around the cutting edge. These burrs are rollover burrs. They are produced because they fail to form chips and detach from the parent material. Other burrs are generated from the edge of the cutting tool when the material is torn. This type of burr usually occurs in punch press processes. The last type of burr is called a cut-off burr. These burrs are formed when the material breaks right before the completion of the turn in a lathe cutting process. This type of burr is highly related to the cutting force, not the result of the plastic deformation of the material. A detailed review is conducted only for the Poisson burr and rollover burr because these two kinds of burrs were considered in this study.

2.2.1 Poisson burr model

A Poisson burr is formed when the cutting tool pushes into a workpiece, which causes the material near the cutting tool edge to bulge because plastic deformation of the workpiece material occurs around the tool. In this analytical model, the cutting tool edge is considered to be a cylinder with a tool radius of R. As the tool continues to advance through the workpiece, burrs are formed on all the surfaces in contact with the tool, as shown in Fig. 2.6. These burrs are called "Poisson burrs" and are the result of the lateral deformation that occurs whenever a solid is compressed. They are named after Poisson's ratio. A Poisson burr is relatively small in size and can be defined in terms of its thickness (PB_{th}) and height (PB_l), as shown in Eq. (2.3) and Eq. (2.4), respectively.

$$PB_{th} = R_e \left(\exp(-3\phi_a)\sqrt{\cos\phi_a} - 1 \right) \tag{2.3}$$

$$PB_l = \frac{d_a(1+\upsilon)\sigma_y\left(\exp(-3\phi_a)\right)}{\sqrt{3}E}\left[\frac{-\sin\phi}{2\left(\sqrt{3}\cos\phi + \sin\phi\right)} \right] \tag{2.4}$$

$$\phi_a = -\sin^{-1}\left(\frac{\sqrt{3}P_0}{2\sigma_y}\right) + \frac{\pi}{6} \tag{2.5}$$

$$\phi = (\sin^{-1}(2 \times (\sigma_y/\sigma_u) \times \sin(45 + \alpha/2) \times \cos(45 - \alpha/2) - \sin\alpha) + \alpha)/2 \tag{2.6}$$

$$P_o = \frac{F_c \times \cos\alpha - F_f \times \sin\alpha}{d_a \times a_o} \tag{2.7}$$

where R_e is the effective cutting edge radius; ϕ_a is the plasticity ellipse angle, which can be found using Eq. (2.5); ϕ is the shear angle in orthogonal cutting, which can be found using Eq. (2.6); E is the Young's modulus of the workpiece; d_a is the axial depth of the cut; v is Poisson's ratio, P_o is the pressure applied at the tool radius, which can be found using Eq. (2.7); σ_u and σ_y are the ultimate tensile strength and yield strength of the workpiece respectively; F_c is the main cutting force; F_f is the cutting force in the cutting direction; and a_o is the arc length of the cutting edge in contact with the workpiece.

Figure 2.6 shows the unique phenomenon of plastic flow starts at point Q_o where a stagnation point appears at angle θ between -57° and -65°, according to Woon[10] and Yen[11]. At point Q_1, the elastic deformation springs back after moving the tool, and behind point Q_2, the plastic deformation leads to the final deformation of the surface layer, and a burr is formed.
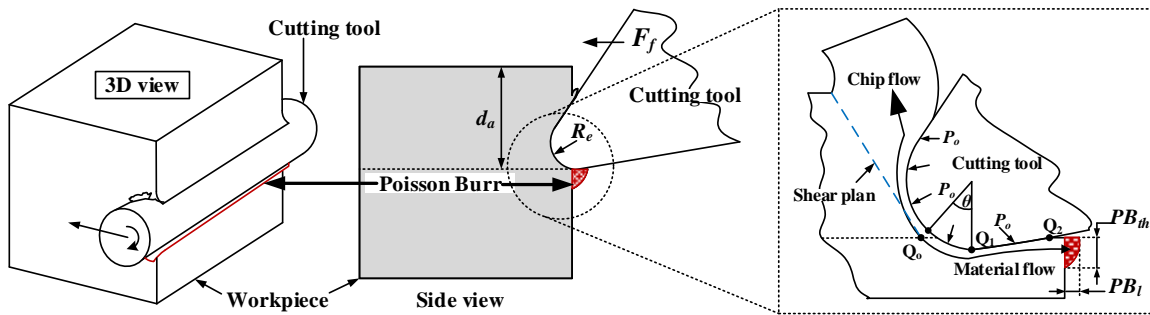
Fig. 2.6 Poisson burr formed when cutting tool pushed into workpiece[9].

2.2.2 Rollover burr model

This burr occurs just before the cutting tool leaves the workpiece. An elastic deformation zone appears at the workpiece edge as elastic bending and plastic deformation also appear near the primary shear zone as plastic bending. A pivoting point appears on the workpiece edge where a large deformation occurs. The burr is developed with the formation of a negative shear zone that expands from the pivoting point to the primary shear zone. Crack formation occurs at the tool tip, which leads to two types of burrs at the end of the deformation: a negative burr, and positive burr. The whole process of rollover burr formation can be divided into two parts.

The first part is the burr development before the crack propagation. In this part, the rollover burr seems to be formed by the deformation, without the formation of a crack. As we can see in Figure. 2.7, the elastic/plastic deformation zone around the tool tip starts to form in stage 1, and the plastic deformation continuous to grow until the negative shear zone becomes fully developed. The burr formation mechanisms considered by Hashimura[4] are as follows:

1. Continuous cutting: During the cutting process, there are three- deformation zones formed around the cutting tool tip: the primary shear zone, plastic zone, and elastic zone.

2. Pre-initiation: In this stage, the elastic zone intersects the workpiece edge. The plastic zone also expands toward the workpiece edge.

3. Burr initiation: The plastic deformation starts to form at the workpiece edge and grows toward the other plastic deformation zone around the tool tip.

4. Pivoting: The deformation starts to become large, and the workpiece edge starts to have more bending, with the center point called the pivoting point on the surface of the workpiece edge.

5. Negative shear zone development: A negative shear zone is formed as a result of the shear zone growth from around the cutting tool tip to the pivoting point. As the tool moves toward the workpiece edge, the burr size increases.
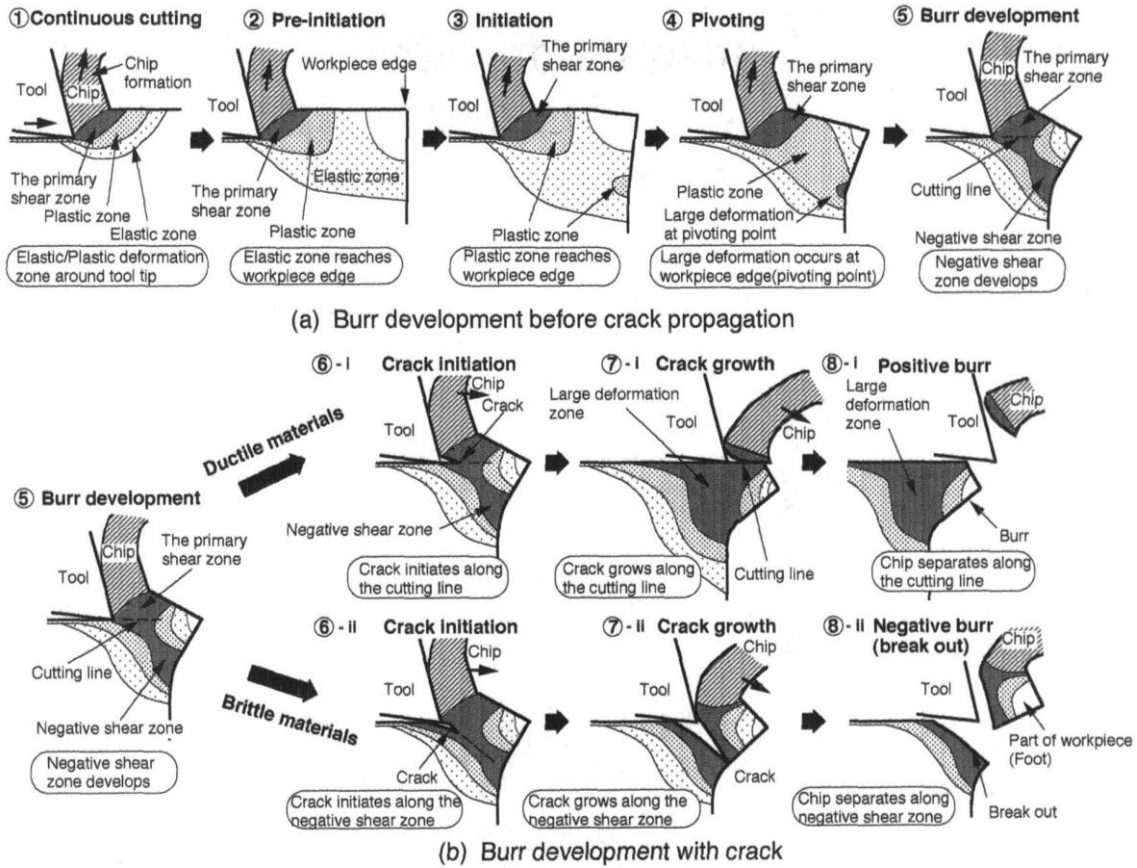
Fig. 2.7 Rollover burr formation process[4].

A negative burr forms mostly for brittle materials. For this type of burr, the crack starts at the tool tip in the primary shear zone in the direction of the cutting line to the workpiece edge, as shown in Fig. 2.7 (stage 8). An indication of the ductility is the percentage of reduction in the area at fracture, E, in a tensile test. The equivalent strain at fracture ε_f can be related to E as follows:

$$\varepsilon_f = \ln\left(\frac{A_0}{A_f}\right) = \ln\left(\frac{1}{1-E}\right) \tag{2.8}$$

As suggested by Gillespie and Blotter[1], the fracture will occur along the negative deformation plane if

$$\varepsilon_a \geq \varepsilon_f \tag{2.9}$$

where ε_a is the shear strain around the cutting tool tip and can be approximated by the von Mises (distortion-energy) theory as $\varepsilon_a = \frac{\gamma}{\sqrt{3}}$, $\gamma = \cot\beta_0 - \cot(\phi + \beta_0)$, and β_o is the initial negative deformation angle and is defined by Eq. (2.15). When the fracture occurs along the negative deformation plane, a negative burr or breakout is formed, leaving a chamfer on the workpiece. It is possible to define the length of the breakout surface η as in Eq. (2.10), from Chern and Dornfeld[2].

$$\eta = \frac{d_a(\cot\phi + 0.5\cot\beta_0)\sin\theta_{ex}}{1 - \tan\beta_0\cot\theta_{ex}} \qquad (2.10)$$

A positive burr forms in ductile materials. Chern[2] was the first researcher to perform a detailed study on the positive burr formation mechanism based on scanning electron microscope (SEM) photographs of the burr formation process during orthogonal cutting, as shown in Fig. 2.8. He assumed that the chip had no effect on the burr formation and would finally separate from the workpiece along the shear plane. In his observations, the process of burr formation was started from initiation state (ACEB) to burr development state ($A_1C_1E_1B$ or $A_2C_2E_2B$), and finally finished at burr final formed ($A_3C_3E_3B$), as shown in Fig. 2.8. In addition, the crack started at the tool tip in the primary shear zone, as shown in Fig. 2.9, and changed direction toward the pivoting point. The size of this burr can be defined by its thickness (RB_{th}) and height (RB_h), as shown in Eq. (2.11) and Eq. (2.12), respectively.

$$RB_{th} = w \times \tan\beta_o \qquad (2.11)$$

$$RB_h = (t_o + w \times \tan\beta_o) \times \sin(\theta_1 + \theta_2) \times \sin\theta_{ex} \qquad (2.12)$$

where w is the initial tool distance from the end of the workpiece and is delineated by Eq. (2.13) and Eq. (2.14) for orthogonal cutting and oblique cutting respectively, as shown by Ko and Dornfeld[3]. He performed a detailed study on burrs in the oblique cutting process, as shown in Fig. 2.10. θ_{ex} is the exit angle, t_o is the undeformed chip thickness, and θ_1 and θ_2 are the rotation angles near the pivoting point on the burr side and can be defined in Eq. (2.16) and Eq. (2.17).
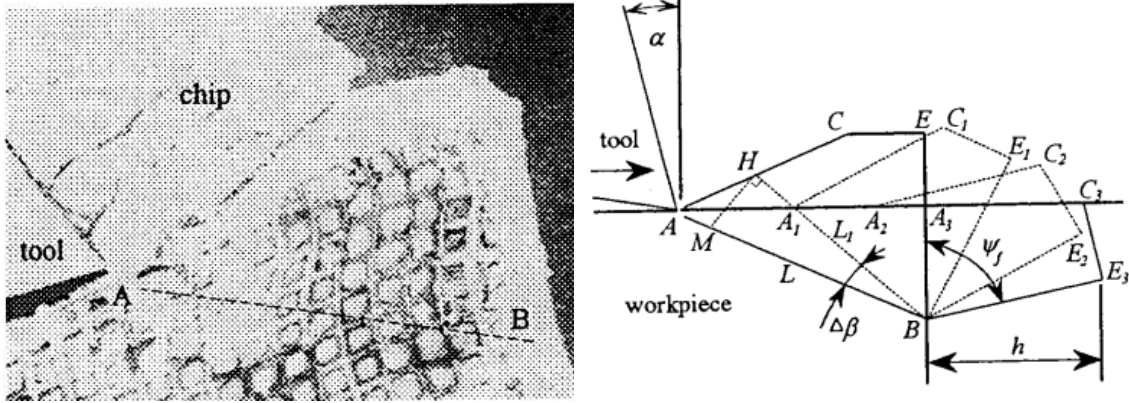
Fig. 2.8 SEM microphotograph at initiation state of burr formation[2].
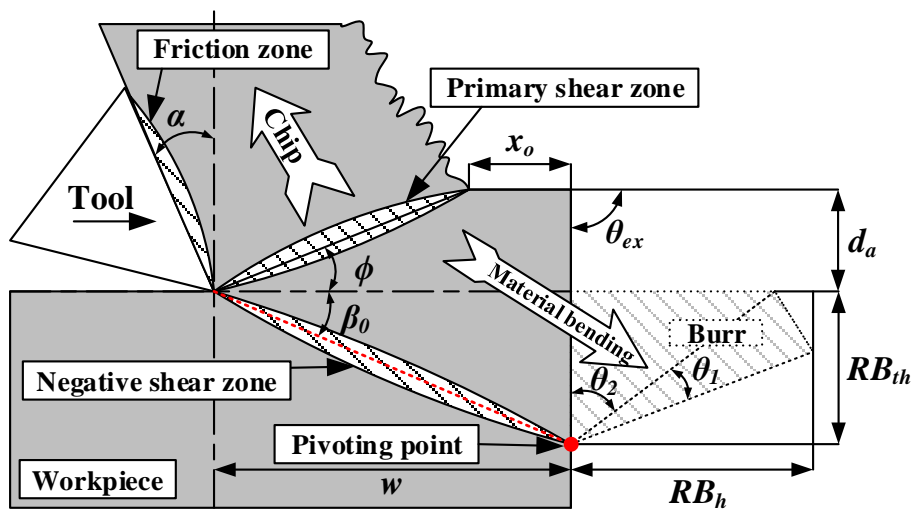
Fig. 2.9 Rollover burr that occurs when cutting tool exits workpiece[9].

$$w_{orthogonal} = \cfrac{\cfrac{F_f}{\cos(\lambda - \alpha)\cos(\varphi - \alpha)}\left[\cos\alpha\cos(\varphi + \lambda - \alpha) + \sin\varphi\sin\lambda\right]}{\left(\cfrac{k_0}{2}\cos^2\beta_0 + \cfrac{\sigma_y}{4}\tan\beta_0\right)d_r} \tag{2.13}$$

$$w_{oblique} = \cfrac{\cfrac{F_f}{\cos(\lambda - \alpha_c)\cos(\varphi_c - \alpha_c)}\left[\cos\alpha_c\cos(\varphi_c + \lambda - \alpha_c)\cos\kappa + \sin\varphi_c\sin\lambda\cos\chi\right]}{\left(\cfrac{k_0}{2}\cos^2\beta_0 + \cfrac{\sigma_y}{4}\tan\beta_0\right)d_r} \tag{2.14}$$

$$\frac{d}{d\beta_0}\left\{\frac{\sin\beta_0(\cot\varphi + 0.5\cot\beta_0)}{(\cos\beta_0 - \sin\beta_0\cot\theta_{ex})}\left[2 + 3\cot\beta_0 - 3\cot(\varphi + \beta_0)\right]\right\} = 0 \tag{2.15}$$

$$\theta_1 = \tan^{-1}(x_o / (t_o + w \times \tan\beta_o)) \tag{2.16}$$

$$\theta_2 = \cos^{-1}((w \times \tan\beta_o \times \sin\theta_1) / x_o) \tag{2.17}$$

$$\phi_c = \tan^{-1}(\tan\phi \times \cos i) \tag{2.18}$$

where λ is the friction angle obtained from $\lambda = \tan^{-1}(\mu)$; μ is the coefficient of friction; α is the rake angle in orthogonal cutting; α_c is the rake angle in oblique cutting, which is equal to $\tan^{-1}(\tan\alpha / \cos i)$; d_r is the radial depth of cut; $k_o = \frac{\sigma_y}{\sqrt{3}}$ is the shear yield stress of the workpiece; ϕ_c is the shear angle in oblique cutting, which can be defined as in Eq.(2.18); $\cos\chi = \cos i / \cos\zeta$; $\cos\kappa = (\cos i \times \sin\phi) / \sin\phi_c$; $\zeta = \tan^{-1}(\sin\alpha \times \tan i)$, $x_o = (0.5 \times \cot\beta_o) \times t_o$; and inclination angle $i = \pi/2 - \alpha$.
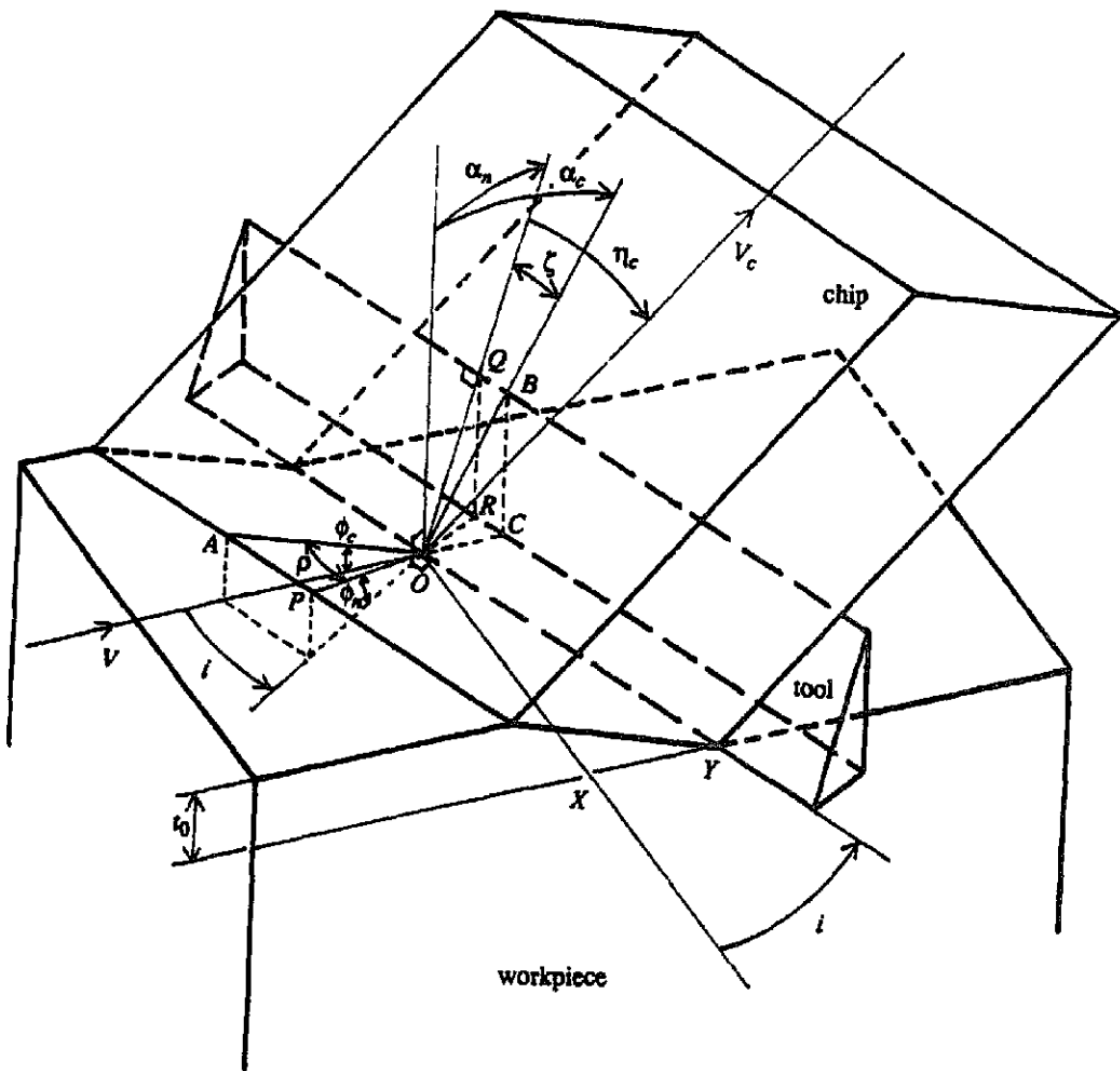
Fig. 2.10 Schematic illustration of oblique cutting[3].

2.3 Parameters that influence burr formation

As Gillespie and Blotter[1] mentioned in their work, burrs cannot be prevented simply by changing some parameters such as the feed, speed, or tool geometry. To minimize and prevent burrs it is necessary to examine the entire cutting process. The major influences include the workpiece material, tool geometry, tool wear, tool path, and machining parameters. It is not possible to change the workpiece material in some cases, and the tool path is limited, because complex geometries would require burr optimized tool paths that would prolong the cycle time, which would be a negative effect. The burr formation parameters can be reliably separated into direct and indirect factors because of the complex connections and relations between the numerous influencing variables, as shown in Fig. 2.11.
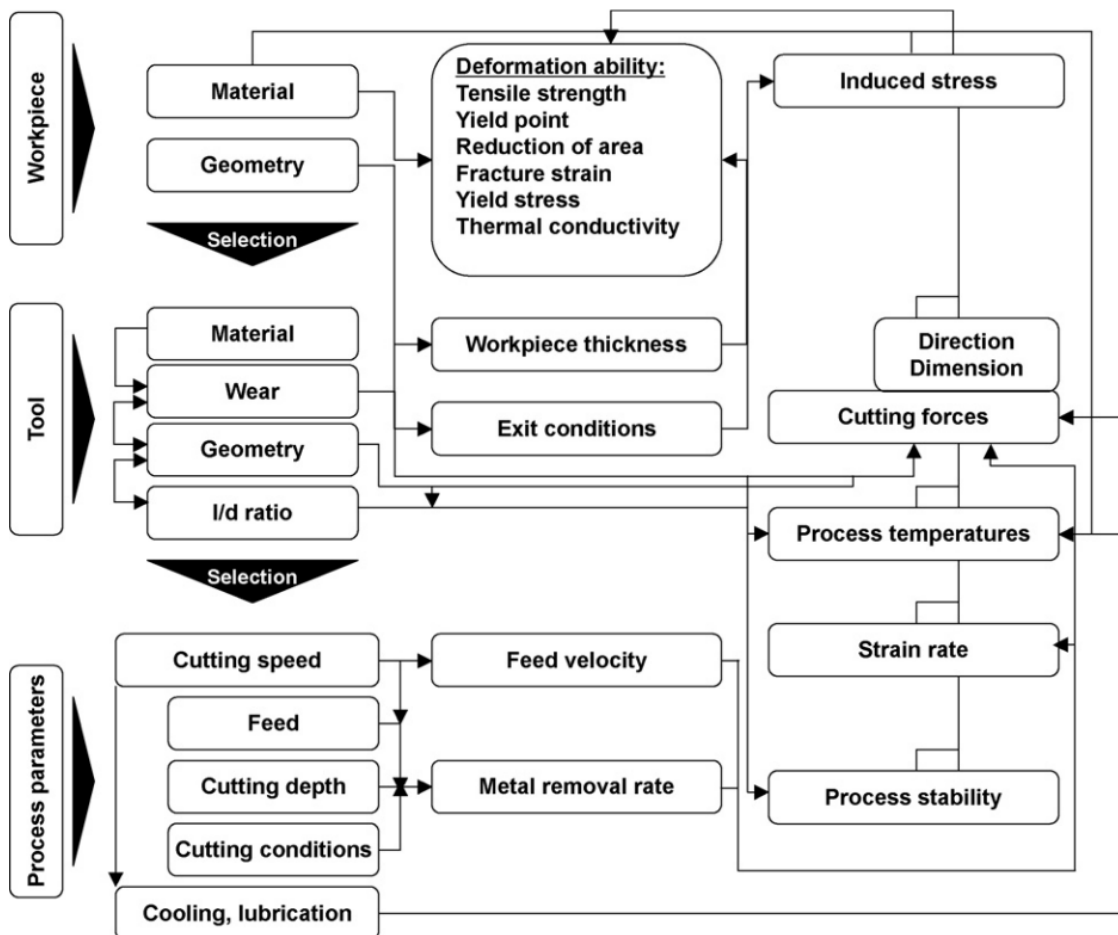
Fig. 2.11 Interdependencies of burr formation parameters[7].

2.4 Burr measurement

Burr measurement methods have been developed by many researchers. Each method has different pros and cons depending on the application conditions, requested measurement accuracy, and burr values to be measured, like the burr height or burr thickness. The types of burr measurement methods can be classified as follows:

- One-, two- or three-dimensional
- Destructive or non-destructive
- With or without contact[7]
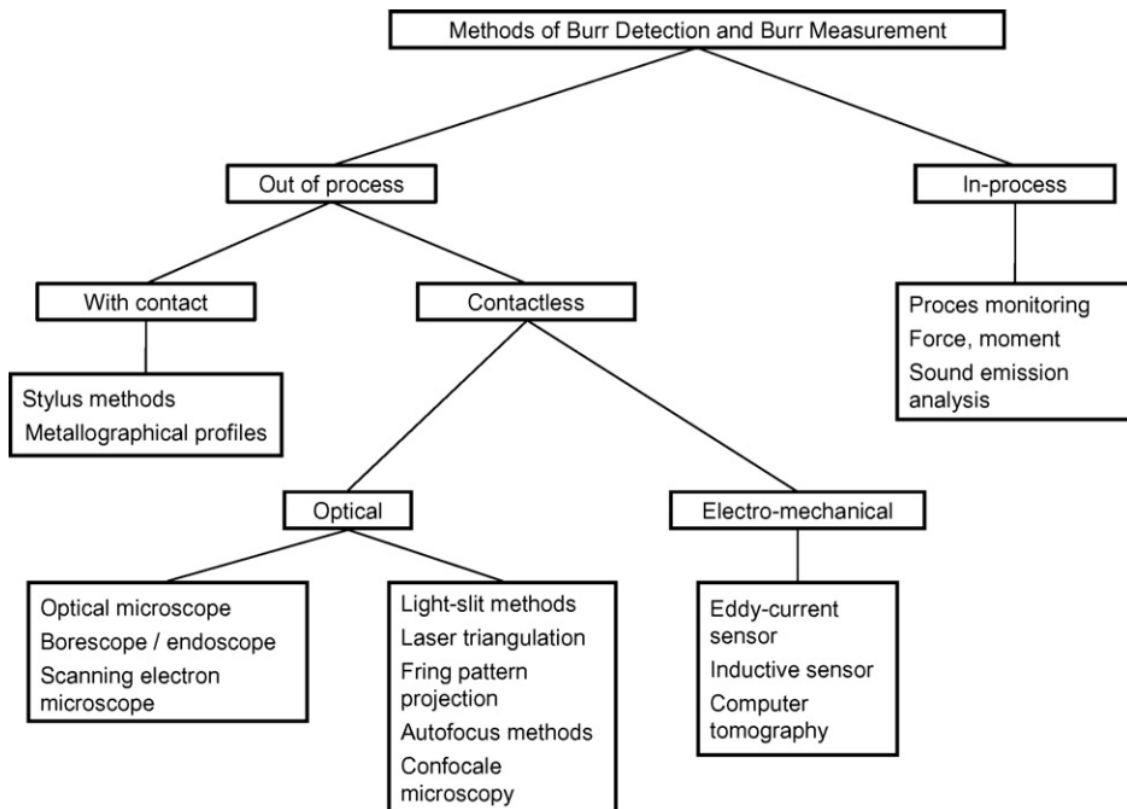
Fig. 2.12 Methods of burr detection and measurement[7].

2.5 Chapter summary

This chapter described the general burr formation mechanisms, burr classification, parameters that influence burr formation, and burr measurement methods. The burr definitions based on the work of many researchers, and the burrs from milling operations were described in detail, including about the names and locations of the burrs formed. The mechanics of burr formation and analytical models were discussed from the initial burr state to the final burr formed. Two kinds of workpiece materials were included in this discussion: ductile and brittle materials. Two kinds of burr mechanism models were described in detail: the Poisson burr model and rollover burr model. The many interdependencies of the burr formation parameters were briefly shown to allow a better understanding of the influence of the cutting conditions on burr formation. The burr measurement methods were also shown as basic information on the selection of a method for burr measurement.

CHAPTER 3

3. Burr Prediction Method

3.1 Classification of burrs in end milling

In this study, a burr simulation system was developed and used to predict the sizes and locations of burrs. In order to obtain an accurate prediction, burrs were classified based on the relationship between the cutting tool and workpiece in end milling. Two cutting modes were also considered: down milling and up milling, as shown in Fig. 3.1.
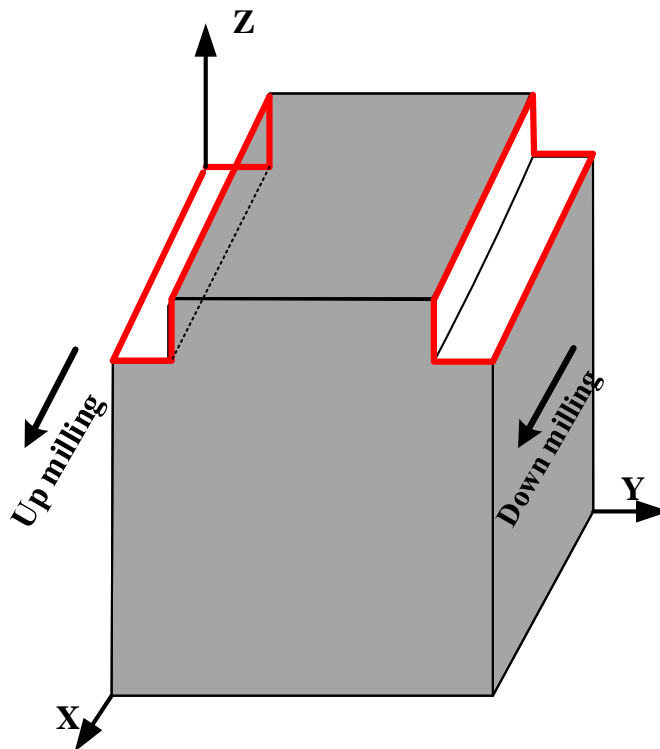
Fig. 3.1 Locations of burrs shown in red for end milling process.

3.1.1 Entrance burr

This burr is formed on the entrance edge of the workpiece where the cutting tool tips push into it, as shown in Fig. 3.2.

(a) Up milling   (b) Down milling
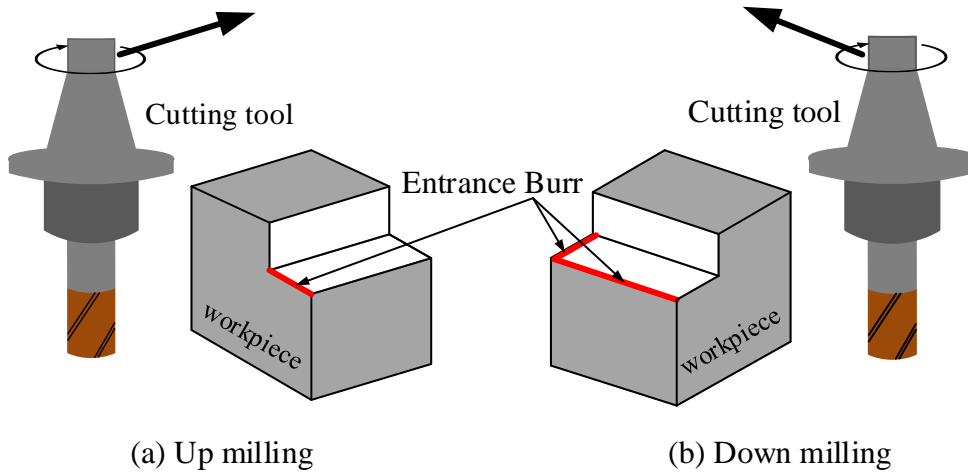
Fig. 3.2 Entrance burr location.

3.1.2 Entrance side burr

This burr is formed on the entrance side edge of the workpiece where the cutting tool tips push into it, as shown in Fig. 3.3.

(a) Up milling   (b) Down milling
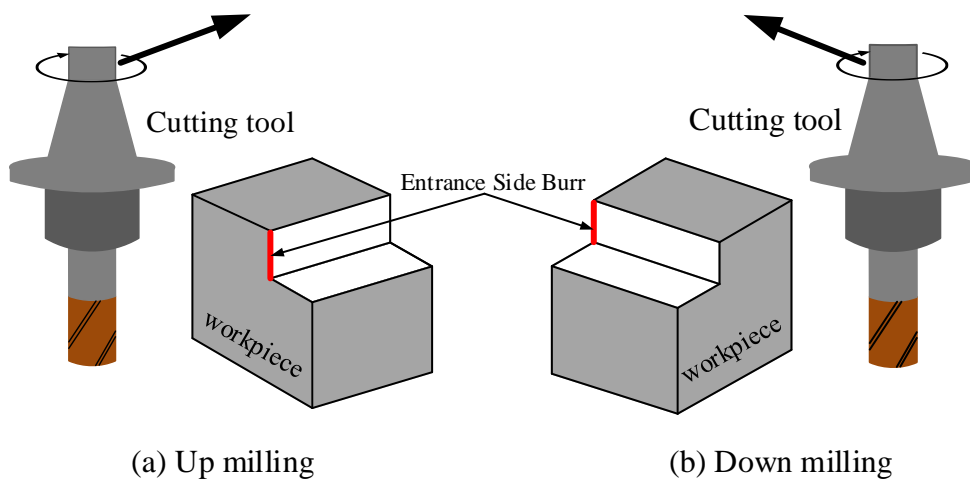
Fig. 3.3 Entrance side burr location.

3.1.3 Top burr

This burr is formed on the top edge of the workpiece where the tool tips push up in the Z direction, as shown in Fig. 3.4.

Cutting tool   Cutting tool

Top Burr

workpiece   workpiece

(a) Up milling   (b) Down milling
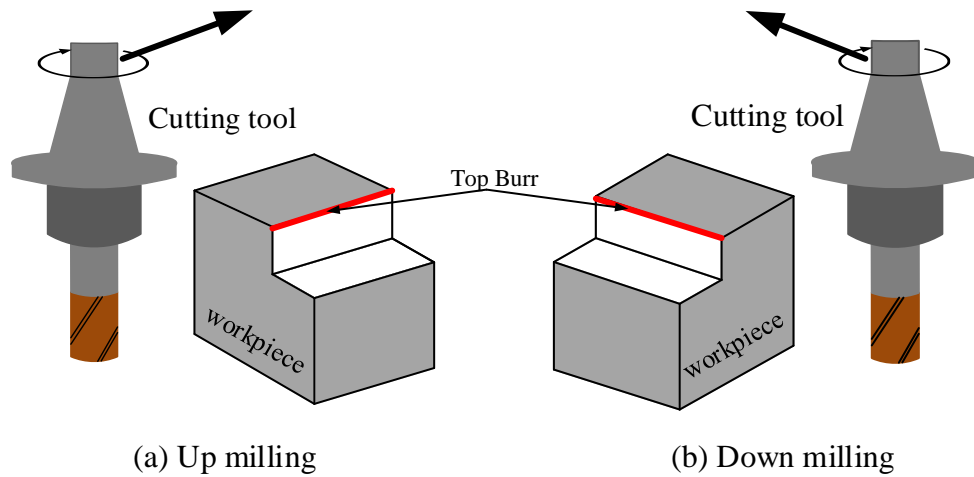
Fig. 3.4 Top burr location.

3.1.4 Exit burr

This burr is formed when the cutting tool leaves the workpiece, as shown in Fig. 3.5.

Cutting tool   Cutting tool

Exit Burr

workpiece   workpiece

(a) Up milling   (b) Down milling
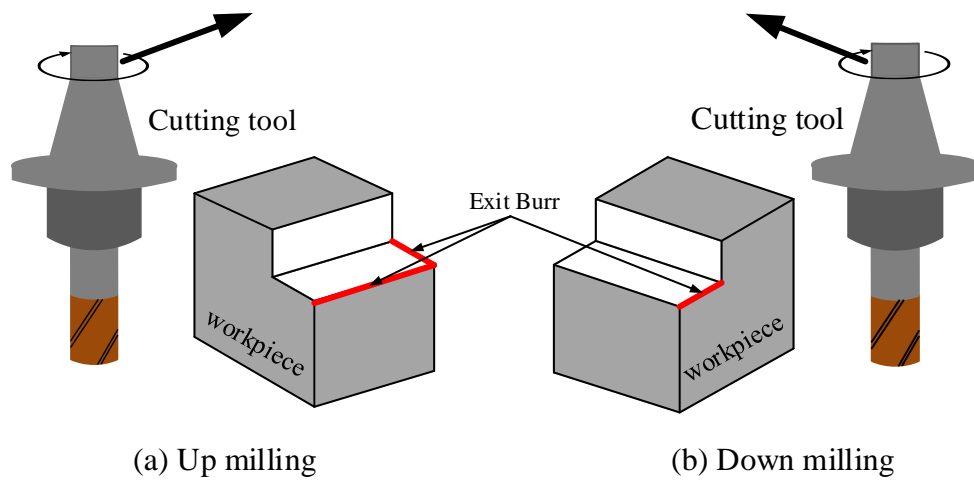
Fig. 3.5 Exit burr location.

3.1.5 Exit side burr

This type of burr is formed when the cutting tool leave the workpiece side edge, as shown in Fig. 3.6.

(a) Up milling (b) Down milling
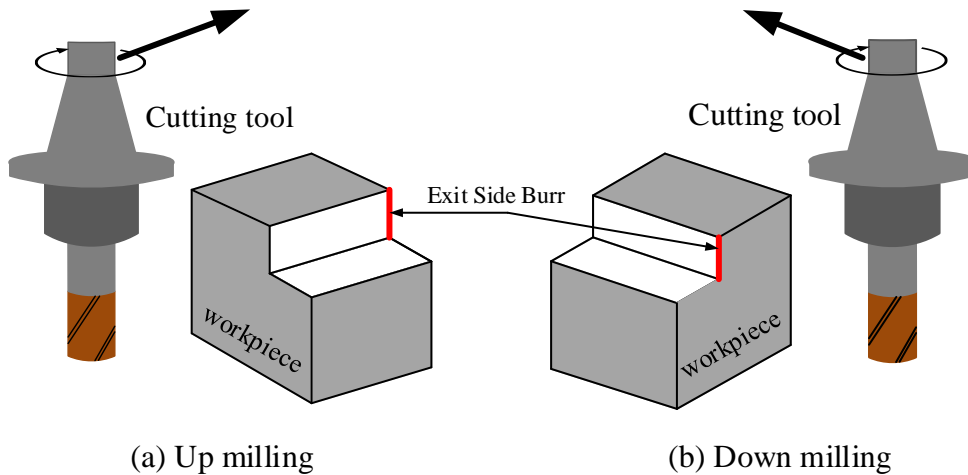
Fig. 3.6 Exit side burr location.

3.2 Application of burr models in end milling

3.2.1 Entrance burr model in up milling

The burrs on the workpiece edge shown in Fig. 3.2 (a) occur when the cutting tool moves in the direction to approach workpiece edge. Thus, the Poisson burr model is used to define the burr size. However, tool geometry is also considered in this case for better burr prediction. In Figure. 3.7, the bottom view of the end milling shows a hook shape near the end of the tool tip, which is a critical form to consider. When the blade pushes into workpiece edge, two burr models will apply: rollover burr and Poisson burr models. When the interference point $P(X_p, Y_p)$ advances to the center point $O(X_o, Y_o)$, the rollover burr model is applied; otherwise, the Poisson burr model is used. This is because, when the point P advances toward the point O, the tool blade motion is seen to push the workpiece material out from the workpiece edge rather than push in. In contrast, when the point O advances toward the point P, the tool blade motion pushes against the side workpiece edge, which is why the Poisson burr model is applied, as shown in Fig. 3.8.
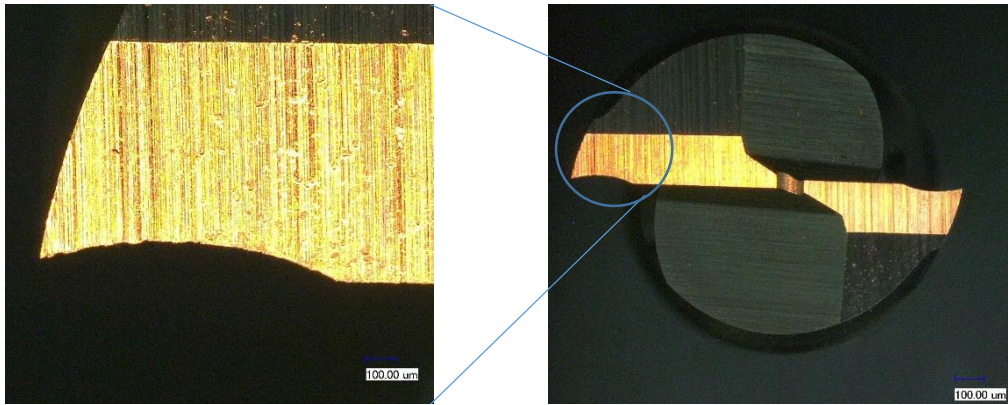
Fig. 3.7 Bottom view of end milling tool.
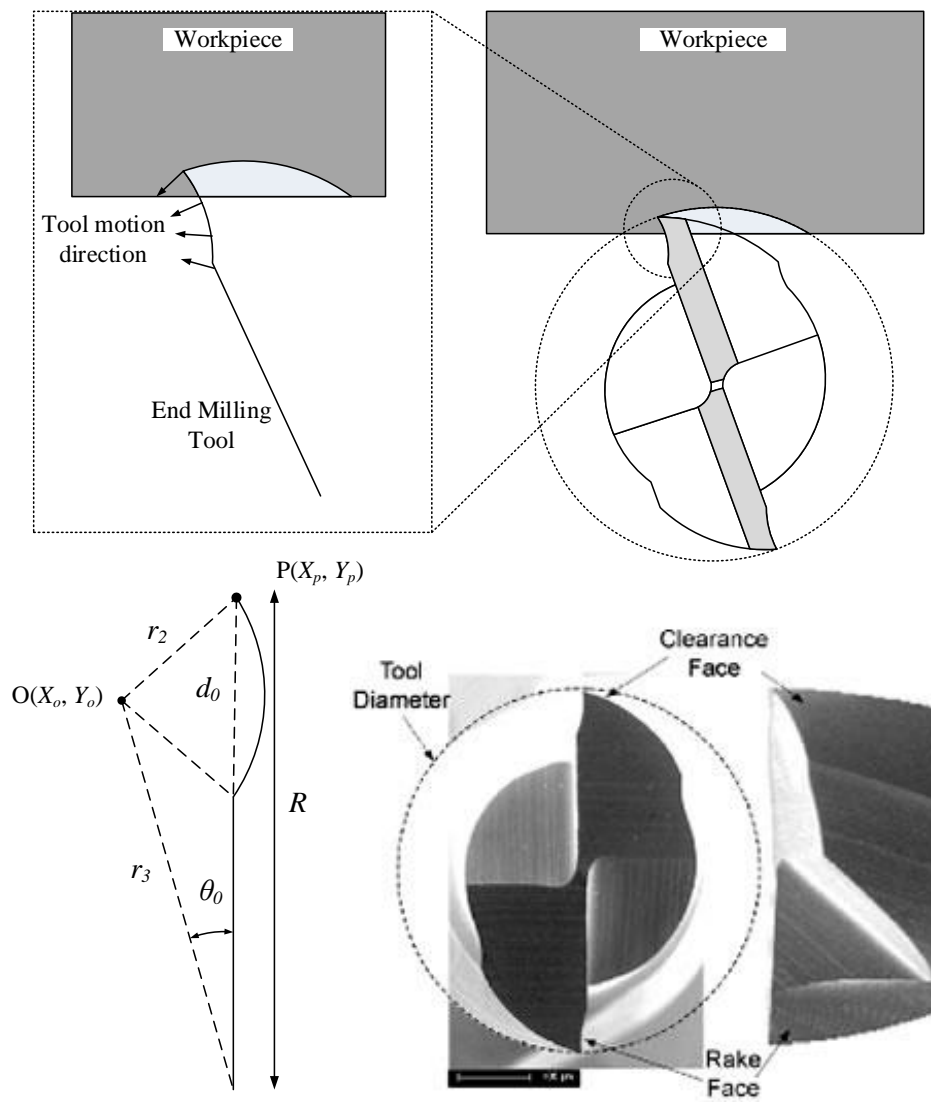
Fig. 3.8 Detail of bottom view of end milling tool in up milling.

The geometric parameters of the cutting tool can be defined by Eq. (3.1) and Eq. (3.2), where r_2 is the hook radius = 1.9 mm and d_0 is the hook length of the cutting tool. In this study, we used a cutting tool diameter of 10 mm. Thus, the hook length is 1.65 mm[14]. r_3 is the distance between the tool center and the center of the hook $O(X_o, Y_o)$.

$$r_3 = \sqrt{\left(R - \frac{d_0}{2}\right)^2 + r_2^2 - \left(\frac{d_0}{2}\right)^2} = \sqrt{R^2 + r_2^2 - Rd_0} \tag{3.1}$$

$$\theta_0 = \tan^{-1}\left(\frac{\sqrt{r_2^2 - \left(\frac{d_0}{2}\right)^2}}{R - \frac{d_0}{2}}\right) \tag{3.2}$$

3.2.2 Entrance burr model in down milling

The cutting tool tip directions are seen to push in at the 1st edge of the workpiece and push out on the 2nd edge of workpiece, as shown in Fig. 3.9. In this case, the Poisson burr model is applied at the 1st edge, and the rollover burr model is applied at the 2nd edge of the workpiece if the point P (X_p, Y_p) is advanced toward the point O (X_o, Y_o), otherwise the Poisson burr model is applied.
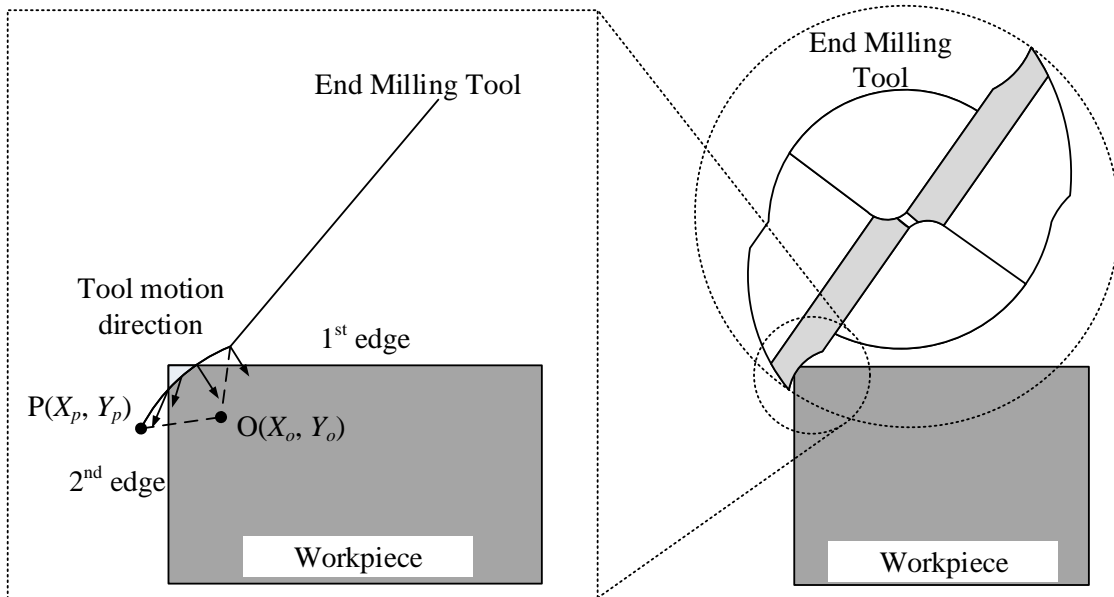
Fig. 3.9 Detail of bottom view of end milling tool in down milling.

3.2.3 Entrance side burr model in up milling and down milling

In both cases (up milling and down milling), the cutting tool is pushed into the workpiece edge, as shown in Fig. 3.3. Thus, the Poisson burr model is applied in each case.

3.2.4 Top burr model in up milling and down milling

According to Gillespie and Blotter[1], the Poisson burr model should be applied for a top burr; however, based on the tool geometry, a modification is needed to increase the accuracy of the burr prediction system. In Figure. 3.10, the red line shows the cutting tool tip blades, which seem to move up because of the helix angle when the tool rotates. For this reason, we assume that the top burr produced is a rollover burr rather than a Poisson burr. Thus, rollover burr models are applied for both down milling and up milling. In addition, the cutting areas in up milling and down milling are different in the case of the top burr view. In down milling, the cutting area is large because the cutting blade is pushed from the outside workpiece edge with a large cutting length and continues to increase the pressure placed on the top edge surface of the workpiece, as shown in Fig. 3.11. In contrast, the cutting areas is small and little pressure on top edge during up milling. The cutting blade starts with a small cutting length and produces less pressure on the top edge, as shown in Fig. 3.12. Thus, the top burr size in down milling will be larger than the top burr size in up milling.
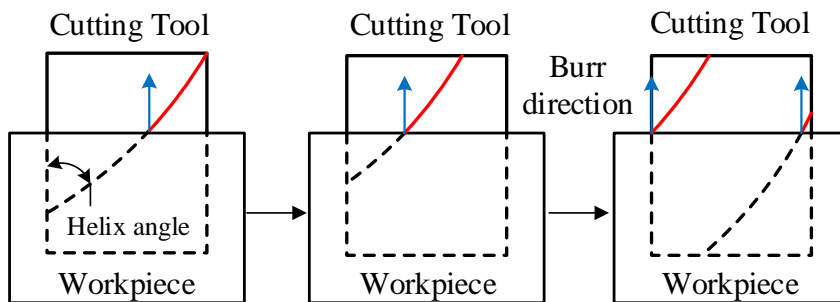
Fig. 3.10 Side view of shoulder end milling[9].

Top View   **Side View**
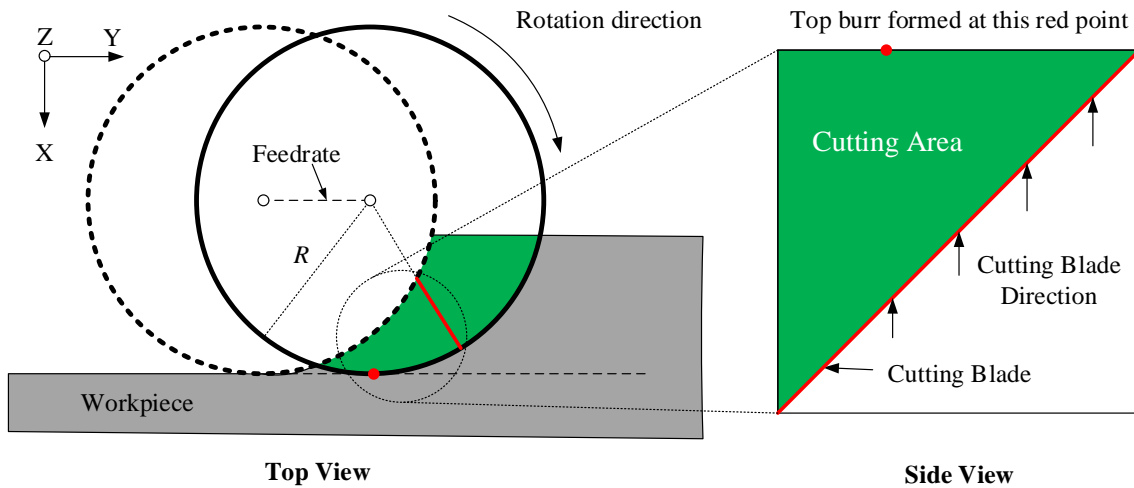
Fig. 3.11 Top burr formed in down milling.

Top View   **Side View**
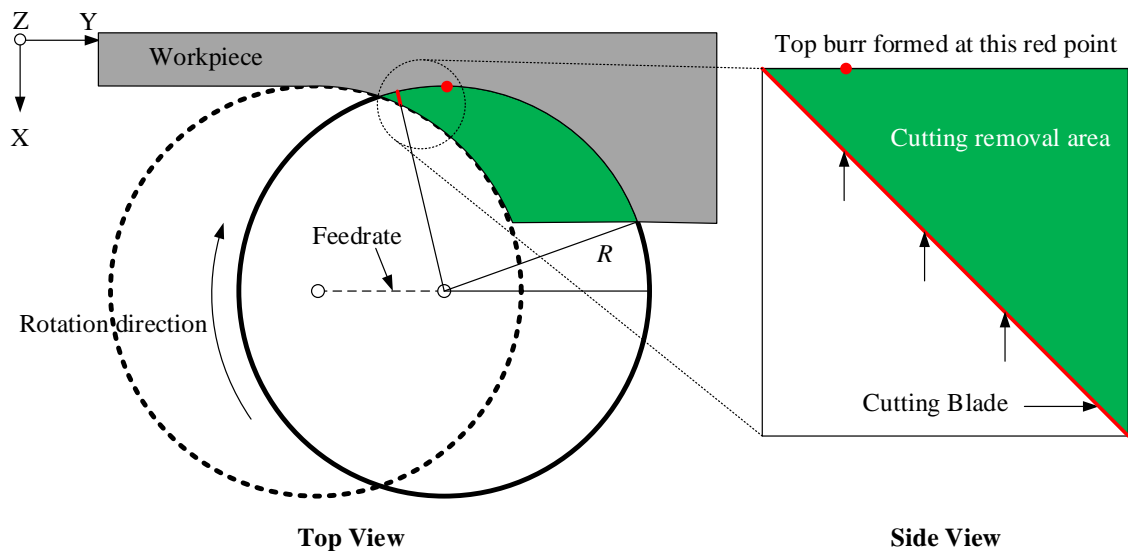
Fig. 3.12 Top burr formed in up milling.

3.2.5 Exit burr model in up milling and down milling

An exit burr is formed when the cutting tool pushes out from the workpiece edge, as shown in Fig. 3.5. Thus, the rollover burr model is used for both up milling and down milling. In the normal rollover burr model, the depth of the cut is assumed to be small. However, when the depth of the cut is large, a modification of this rollover burr is needed. In the case of a large depth of cut, the cutting blades push the removed volume and generate a plastic deformation zone ABC at a point near where the cutting tool leaves the workpiece edge, as shown in Fig.

3.13. The plastic deformation zone ABC was bended around the pivoting point B when the tool was moved forward to the exit surface and the point C was moved to the point D at the final state of a burr development. Thus, the modifications of the burr thickness and burr height can be defined in Eq. (3.3) and Eq. (3.4), respectively.

$$RB_{th} = w \times \tan\beta_0 \tag{3.3}$$

$$RB_h = w \times \tan\phi / \tan\beta_0 \tag{3.4}$$

However, this burr will break because of the ductility of the workpiece material when the equivalent strain at fracture $\varepsilon_f \leq \varepsilon_a$ is the shear strain. Thus, a shear strain criterion is needed to determine whether this burr is formed. This shear strain can be defined in Eq. (3.5). The equivalent strain at fracture ε_f can be define in Eq. (2.8), and w, ϕ, and β_0 can be defined in Eqs. (2.13) and (2.14), (2.6) and (2.18), and (2.15), respectively.

$$\varepsilon_a = [(w + RB_h) \cos\phi - w] / w \tag{3.5}$$
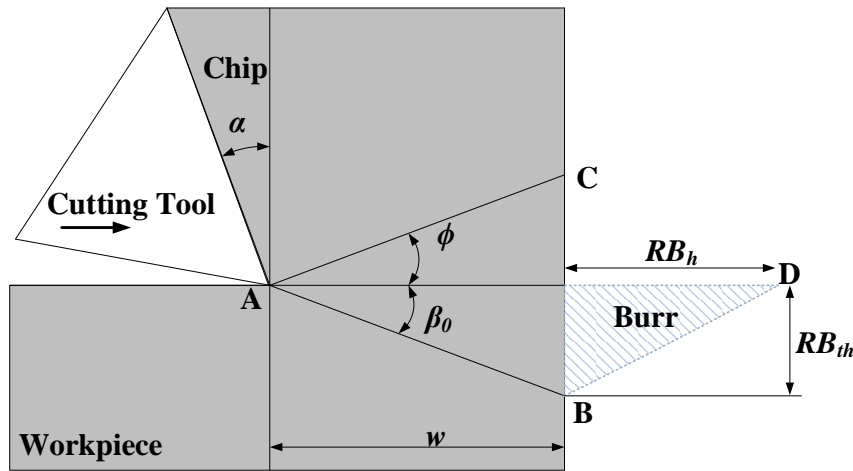
Fig. 3.13 Rollover burr formed when cutting depth is large.

3.2.6 Exit side burr model in up milling and down milling

Exit side burrs are formed, as shown in Fig. 3.6, when the cutting blades push out of the workpiece edge. More than-one cut is required to form these burrs. Based on photo of the surface of a burr, these burrs are formed by multiple cuts of the cutting blades, which turn this burr into a rollover burr, as shown in Fig. 3.14. Thus, the rollover burr model is applied in both up milling and down milling.
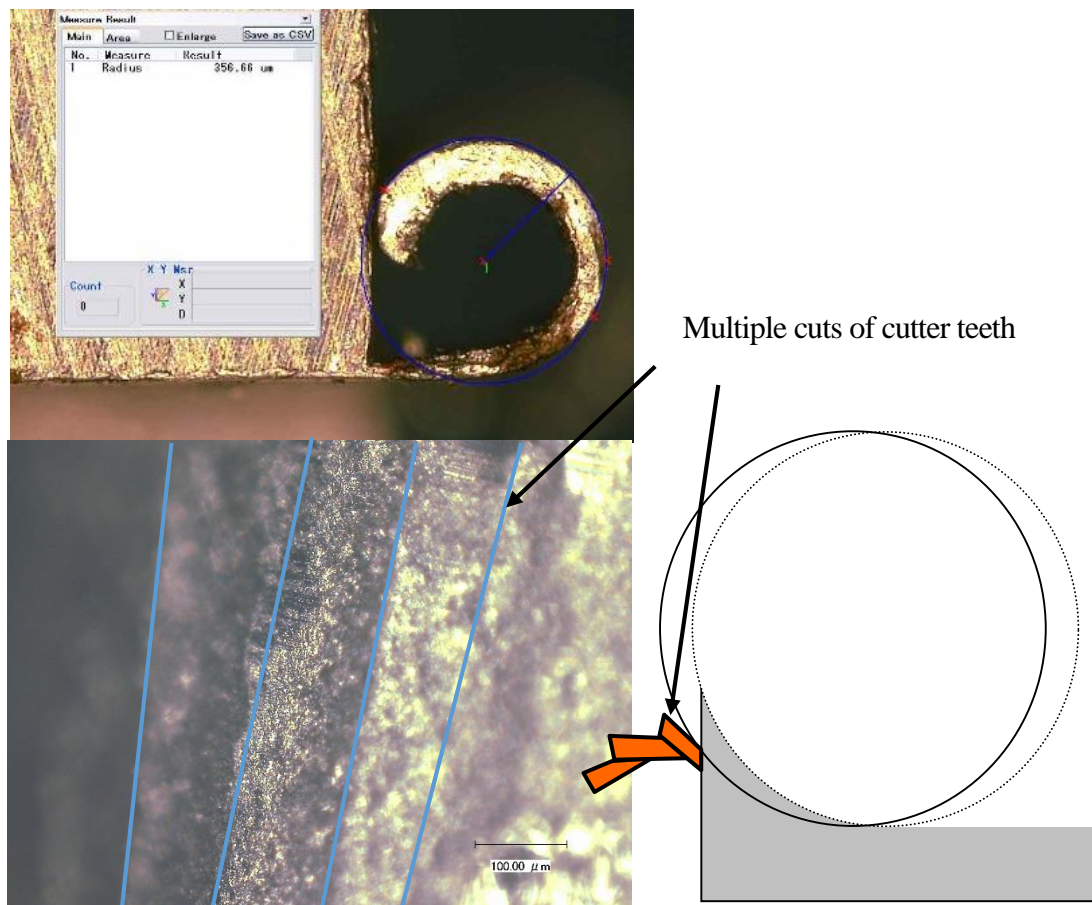
Fig. 3.14 Rollover burr formed at side edge by multiple cuts.

A summary of the burr classifications is given in Table 3.1 and Fig. 3.15.

Table 3.1 Classification for use of burr models.

Burr types	Used burr models	
	Up milling	Down milling
Exit burr	Rollover burr (orthogonal)	Poisson burr (orthogonal)
Side burr	Rollover burr (oblique)	Poisson burr (orthogonal)
Top burr	Rollover burr (oblique)	Rollover burr (oblique)
Entrance burr	Poisson burr (orthogonal)	Poisson burr (orthogonal)
Entrance side burr	Poisson burr (orthogonal)	Poisson burr (orthogonal)
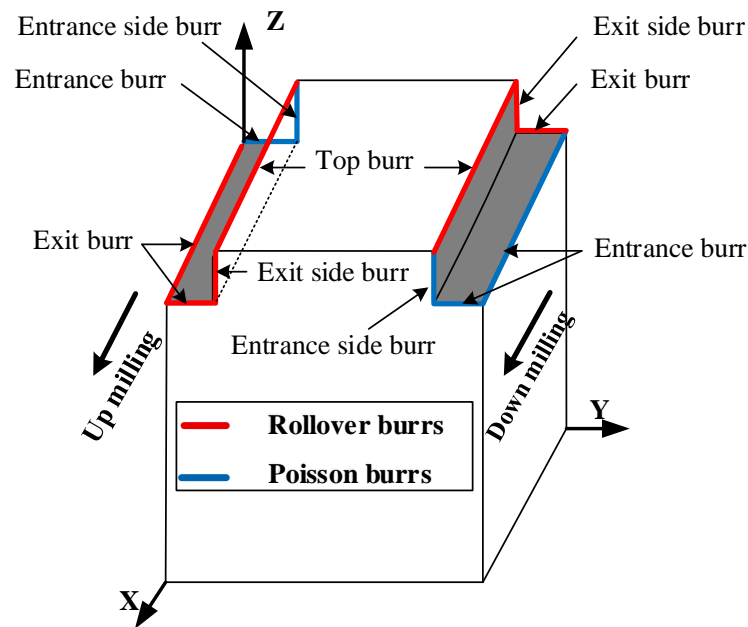
Fig. 3.15 Locations of burrs in shoulder end milling[9].

3.3 Chapter summary

This chapter described the classification of the burrs found in the end milling process. The Poisson burr model and rollover burr model are used for entrance burrs, entrance side burrs, exit burrs, exit side burrs, and top burrs in both up milling and down milling based on their location, tool geometry, and cutting phenomenon . The development of a burr prediction system will be discussed in the next chapter.

CHAPTER 4

4. Development of Burr Prediction System

4.1 System architecture

This chapter presents the development of a burr prediction system for end milling. The proposed approach was implemented in object-oriented software under Windows using C++ Builder[13] and the graphical library OpenGL[14]. The numerical calculation process of the burr prediction system is shown in Fig. 4.1. The input data are from an NC program that was written in the form of G-code and contained in a text file. The system reads information in the text file and uses it in the machining simulator. The burr prediction system, which is called NC simulator, performs with two steps: geometry simulation and physical simulation, as shown in Fig. 4.1. The geometric simulation consists of a geometric model of the workpiece, tool geometry data, and NC data. This simulation is based on a solid modeling system that changes the workpiece geometry with the movement of the tool and removed material. The result of the geometric simulation is the geometric verification of the machined parts; the collision check information about the depth of the cut, width of the cut, and immersion angle; and the reconstruction of the workpiece geometry. Then, the physical simulation is performed using the mechanical and material data of the workpiece, cutting tools, and geometry information provided by the geometric simulation. The physical simulation can instantly estimate the cutting force that will be used to evaluate the burr height and thickness. NC simulator predicts the burr location on a display showing where the burrs were formed and estimates the burr's size based on each position where the burr models were applied.

4.2 Geometric simulation

4.2.1 Z-map model

For end milling, a geometric simulation can be achieved as a Boolean subtraction of the tool swept volume model, which represents the space occupied by the cutting tool motion along the tool path, from the workpiece solid model. The Z-map model is used to construct a solid model of the workpiece and cutting tool. During the simulation, NC data containing thousands of tool positions required as many Boolean subtractions results. To verify the simulation results, real-time visualization is also required in the solid modeling system. The Z-map model is the most suitable form for fulfilling these requirements, because the update part model can be made quickly. A frame map is used to display a graphic image.
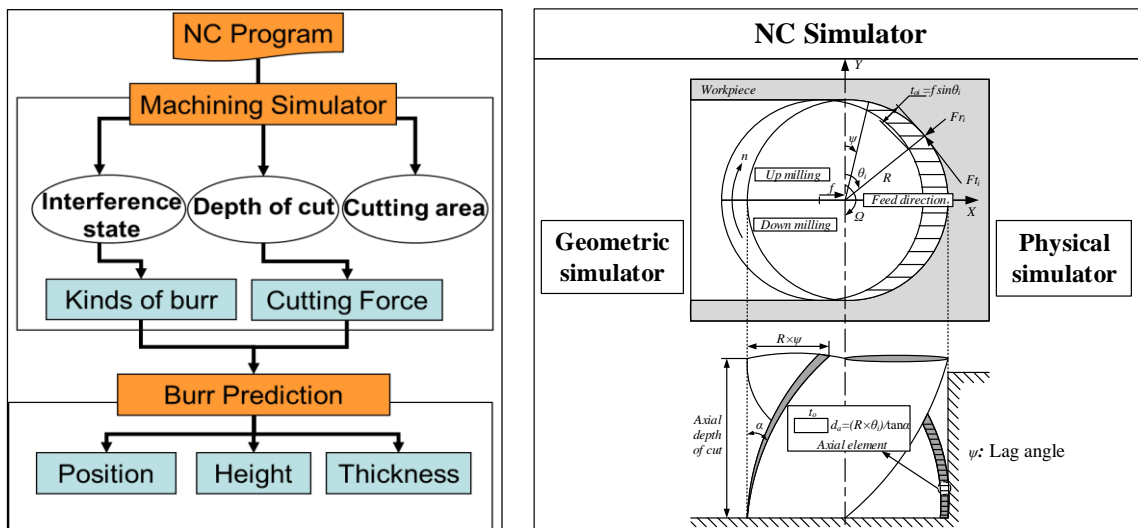
Fig. 4.1 Numerical calculation process.

This frame is organized as an X-Y matrix of memory locations, and each memory location corresponding to a pixel of the display screen contains the color data to be displayed. The pixel coordinates are represented as (X_i, Y_j), where $X_i = dx \times i$, $Y_j = dy \times j$, and dx and dy are the pixel or grid sizes (g), as shown in Fig. 4.3, which should be small in order to display a smooth solid model to represent a workpiece. However, this will increase computation time. In addition, i is the index on the X axis, and j is the index on the Y axis, which have relationships with the length of the workpiece on X axis (a) and length of the workpiece in Y axis (b), as

follow: $0 \le i \le a/dx$ and $0 \le j \le b/dy$. The Z-map values are visible on each pixel surface at a specific height. The Boolean subtraction with the Z-map model can simply be performed during the updating of the Z-map height of each pixel point. For example, when the cutting tool moves over a swept volume along the tool path, the Z-map height update will be performed if the stored value is higher than the surface that is swept by the cutting tool at each interference point between the tool and solid workpiece, as shown in Fig. 4.2. The grid size can be freely selected and has a great effect on the accuracy of the cutting conditions, especially the radial depth of cut d_r as shown in Fig. 4.3. A small grid size provides better accuracy but increases the computation time. In this study, a grid size $g = 0.05$ mm was used. The workpiece had a cube shape ($a = b = 20$ mm) with height $W_h = 30$ mm and cutting tool rake angle $\alpha = 30^o$.

Z-map height update = Z-map height initial – Depth of cut
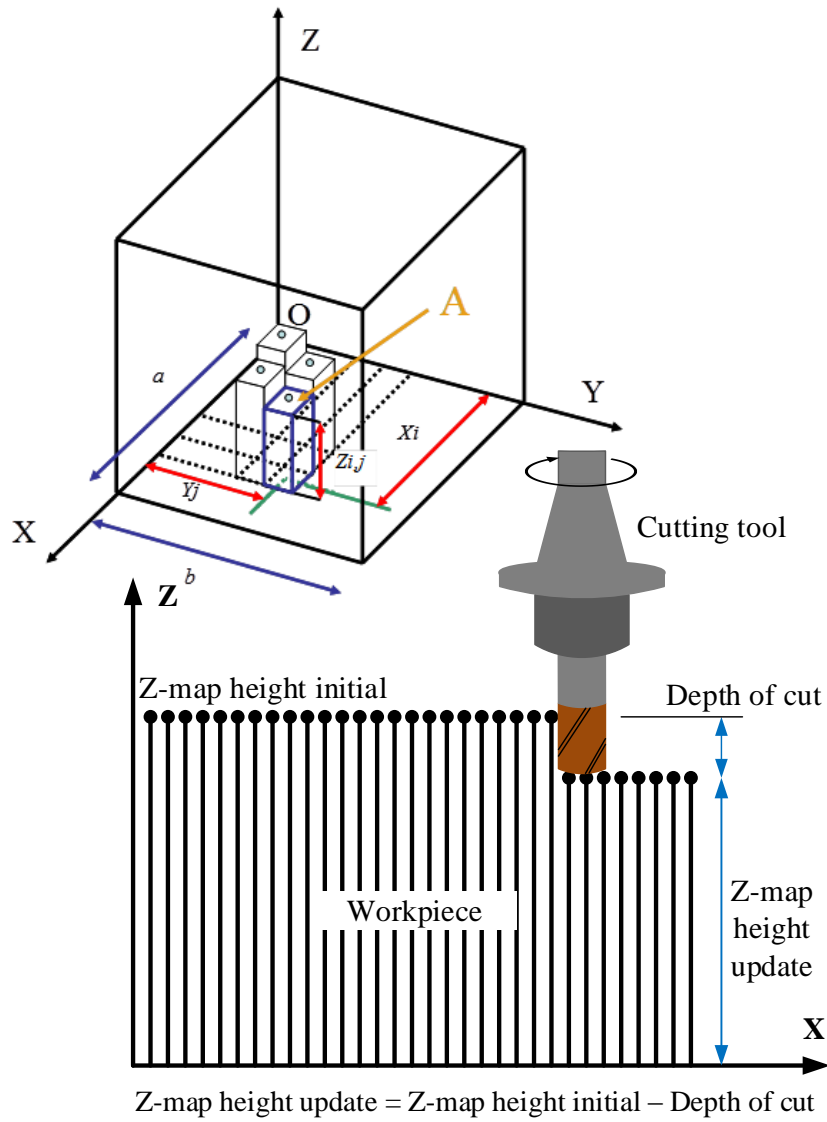
Fig. 4.2 Boolean subtraction with Z-map model.

Grid center points by
2D arrays of Z-map

(X+1, Y+1)	(X+1, Y)	(X+1, Y-1)
(X, Y+1)	(X, Y)	(X, Y-1)
(X-1, Y+1)	(X-1, Y)	(X-1, Y-1)

g

Workpiece (top view)

Vector tool
feed direction

Rotation
Direction

Feed rate

$\vec{d_r}$
(up milling)

$\vec{d_r}$
(down milling)

X

Y

$P(X_p, Y_p)$

$O(X_o, Y_o)$

Up Milling

Vector tool
feed direction

Down Milling

Hook

Z

Y

X

dx

dy
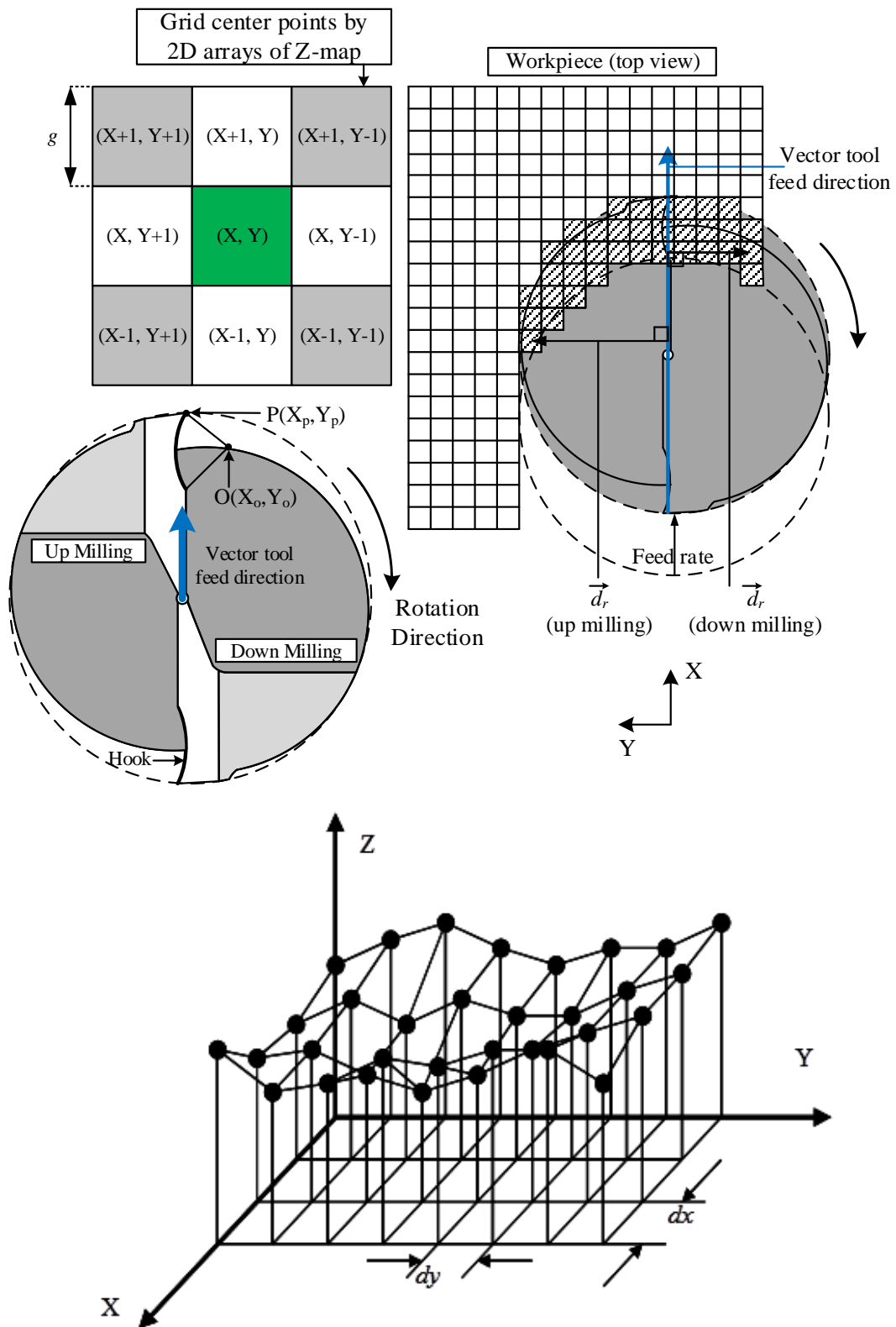
Fig. 4.3 Z-map model used to represent workpiece[9].

4.2.2 NC program analysis model

The analysis model was developed to read and store the information from the G-code syntax. This analysis model can recognize the G-code syntax such as the G function, M function, and coordinate letters X, Y, Z, along with the cutting condition. This G-code or NC program provides the command information for the NC machine to move base on the input code. In this study, the NC program analysis model had the ability to translate the NC code and send information to the geometric simulator to execute the simulation process display. The G-code functions that the NC program analysis model can recognize are listed in Table 4.1.

Table 4.1 G-code functions[15].

Code	Functions	Description
G00	Fast forward	Move fast forward to the specified coordinates from the current position.
G01	Linear interpolation	Move in a straight line at the specified feed rate to the specified coordinates from the current position.
G02	Circular interpolation	Move in the clockwise direction with the specified feed rate to the specified coordinates.
G03	Circular interpolation	Move in the counterclockwise direction with the specified feed rate to the specified coordinates.
M00	Compulsory program stop	Stop the execution of the program.
M03	Spindle rotation normal	Rotate the spindle in the clockwise direction.
M30	Program end	Represents the end of the program. It is always used with reset and rewind.

The NC code is written in text file (.txt) and included in the program folder. The NC program analysis model read the information contained in that text file. The flow of the program execution can be described as follows:

1. Create a two-dimensional matrix array to store the G code information,
2. Read a line of code in the text file and store it in the matrix,
3. Copy that information and update the information for the next line to use,
4. Read the next line and save it in the matrix, and
5. Repeat steps 3 and 4 until finished with the code in the text file.

4.3 Physical simulation

In the physical simulation, the cutting force at a certain instance is calculated using a force model. This force model is based on the axial depth of cut, cutting areas, and cutting constant. In this study, three patterns for the cutting process simulation are discussed for force model development, including the entrance pattern, ready pattern, and exit pattern of the cutting tool from the workpiece. These patterns were applied for both up milling and down milling.

4.3.1 Cutting length calculation
(1) Entrance pattern

In this pattern, the cutting tool starts to approach the workpiece edge as shown in Fig. 4.4. The cutting lengths vary between points a and b, b and c, and c and d, as represented by $L_{a\text{-}b}$, $L_{b\text{-}c}$, and $L_{c\text{-}d}$, respectively and can be defined by Eq. (4.1) to Eq. (4.3), respectively.

$$L_{a-b} = R - \frac{\min a}{\sin \alpha_a} \tag{4.1}$$

$$L_{b-c} = R + f \cos \alpha_b - \sqrt{R^2 - f^2 \sin^2 \alpha_b} \tag{4.2}$$

$$L_{c-d} = R - \frac{\min b}{\cos \alpha_c} \tag{4.3}$$

Top View
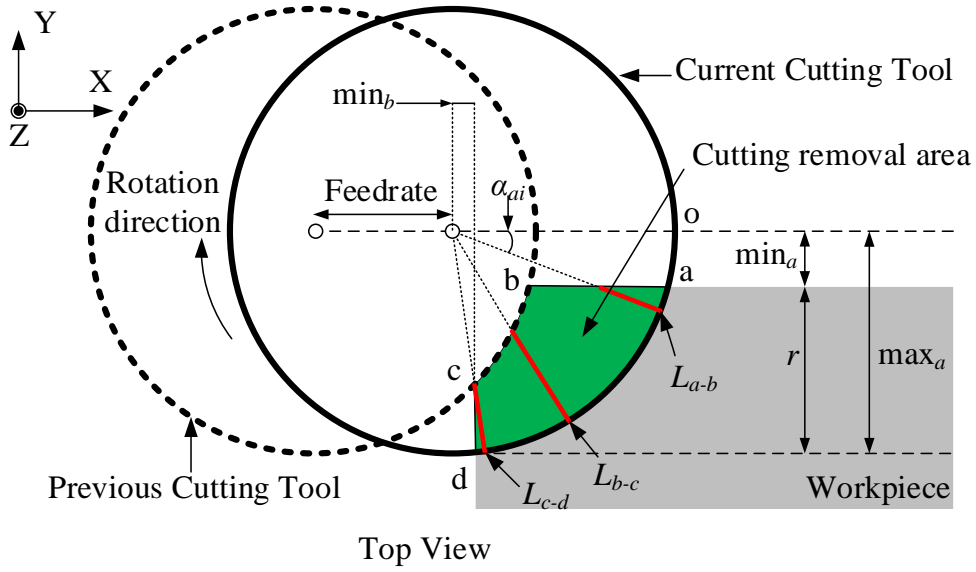
Fig. 4.4 Cutting length in each segment at entrance pattern of cutting tool.

where R is the cutting tool radius; f is feed rate; and α_a, α_b, and α_c can be found using Eq. (4.4) to Eq. (4.6), respectively.

$$\alpha_a = \sin^{-1}\left(\frac{\min a}{R}\right) \tag{4.4}$$

$$\alpha_b = \tan^{-1}\left(\frac{\min a}{\sqrt{R^2 - \min a^2} - f}\right) \tag{4.5}$$

$$\alpha_c = \tan^{-1}\left(\frac{\sqrt{R^2 - \left(f + \min b^2\right)}}{\min b}\right) \tag{4.6}$$

(2) Ready pattern

In this pattern, the cutting tool fully engages the workpiece, as shown in Fig. 4.5. Two cutting lengths vary, in the segments from point a to b and b to c ($L_{a\text{-}b}$ and $L_{b\text{-}c}$), which can be defined in Eq. (4.7) and Eq. (4.8), respectively.
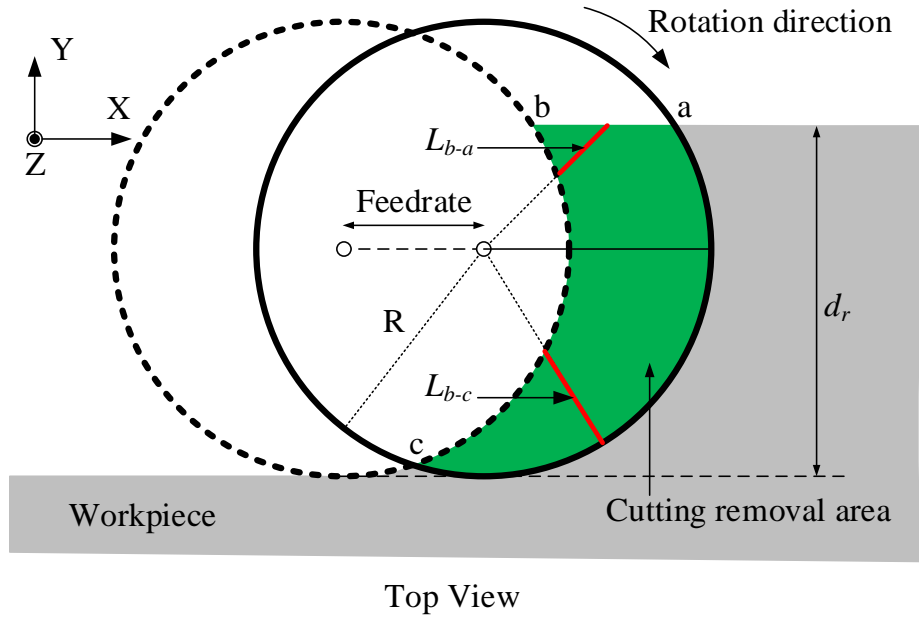
Fig. 4.5 Cutting length in each segment at ready pattern of cutting tool.

$$L_{a-b} = R + \frac{d_r - R}{\sin \alpha_a} \qquad (4.7)$$

$$L_{b-c} = R + f \cos \alpha_b - \sqrt{R^2 - f^2 \sin^2 \alpha_b} \qquad (4.8)$$

where α_a and α_b can be found using Eq. (4.9) and Eq. (4.10), respectively.

$$\alpha_a = \sin^{-1}\left(\frac{R - d_r}{R}\right) \qquad (4.9)$$

$$\alpha_b = \tan^{-1}\left(\frac{d_r - R}{\sqrt{R^2 - (R - d_r)^2} - f}\right) \qquad (4.10)$$

(3) Exit pattern

In this pattern, the cutting tool is close to the exiting the workpiece edge, as shown in Fig. 4.6. The cutting lengths vary between points a and b, and b and c, as represented by L_{a-b}, and L_{b-c}, respectively and can be defined by Eq. (4.11) and Eq. (4.12), respectively.
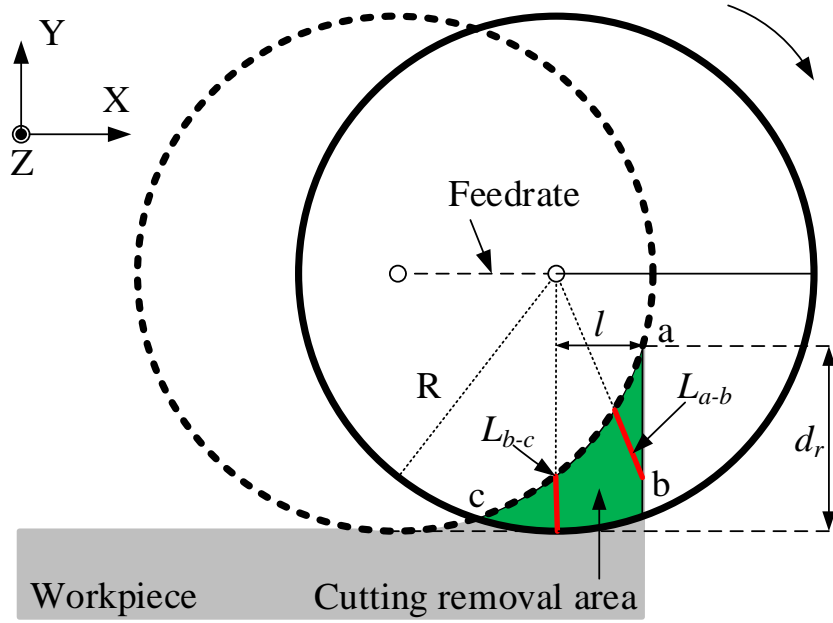
Fig. 4. 6 Cutting length in each segment at exit pattern of cutting tool.

$$L_{a-b} = \frac{l}{\cos \alpha_a} + f \cos \alpha_a - \sqrt{R^2 - f^2 \sin^2 \alpha_a} \qquad (4.11)$$

$$L_{b-c} = R + f \cos \alpha_b - \sqrt{R^2 - f^2 \sin^2 \alpha_b} \qquad (4.12)$$

where α_a and α_b can be found using Eq. (4.13) and Eq. (4.14), respectively, and l is the distance from the current cutting tool position to the exit point at the workpiece edge.

$$\alpha_a = \cos^{-1}\left(\frac{l}{\sqrt{(R - d_r)^2 + l^2}}\right) \qquad (4.13)$$

$$\alpha_b = \cos^{-1}\left(\frac{l}{R}\right) \qquad (4.14)$$

4.3.2 Axial and radial depth of cut calculation

The cutting conditions, including the axial depth of the cut and radial depth of the cut are important parameters that are necessary for calculating the cutting areas. These parameters are varied in value sequentially in the actual processing. In this study, a simulation process was developed by assuming that the actual process is the amount involves the number of interference points between the cutting tool and workpiece. Because the Z-map model was used, the calculation of the axial depth of the cut was easy to obtain, as shown in Fig. 4.2. The radial depth of cut could be calculated based on any interference points. In Figure 4.7, the cutting tool has the previous coordinate (X_1, Y_1, Z_1). At a certain feed rate, the cutting tool moves to coordinate (X_2, Y_2, Z_2) and sweeps an area of the workpiece that contains many interference points. The dots represent grid points that are coordinates on the Z-map. The radial depth of cut can be defined based on the concept of the distance between two points.
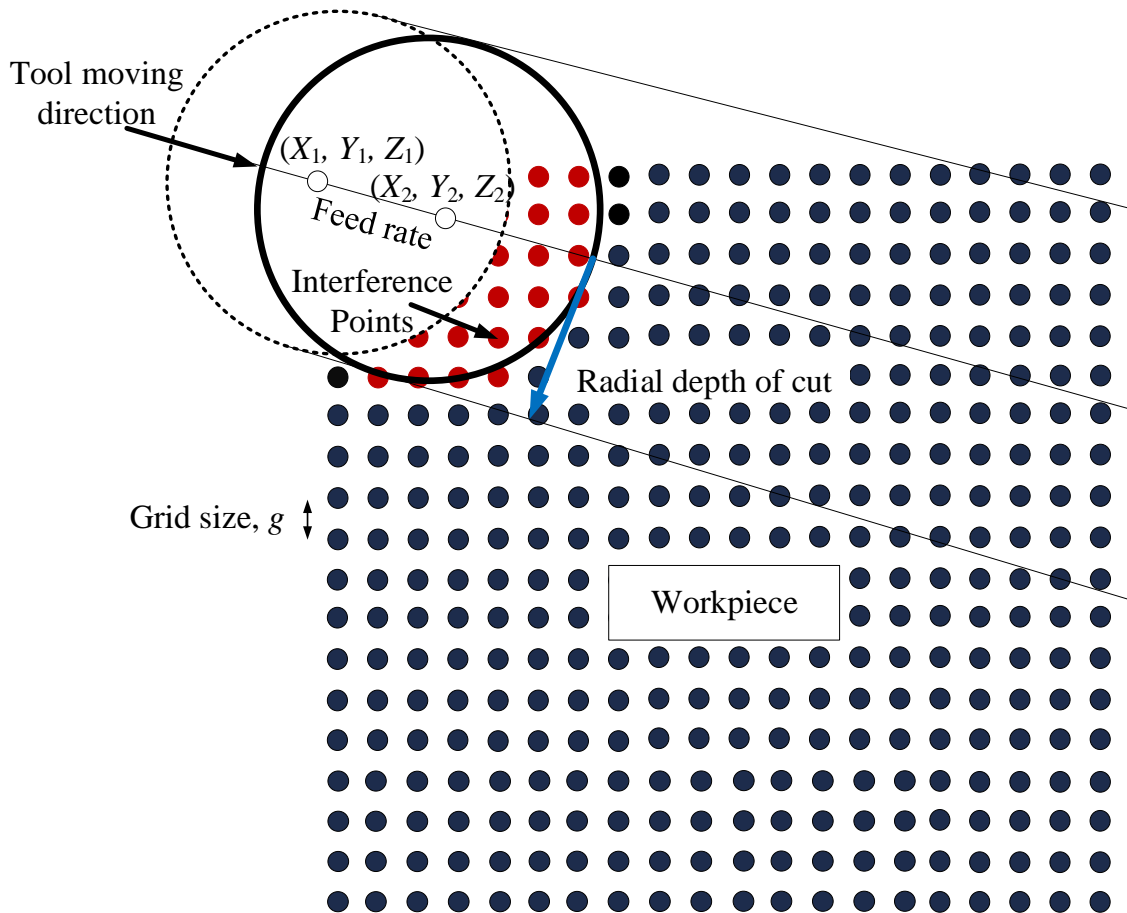
Fig. 4.7 Method for calculating radial depth of cut.

In order to clarify the up milling and down milling in the system, the cutting tool cross section is divided into two areas: area A and area B. Area A represents up milling while area B represents down milling. The sign of the vector product of $\overrightarrow{V_1}$ and $\overrightarrow{V_2}$ is used to distinguish areas A and B. $\overrightarrow{V_1}$ is the vector formed by the previous tool coordinate and current tool coordinate, as shown in Fig. 4.8 (a). $\overrightarrow{V_2}$ is the vector formed by the current tool coordinate and any interference points in area A or area B. If the sign of the vector product is positive, area A is assigned otherwise area B is assigned. Figure 4.8 (b) shows an example of the radial depth of cut calculation. First, the system defines the sign of the vector product as positive. Second, it calculates the L_{min} between the current tool coordinate and interference point I_p. The radial depth of cut is obtained by finding the different between tool radius and this L_{min}.
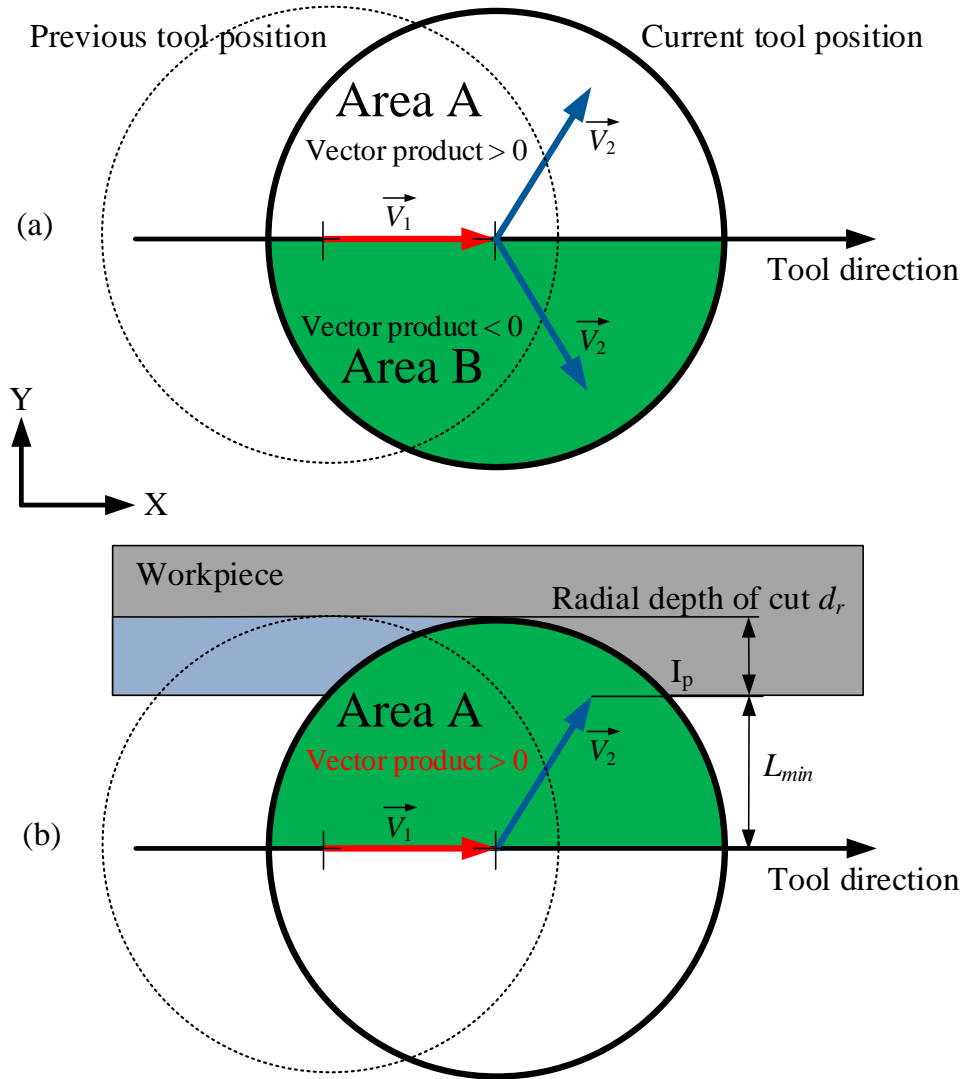
Fig. 4.8 Method for distinguishing area A or area B.

In the full cutting pattern, areas A and B both exist. Thus, some additional conditions are needed. First, the system checks the cross product vector sign to identify the area. If both areas (A and B) exist, the system will check their sizes. If area A is bigger than area B, there are two possibilities: no interference with area B or interference with area B. If the system detects that there is no interference with area B, the L_{min} is calculated, and the radial depth of cut $= R - L_{min}$. The diagram used for this judgement is shown in Fig. 4.9. A summary of the flow chart for calculating the radial depth of cut is shown in Fig. 4.10.
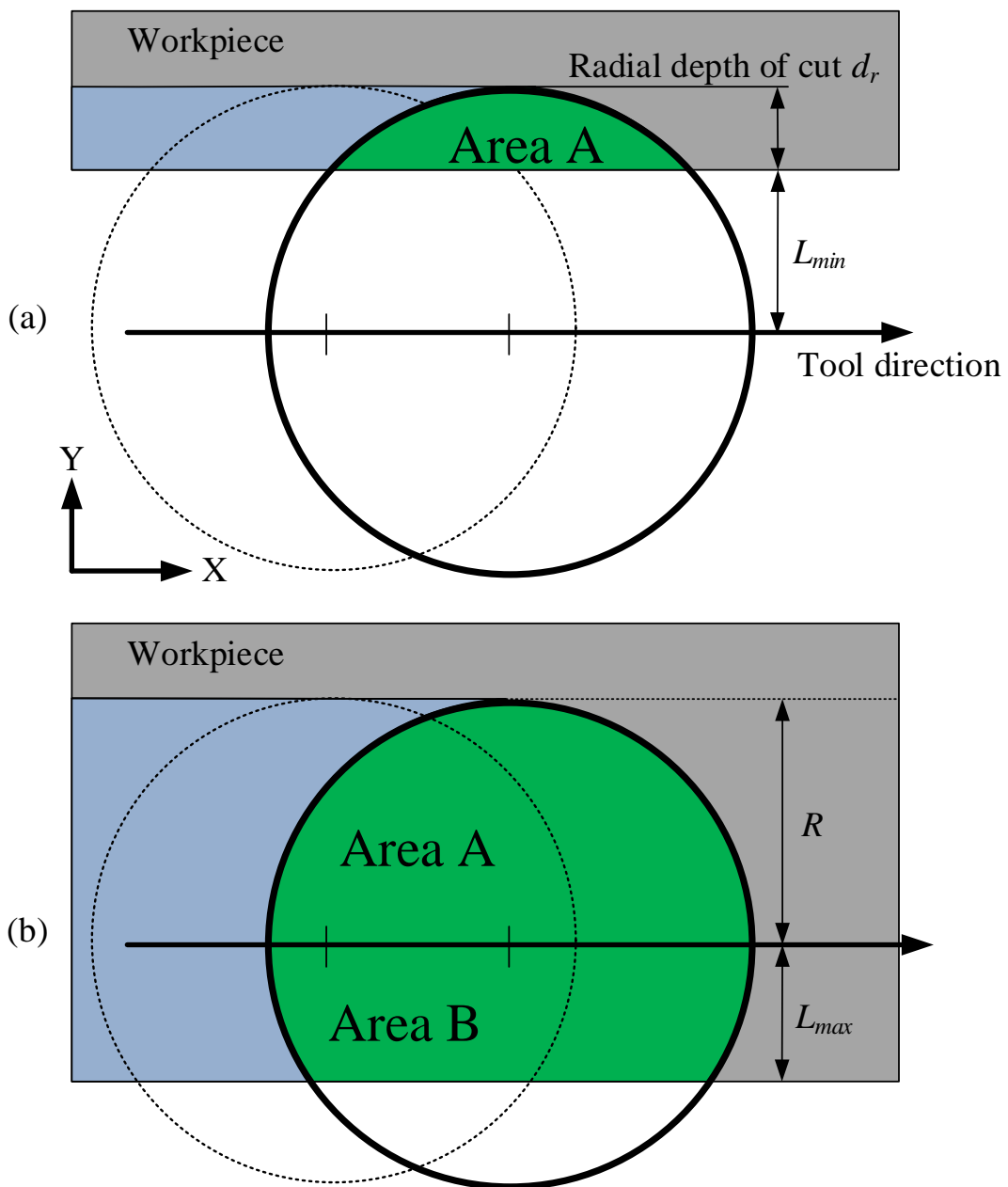
Fig. 4.9 Method for calculating radial depth of cut.
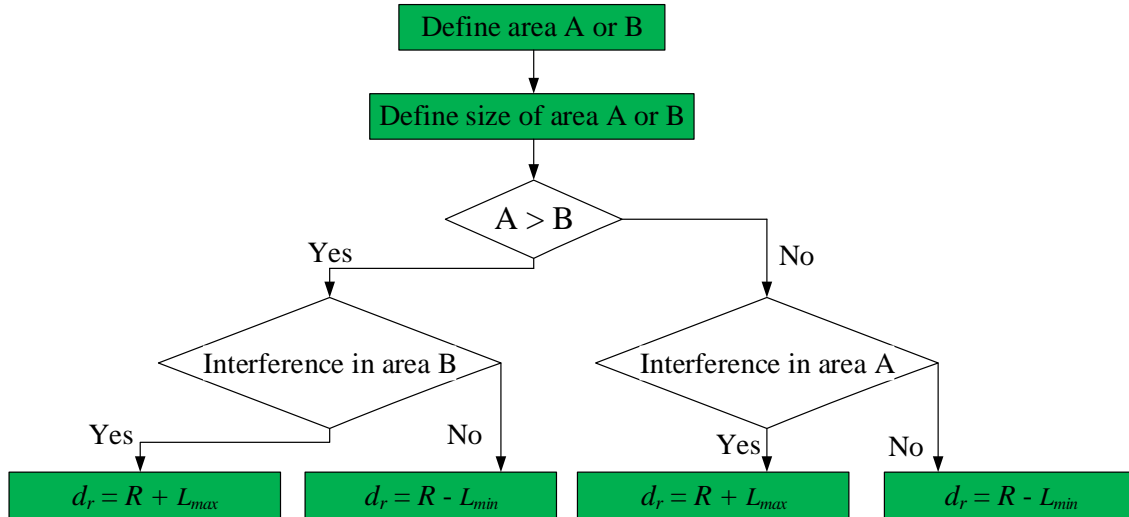
Fig. 4.10 Flowchart for calculating radial depth of cut.

4.3.3 Cutting area calculation

In this study, we adopted a model in which the cutting area is divided into small sections along the axis based on cutting length L_i and axial depth of cut d_{ai}. The cutting area at a specific point, as point i, is defined in Eq. (4.15).

$$S_i = L_i \times d_{ai} \tag{4.15}$$

The cutting length can be defined as shown in Eqs. (4.1) to Eq. (4.14) based on each pattern. Because the cutting tool has rake angle α, the axial depth of cut d_{ai} can be defined as shwon in Eq. (4.16).

$$d_{ai} = (R \times \theta_i) / \sin \alpha \tag{4.16}$$

where θ_i is the immersion angle or rotation angle at the current cutting point.

4.3.4 Cutting force calculation

End milling tools are the most common tools used in industry and usually have many flutes. In this study, typical flat end milling with two flutes was used. The instantaneous cutting force acting on each cutting flue can be simply represented using three forces components, namely the tangential force $dF_t(\theta_i)$, radial force $dF_r(\theta_i)$, and axial force $dF_a(\theta_i)$. It can be defined using two methods, one that uses cutting constant from the results of an experiment and one based on the cutting force model proposed by Armarego and Brown[16].

(1) First method of cutting force calculation

In this method, the total cutting force is calculated based on two force components, normal force N and friction force P, as in Eq. (4.17). In addition, friction force P is the force acting on the rake face of the cutting tool, which occurs in the secondary shear zone. It can be calculated using the normal force and coefficient of friction μ, as shown in Eq. (4.18). The normal force N is defined by cutting constant K_s and cutting area S_i, as shown in Eq. (4.19).

$$F = \sqrt{N^2 + P^2} \tag{4.17}$$

$$P = N \times \mu \tag{4.18}$$

$$N = K_s \times S_i \tag{4.19}$$

The cutting constant K_s is dependent on both the cutting conditions and workpiece material. In this method, cutting constant K_s is determined through experimental tests[17]. As shown in Figure 3.11, F_{xy}, F_x, F_y, and F_z, are cutting force projections on the (X, Y) plane, X axis, Y axis, and Z axis, respectively, and are defined in Eq. (4.20) to Eq. (4.24). The cutting force F acting on the tool rake face is the main cutting force. The other cutting force components: F_{xy}, F_x, F_y, and F_z, are the components of the cutting forces in the X-Y, X, Y, and Z cutting directions, respectively.
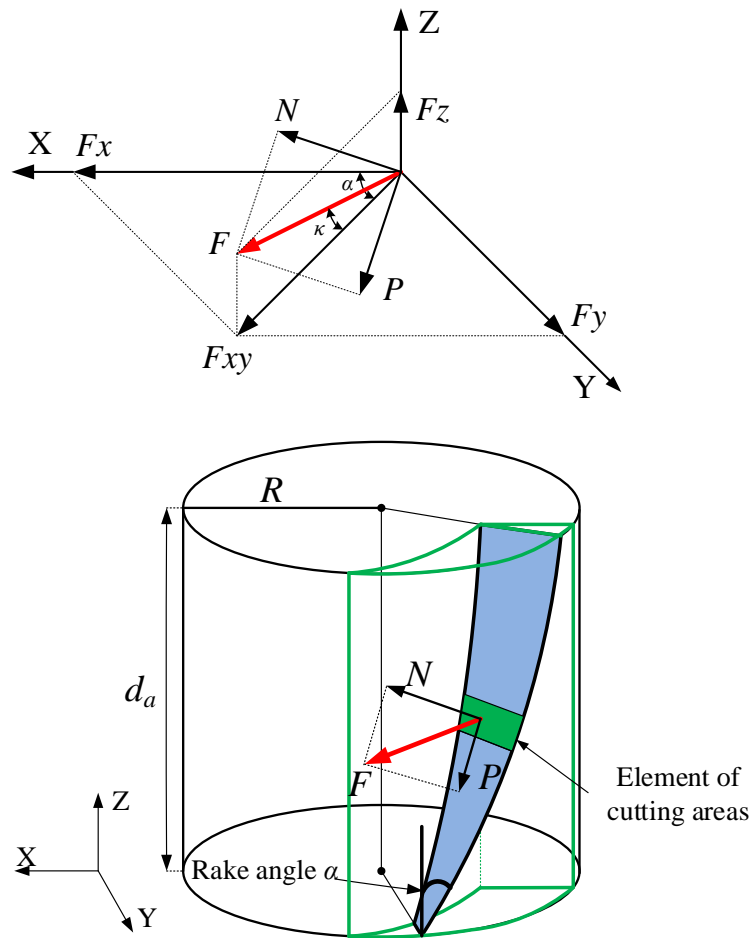
Fig. 4.11 Cutting force definition for tool rake face[9].

$$F_{xy} = F \times \cos \kappa \qquad (4.20)$$

$$F_x = F_{xy} \times \cos \alpha \qquad (4.21)$$

$$F_y = F_{xy} \times \sin \alpha \qquad (4.22)$$

$$F_z = F \times \sin \kappa \qquad (4.23)$$

$$\kappa = \tan^{-1}(1/\mu) - (\pi/2 - \alpha) \qquad (4.24)$$

(2) Second method of cutting forces calculation

In this method, the three cutting force components, the tangential force $dF_t(\theta_i)$, radial force $dF_r(\theta_i)$, and axial force $dF_a(\theta_i)$, as shown in Fig. 4.12, are the cutting forces acting on a chip element that is removed, and the summing-up of the cutting forces acting on the integrated axial depth of cut ($\Delta d_{ai} = d_a/n_a$) can be given in Eq. (4.25)[18]

$$
\begin{cases}
dF_t(\theta_i) = \displaystyle\sum_{j=1}^{n_a} [(K_{tc}t_{0i} + K_{te})\Delta d_{ai}]_j \\[2mm]
dF_r(\theta_i) = \displaystyle\sum_{j=1}^{n_a} [(K_{rc}t_{0i} + K_{re})\Delta d_{ai}]_j \\[2mm]
dF_a(\theta_i) = \displaystyle\sum_{j=1}^{n_a} [(K_{ac}t_{0i} + K_{ae})\Delta d_{ai}]_j
\end{cases}
\qquad (4.25)
$$

where K_{tc}, K_{rc}, and K_{ac} are the cutting constants in the tangential, radial, and axial directions, respectively, and K_{te}, K_{re}, and K_{ae} are the corresponding edge coefficients. n_a is the number of axial integration steps, and d_a is the axial depth of cut.
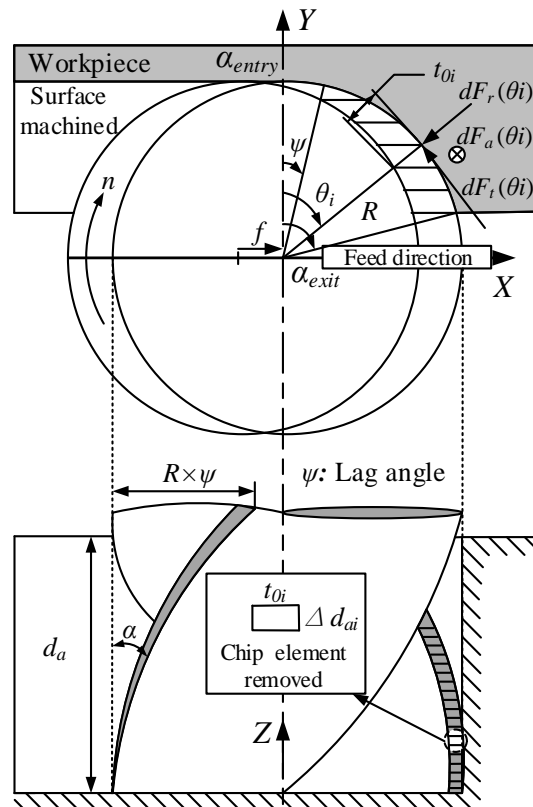
Fig. 4.12 Cutting force model in up milling[26].

Figure 4.12. shows the geometry of the chip thickness in up milling with the side view of the cutting tool slicing into the small chip elements that are removed. The chip thickness t_{0i} varies as a function of the immersion or rotation angle θ_i for flute i at axial depth of cut d_{ai}. The immersion angle is measured in the clockwise direction. The instantaneous effective chip thickness is expressed as[19]

$$t_{0i} = R + f\sin(\theta_i - d_{ai}\frac{\tan(\psi)}{R}) - \sqrt{R^2 - \left(f\cos(\theta_i - d_{ai}\frac{\tan(\psi)}{R})\right)^2} \qquad (4.26)$$

where R is the cutting tool radius, $f = f_L / (n \times N)$ is the feed rate per tooth[15], f_L is the linear feed rate in millimeters per minute, n is the spindle speed in rotations per minute, N is the number of cutting edges (flutes), $\psi = d_{ai} \times \tan(\gamma) / R$ is the lag angle, γ is the helix angle, and θ_i is the immersion or rotation angle for flute i, which can be defined as

$$\theta_i = \theta_0 + (i-1)\theta_p - \psi \qquad (4.27)$$

where $\theta_0 = \alpha_{entry} + \Delta\theta$ is the immersion angle of the flute's bottom edge, $\Delta\theta$ is the cutter rotation angle increment, and $\theta_p = 2\pi/N$ is the pitch angle. The elemental cutting forces can be resolved in the X, Y, and Z direction as follows

$$\begin{pmatrix} dF_x(\theta_i) \\ dF_y(\theta_i) \\ dF_z(\theta_i) \end{pmatrix} = \begin{pmatrix} -\cos\theta_i & -\sin\theta_i & 0 \\ \sin\theta_i & -\cos\theta_i & 0 \\ 0 & 0 & 1 \end{pmatrix} \times \begin{pmatrix} dF_t(\theta_i) \\ dF_r(\theta_i) \\ dF_a(\theta_i) \end{pmatrix} \qquad (4.28)$$

These cutting forces are produced only when the cutting tool is in the cutting zone, that is, $dF_x(\theta_i)$, $dF_y(\theta_i)$, $dF_z(\theta_i) > 0$, which means that $\theta_{entry} \le \theta_i \le \theta_{exit}$. θ_{entry} and θ_{exit} are the cutter entry and exit angles, respectively, and can be defined using the width of cut d_r and R as follow:

$$\begin{cases} \theta_{entry} = \begin{cases} 0 & up \quad milling \\ \pi - \cos^{-1}(1 - d_r / R) & down \quad milling \end{cases} \\ \theta_{exit} = \begin{cases} \cos^{-1}(1 - d_r / R) & up \quad milling \\ \pi & down \quad milling \end{cases} \end{cases} \qquad (4.29)$$

The total feed, normal, and axial forces acting on the cutter at a given rotation angle θ_i can be found by summing up the cutting force contributions as follows:

$$F_x(\theta_i) = \sum_{i=1}^{N} dF_x(\theta_i); \ F_y(\theta_i) = \sum_{i=1}^{N} dF_y(\theta_i); \ F_z(\theta_i) = \sum_{i=1}^{N} dF_z(\theta_i) \tag{4.30}$$

The instantaneous resultant cutting force on the end milling tool is defined in Eq. 4.31. In orthogonal cutting, the cutting force along the tool axis is zero, $F_z(\theta_i) = 0$.

$$F = \sqrt{F_x^2(\theta_i) + F_y^2(\theta_i) + F_z^2(\theta_i)} \tag{4.31}$$

In this method, the cutting constants and edge coefficients[20] in the orthogonal cutting model are expressed as follows:

$$\begin{cases} K_{tc} = k_0 \dfrac{\cos(\lambda - \alpha)}{\sin\phi \cos(\phi + \lambda - \alpha)} \\[2mm] K_{rc} = k_0 \dfrac{\sin(\lambda - \alpha)}{\sin\phi \cos(\phi + \lambda - \alpha)} \\[2mm] K_{te} = R_e k_0 (\dfrac{2\theta_s}{\cos\theta_s} + \pi \sin\theta_s \tan\theta_s) \\[2mm] K_{re} = 2\sqrt{3} R_e k_0 \sin\theta_s \end{cases} \tag{4.32}$$

The estimations of the cutting constants in the oblique cutting model are applied from the cutting model proposed by Merchant[21] and the orthogonal to oblique transformation proposed by Armarego and assuming that the Stabler rule[18] is correct (chip flow angle $\eta = $ inclination angle i).

$$\begin{cases} K_{tc} = \dfrac{k_0}{\sin\phi_c} \times \dfrac{\cos(\lambda - \alpha_c) + \tan i \tan\eta \sin\lambda}{\sqrt{\cos^2(\phi_c + \lambda - \alpha_c) + \tan^2\eta \sin^2\lambda}} \\[3mm] K_{rc} = \dfrac{k_0}{\sin\phi_c \cos i} \times \dfrac{\sin(\lambda - \alpha_c)}{\sqrt{\cos^2(\phi_c + \lambda - \alpha_c) + \tan^2\eta \sin^2\lambda}} \\[3mm] K_{ac} = \dfrac{k_0}{\sin\phi_c} \times \dfrac{\cos(\lambda - \alpha_c)\tan i - \tan\eta \sin\lambda}{\sqrt{\cos^2(\phi_c + \lambda - \alpha_c) + \tan^2\eta \sin^2\lambda}} \\[3mm] K_{te} = R_e k_0 (\dfrac{2\theta_s}{\cos\theta_s} + \pi \sin\theta_s \tan\theta_s) \\[3mm] K_{re} = 2\sqrt{3} R_e k_0 \sin\theta_s \\[2mm] K_{ae} = K_{te} \sin i \end{cases} \tag{4.33}$$

By adopting the prediction of the shear angle model proposed by Wright's[22] and using the von Mises or the Tresca theory, along with shear angles ϕ and ϕ_c from Eq. (2.6) and Eq. (2.18), respectively, θ_s is the stagnation or neutral point angle and has a value between -57° and -65°, accoding to Woon[10] and Yen[11]. In addition, $k_0 = \sigma_y/\sqrt{3}$ is the yield shear strength, σ_y is the yield strength of the workpiece, λ is the friction angle obtained from $\lambda = \arctan\mu$, and μ is the coefficient of friction.

The rake angle α was replaced by the effective rake angle α_{eff}, which depends on the relationship between uncut chip thickness c and effective cutting edge radius R_e as follows:[23]

$$\alpha_{eff} = \begin{cases} -\dfrac{\pi}{2} + \cos^{-1}\left(1 - \dfrac{c}{R_e}\right) & if\ c{\leq}h_t \\ \alpha & if\ c{>}h_t \end{cases}$$

$$h_t = R_e\left(1 - \cos\left(\alpha + \frac{\pi}{2}\right)\right)$$

(4.34)

4.4 Burr prediction

The burr prediction module is described in this section. This prediction module identifies the type of burrs using the relation of the interference point position and Z-map grid coordinates.

4.4.1 Identification of burr formed using NC simulation

When interferences occurs between the cutting tool and workpiece, NC simulator starts to identify which type of burr will form by comparing the Z-map height at the coordinates of the grid point with the Z-map height at the coordinates of the interference point, as shown in Fig. 4.13.

4.4.2 Identification of top burrs and applies formula

To identify the top burrs, NC simulator will compare the Z-map height at grid point coordinate Z ($\pm x$, $\pm y$) with the Z-map height at interference point Ip as shown in Fig. 4.14.

Fig. 4.13 Grid point coordinate and interference point Ip.

(a) Judgment of top burr, exit burr, and entrance burr

(b) Judgment of exit side burr, and entrance side burr
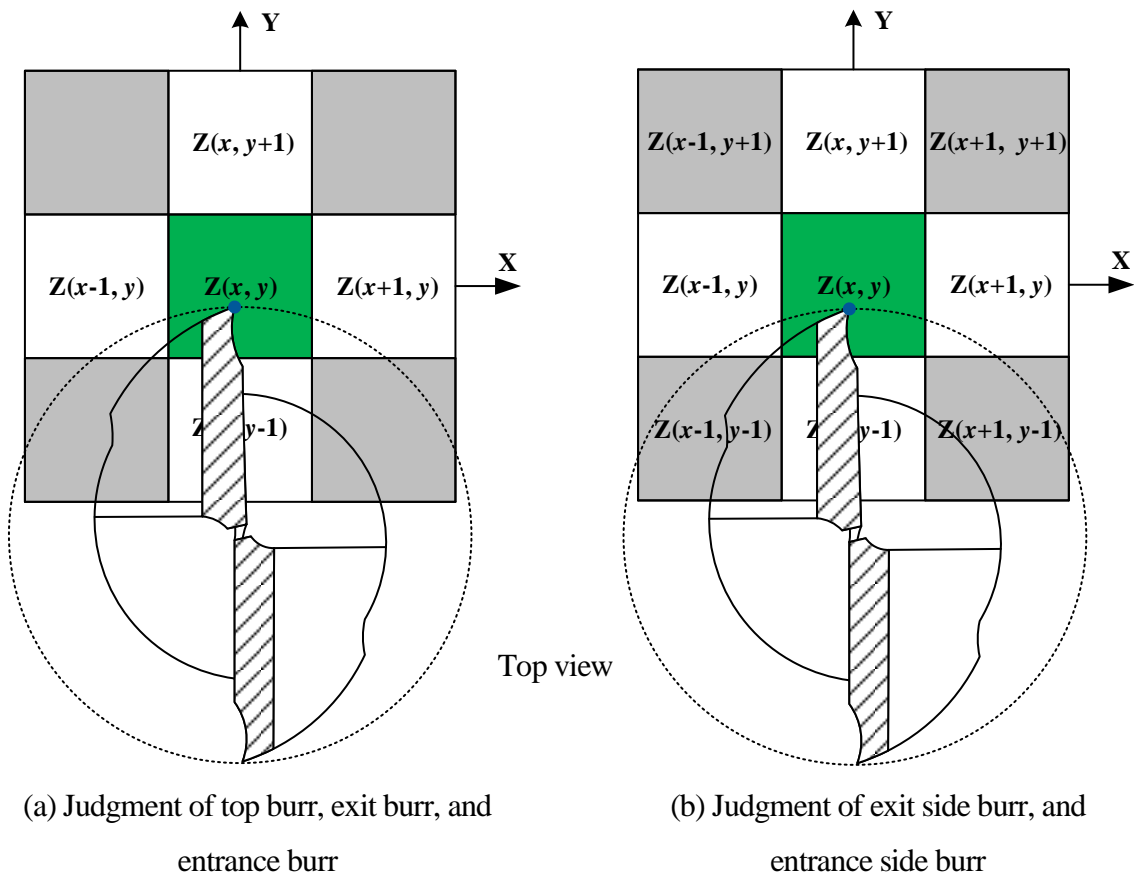
Fig. 4.14 Judgment of burr type using Z-map height of grid point coordinate and Z-map height of interference point Ip.

In Figure 4.14 (a), the cutting tool interferes with the workpiece at point I_p and has Z-map height $Z(x, y)$. The grid points coordinates around the interference point have Z-map heights of $Z(x+1, y)$, $Z(x-1, y)$, $Z(x, y+1)$, and $Z(x, y-1)$.

If:

$Z(x, y) < Z(x+1, y)$:   a top burr forms at coordinate $Z(x+1, y)$ in the +X-axis direction

$Z(x, y) < Z(x-1, y)$:   a top burr forms at coordinate $Z(x-1, y)$ in the –X-axis direction

$Z(x, y) < Z(x, y+1)$:   a top burr forms at coordinate $Z(x, y+1)$ in the +Y-axis direction

$Z(x, y) < Z(x, y-1)$:   a top burr forms at coordinate $Z(x, y-1)$ in the –Y-axis direction

The rollover burr model and oblique cutting are applied for a top burr in both up milling and down milling. Thus, NC simulator uses the following equations for calculating the burr size.

$$\phi = (\sin^{-1}(2 \times (\sigma_y / \sigma_u) \times \sin(45 + \alpha/2) \times \cos(45 - \alpha/2) - \sin\alpha) + \alpha)/2 \qquad (2.6)$$

$$RB_{th} = w \times \tan\beta_o \qquad (2.11)$$

$$RB_h = (t_o + w \times \tan\beta_o) \times \sin(\theta_1 + \theta_2) \times \sin\theta_{ex} \qquad (2.12)$$

$$w_{oblique} = \dfrac{\dfrac{F_f}{\cos(\lambda - \alpha_c)\cos(\phi_c - \alpha_c)}\left[\cos\alpha_c \cos(\phi_c + \lambda - \alpha_c)\cos\kappa + \sin\phi_c \sin\lambda \cos\chi\right]}{\left(\dfrac{k_0}{2}\cos^2\beta_0 + \dfrac{\sigma_y}{4}\tan\beta_0\right)d_r} \qquad (2.14)$$

$$\dfrac{d}{d\beta_0}\left\{\dfrac{\sin\beta_0(\cot\phi + 0.5\cot\beta_0)}{(\cos\beta_0 - \sin\beta_0 \cot\theta_{ex})}\left[2 + 3\cot\beta_0 - 3\cot(\phi + \beta_0)\right]\right\} = 0 \qquad (2.15)$$

$$\theta_1 = \tan^{-1}(x_o / (t_o + w \times \tan\beta_o)) \qquad (2.16)$$

$$\theta_2 = \cos^{-1}((w \times \tan\beta_o \times \sin\theta_1) / x_o) \qquad (2.17)$$

$$\phi_c = \tan^{-1}(\tan\phi \times \cos i) \qquad (2.18)$$

4.4.3 Identification of exit burrs and applied formula

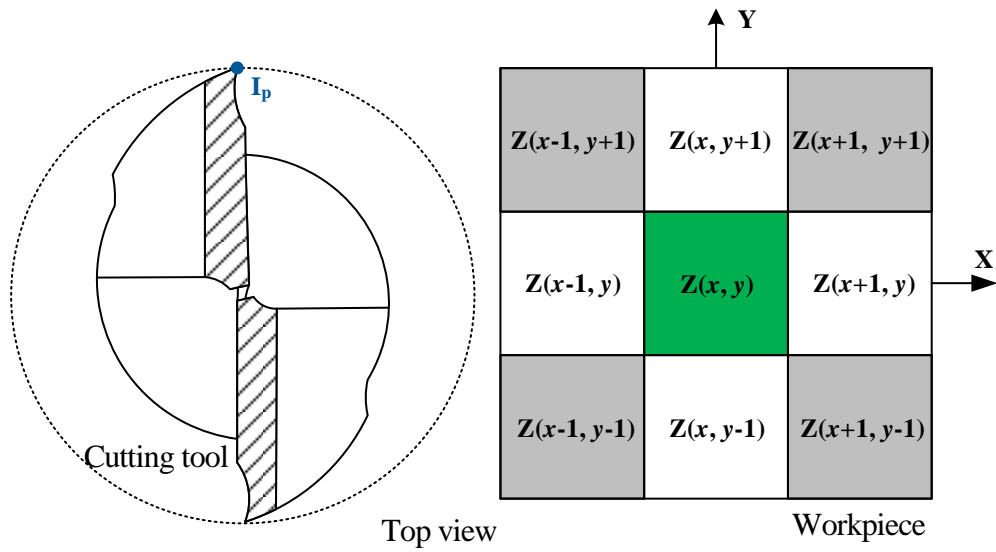To identify the exit burrs, NC simulator will compare the Z-map height at grid point coordinate Z ($\pm x$, $\pm y$) to the Z-map height at interference point Ip like the top burr case, as shown in Fig. 4.14 (a); however, the condition is different.

If:

Z (x, y) > Z (x+1, y):   an exit burr forms at coordinate Z (x, y) in the +X-axis direction

Z (x, y) > Z (x-1, y):   an exit burr forms at coordinate Z (x, y) in the –X-axis direction

Z (x, y) > Z (x, y+1):   an exit burr forms at coordinate Z (x, y) in the +Y-axis direction

Z (x, y) > Z (x, y-1):   an exit burr forms at coordinate Z (x, y) in the –Y-axis direction

The rollover burr model modified with a large axial depth of cut and orthogonal cutting are applied for an exit in burr both up milling and down milling. Thus, NC simulator uses the following equations to calculate the burr size.

$$RB_{th} = w \times \tan\beta_0 \tag{3.3}$$

$$RB_h = w \times \tan\phi \,/\, \tan\beta_0 \tag{3.4}$$

$$\varepsilon_a = [(w + RB_h) \cos\phi - w] \,/\, w \tag{3.5}$$

$$\phi = (\sin^{-1}(2 \times (\sigma_y/\sigma_u) \times \sin(45 + \alpha/2) \times \cos(45 - \alpha/2) - \sin\alpha) + \alpha)/2 \tag{2.6}$$

$$w_{orthogonal} = \dfrac{\dfrac{F_f}{\cos(\lambda - \alpha)\cos(\phi - \alpha)}\left[\cos\alpha\cos(\phi + \lambda - \alpha) + \sin\phi\sin\lambda\right]}{\left(\dfrac{k_0}{2}\cos^2\beta_0 + \dfrac{\sigma_y}{4}\tan\beta_0\right)d_r} \tag{2.13}$$

$$\frac{d}{d\beta_0}\left\{\frac{\sin\beta_0(\cot\phi + 0.5\cot\beta_0)}{(\cos\beta_0 - \sin\beta_0\cot\theta_{ex})}[2 + 3\cot\beta_0 - 3\cot(\phi + \beta_0)]\right\} = 0 \tag{2.15}$$

4.4.4 Identification of exit side burrs and applied formula

To identify the exit side burrs, NC simulator will compare the Z-map height at grid point coordinate $Z(x\pm1, y\pm1)$ with the Z-map height at interference point Ip like in the exit burr case, as shown in Fig. 4.14 (b); however, an additional condition is needed.

If:

$Z(x, y) > Z(x+1, y)$

&&   an exit burr forms at coordinate $Z(x+1, y+1)$ in the +X-axis direction

$Z(x, y) < Z(x, y+1)$

If:

$Z(x, y) > Z(x-1, y)$

&&   an exit burr forms at coordinate $Z(x-1, y-1)$ in the –X-axis direction

$Z(x, y) < Z(x, y-1)$

If:

$Z(x, y) > Z(x, y+1)$

&&   an exit burr forms at coordinate $Z(x-1, y+1)$ in the +Y-axis direction

$Z(x, y) < Z(x-1, y)$

If:

$Z(x, y) > Z(x, y-1)$

&&   an exit burr forms at coordinate $Z(x+1, y-1)$ in the –Y-axis direction

$Z(x, y) < Z(x+1, y)$

The rollover burr model and oblique cutting are applied for an exit burr in both up milling and down milling. Thus, NC simulator uses the following equations to calculate the burr size.

$$\phi = (\sin^{-1}(2 \times (\sigma_y / \sigma_u) \times \sin (45 + \alpha/2) \times \cos (45 - \alpha/2) - \sin\alpha) + \alpha)/2 \qquad (2.6)$$

$$RB_{th} = w \times \tan\beta_o \qquad (2.11)$$

$$RB_h = (t_o + w \times \tan\beta_o) \times \sin (\theta_1 + \theta_2) \times \sin \theta_{ex} \qquad (2.12)$$

$$w_{oblique} = \frac{\dfrac{F_f}{\cos(\lambda - \alpha_c)\cos(\phi_c - \alpha_c)}\left[\cos \alpha_c \cos(\phi_c + \lambda - \alpha_c)\cos \kappa + \sin \phi_c \sin \lambda \cos \chi\right]}{\left(\dfrac{k_0}{2}\cos^2 \beta_0 + \dfrac{\sigma_y}{4}\tan \beta_0\right)d_r} \qquad (2.14)$$

$$\frac{d}{d\beta_0}\left\{\frac{\sin \beta_0(\cot \phi + 0.5\cot \beta_0)}{(\cos \beta_0 - \sin \beta_0 \cot \theta_{ex})}[2 + 3\cot \beta_0 - 3\cot(\phi + \beta_0)]\right\} = 0 \qquad (2.15)$$

$$\theta_1 = \tan^{-1}(x_o / (t_o + w \times \tan\beta_o)) \qquad (2.16)$$

$$\theta_2 = \cos^{-1}((w \times \tan\beta_o \times \sin\theta_1) / x_o) \qquad (2.17)$$

$$\phi_c = \tan^{-1}(\tan\phi \times \cos i) \qquad (2.18)$$

4.4.5 Identification of entrance burrs and applies formula

To identify the entrance burrs, NC simulator will compare the Z-map height at grid point coordinate Z ($\pm x$, $\pm y$) with the Z-map height at interference point Ip, as in the case of exit burrs, as shown in Fig. 4.14 (a); however, the condition is different.

If:

Z (x, y) > Z (x-1, y):   an entrance burr forms at coordinate Z (x, y) in the +X-axis direction

Z (x, y) > Z (x+1, y):   an entrance burr forms at coordinate Z (x, y) in the –X-axis direction

Z (x, y) > Z (x, y-1):   an entrance burr forms at coordinate Z (x, y) in the +Y-axis direction

Z (x, y) > Z (x, y+1):   an entrance burr forms at coordinate Z (x, y) in the –Y-axis direction

The Poisson burr model and orthogonal cutting are applied for the entrance burr in both up milling and down milling. Thus, NC simulator uses the following equations for calculating burr size.

$$PB_{th} = R_e \left(\exp\left(-3\phi_a \right) \sqrt{\cos\phi_a} - 1 \right) \tag{2.3}$$

$$PB_l = \frac{d_a (1+\upsilon)\sigma_p \left(\exp\left(-3\phi_a \right) \right)}{\sqrt{3}E} \left[\frac{-\sin\phi}{2\left(\sqrt{3}\cos\phi + \sin\phi \right)} \right] \tag{2.4}$$

$$\phi_a = -\sin^{-1}\left(\frac{\sqrt{3}P_0}{2\sigma_p} \right) + \frac{\pi}{6} \tag{2.5}$$

$$\phi = (\sin^{-1}(2 \times (\sigma_y / \sigma_u) \times \sin(45 + \alpha/2) \times \cos(45 - \alpha/2) - \sin\alpha) + \alpha)/2 \tag{2.6}$$

$$P_o = \frac{F_c \times \cos\alpha - F_f \times \sin\alpha}{d_a \times a_o} \tag{2.7}$$

4.4.6 Identification of entrance side burrs and applied formula

To identify the entrance side burrs, NC simulator compares the Z-map height at grid point coordinate Z $(x\pm1, y\pm1)$ with the Z-map height at interference point Ip, as in the case of entrance burrs, as shown in Fig. 4.14 (b); however, an additional condition is needed.

If:

Z $(x, y) >$ Z $(x$-1, $y)$
&&
Z $(x, y) <$ Z $(x, y+1)$ | an entrance side burr forms at coordinate Z $(x$-1, $y+1)$ in the +X-axis direction

Z $(x, y) >$ Z $(x+1, y)$
&&
Z $(x, y) <$ Z $(x, y$-1) | an entrance side burr forms at coordinate Z $(x+1, y$-1) in the −X-axis direction

Z $(x, y) >$ Z $(x, y$-1)
&&
Z $(x, y) <$ Z $(x$-1, $y)$ | an entrance side burr forms at coordinate Z $(x$-1, y-1) in the +Y-axis direction

Z $(x, y) >$ Z $(x, y+1)$
&&
Z $(x, y) <$ Z $(x+1, y)$ | an entrance side burr forms at coordinate Z $(x+1, y+1)$ in the −Y-axis direction

The Poisson burr model and orthogonal cutting are applied for an entrance side burr in both up milling and down milling. Thus, NC simulator uses the following equations to calculate burr size.

$$PB_{th} = R_e\left(\exp\left(-3\phi_a\right)\sqrt{\cos\phi_a} - 1\right) \tag{2.3}$$

$$PB_l = \frac{d_a(1+\upsilon)\sigma_p\left(\exp\left(-3\phi_a\right)\right)}{\sqrt{3}E}\left[\frac{-\sin\phi}{2\left(\sqrt{3}\cos\phi + \sin\phi\right)}\right] \tag{2.4}$$

$$\phi_a = -\sin^{-1}\left(\frac{\sqrt{3}P_0}{2\sigma_p}\right) + \frac{\pi}{6} \tag{2.5}$$

$$\phi = (\sin^{-1}(2 \times (\sigma_y / \sigma_u) \times \sin (45 + \alpha/2) \times \cos (45 - \alpha/2) - \sin\alpha) + \alpha)/2 \qquad (2.6)$$

$$P_o = \frac{F_c \times \cos\alpha - F_f \times \sin\alpha}{d_a \times a_o} \qquad (2.7)$$

4.4.7 Burr direction

The direction of the burr formation is identified by tool exit-angle φ_{exit}, as shown in Fig. 4.15. Two cases are considered: one with a radial depth of cut that is larger than the tool radius and the other with a radial depth of cut that is smaller than the tool radius.

$$\begin{cases} \varphi_{exit} = \dfrac{\pi}{2} + \sin\left(\dfrac{R - d_r}{R}\right) & if\, d_r > R \\ \varphi_{exit} = \sin\left(\dfrac{R - d_r}{R}\right) & if\, d_r < R \end{cases} \qquad (4.35)$$
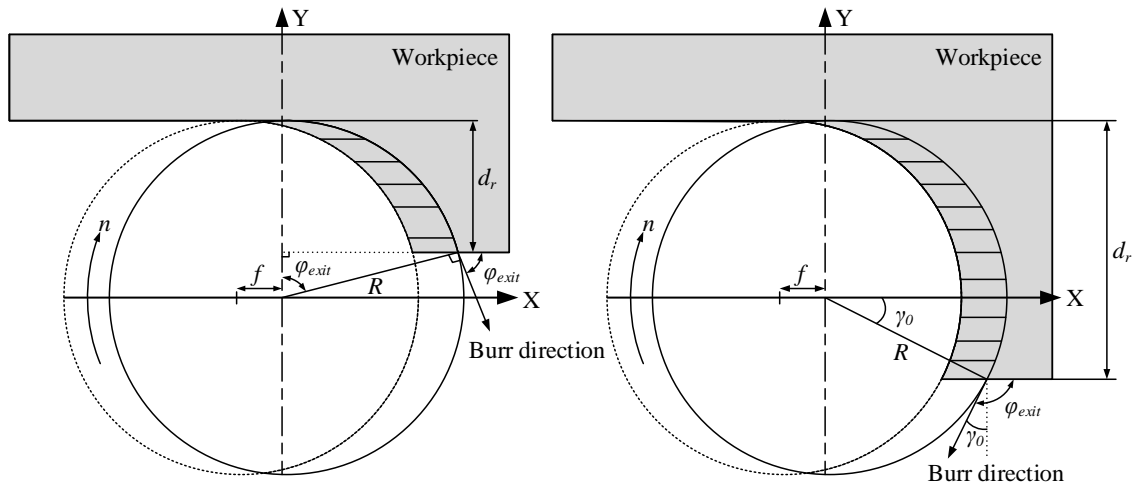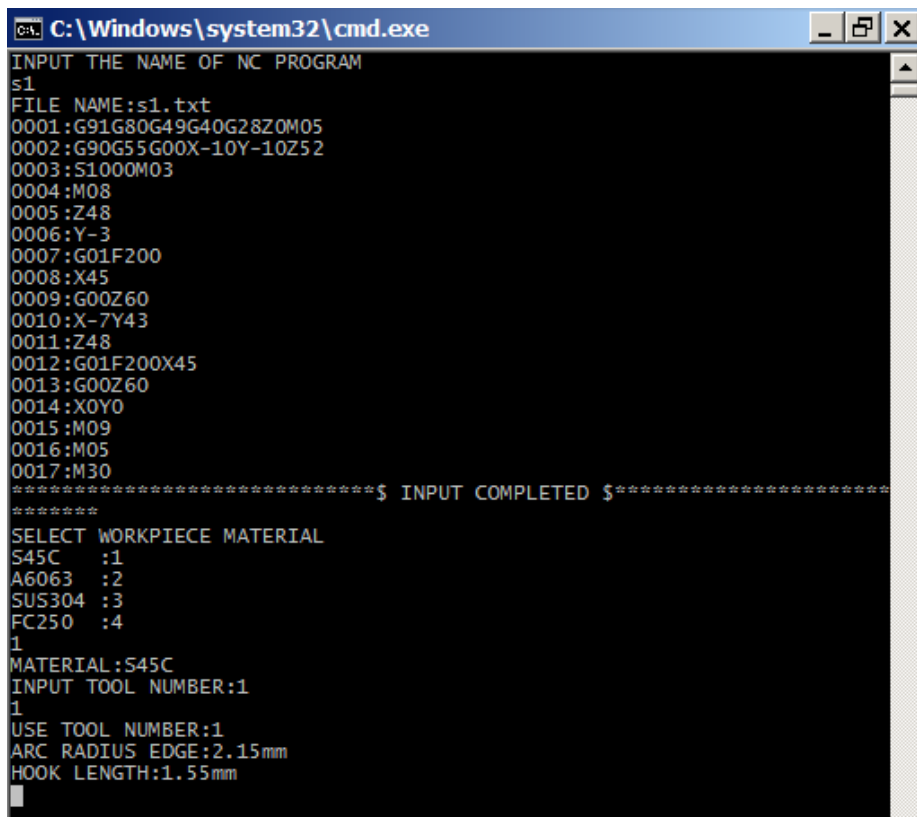
Fig. 4.15 Burr direction condition.

4.5 Execution of burr prediction system

4.5.1 Method for operation of burr prediction system

In order to execute the program simulation, G-code in a text file (.txt) is prepared. As an example, a text file named s1.txt is called for program execution as shown the Fig. 4.16. In this text file, the user needs to write the NC program in G-code. To begin running the program, the file s1.txt is simply called. Then, the user can choose the workpiece material types. In this study, four types of workpieces were used, S45C, A6063, SUS304, and FC250.


```
C:\Windows\system32\cmd.exe                          _ | 日 | ×
INPUT THE NAME OF NC PROGRAM
s1
FILE NAME:s1.txt
0001:G91G80G49G40G28Z0M05
0002:G90G55G00X-10Y-10Z52
0003:S1000M03
0004:M08
0005:Z48
0006:Y-3
0007:G01F200
0008:X45
0009:G00Z60
0010:X-7Y43
0011:Z48
0012:G01F200X45
0013:G00Z60
0014:X0Y0
0015:M09
0016:M05
0017:M30
***************************$ INPUT COMPLETED $**********************
*******
SELECT WORKPIECE MATERIAL
S45C    :1
A6063   :2
SUS304  :3
FC250   :4
1
MATERIAL:S45C
INPUT TOOL NUMBER:1
1
USE TOOL NUMBER:1
ARC RADIUS EDGE:2.15mm
HOOK LENGTH:1.55mm
```

Fig. 4.16 Input data screen for system execution.

The system will start the simulation when the user clicks the mouse anywhere on the window console screen, as shown in Fig. 4.17.
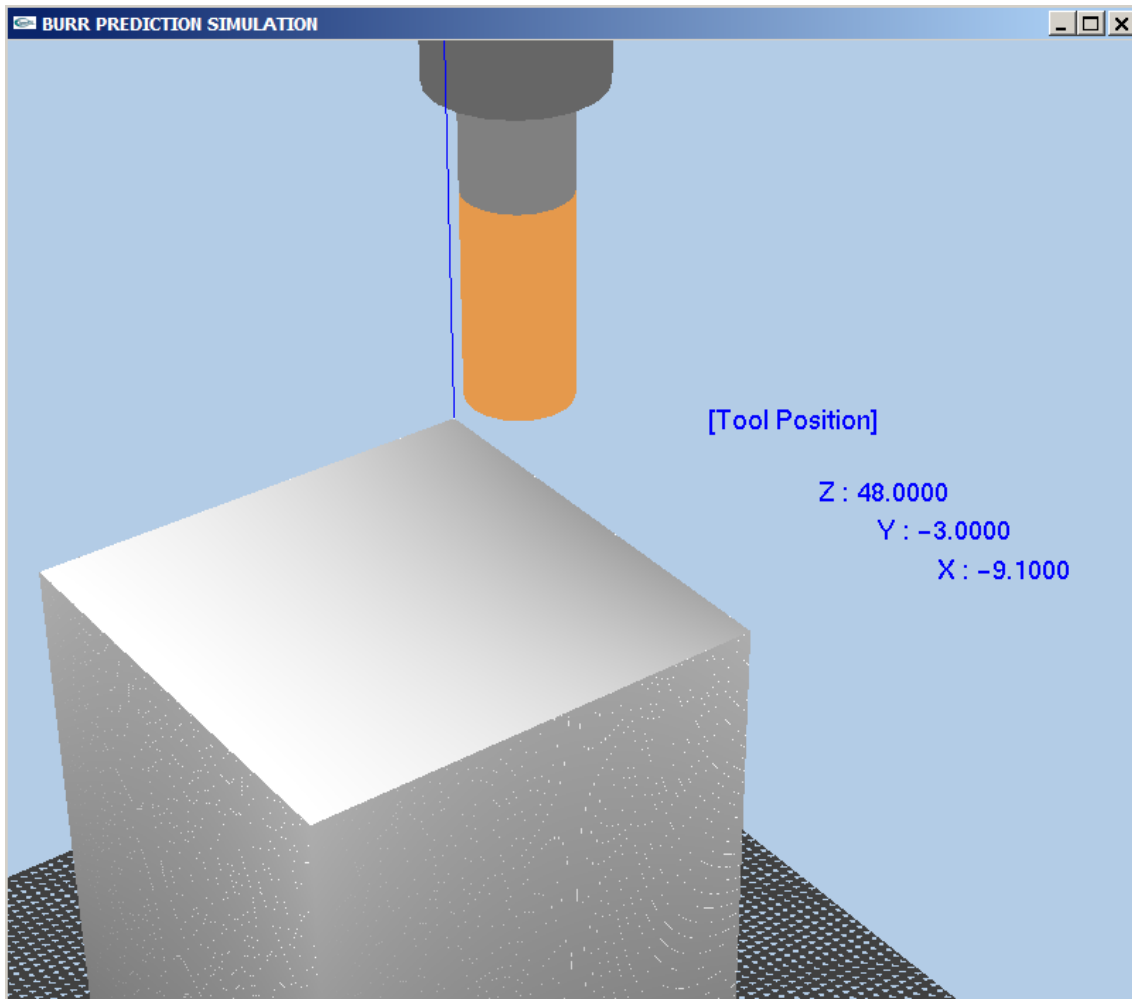
Fig. 4.17 Console window screen for system execution.

After starting the simulation, the cutting tool moves based on the NC code input from the text file. The tool path and burr location are displayed in the console window on the workpiece edge. The blue color represents the Poisson burr type, while the red color represents the rollover burr type, as shown in Fig. 4.18. The system can also test complex shapes, as shown in Fig. 4.19. The burr size result can be shown during the simulation or saved in a .csv file after completing the execution. The user needs to choose burr the height or burr thickness to save, and four files are saved, including those for the burr size in the X-axis direction (entrance burr or exit burr), burr size in the Y-axis direction (entrance burr or exit burr), burr size in the Z-axis direction (top burr), and burr size in the vertical direction (entrance side burr or exit side burr).
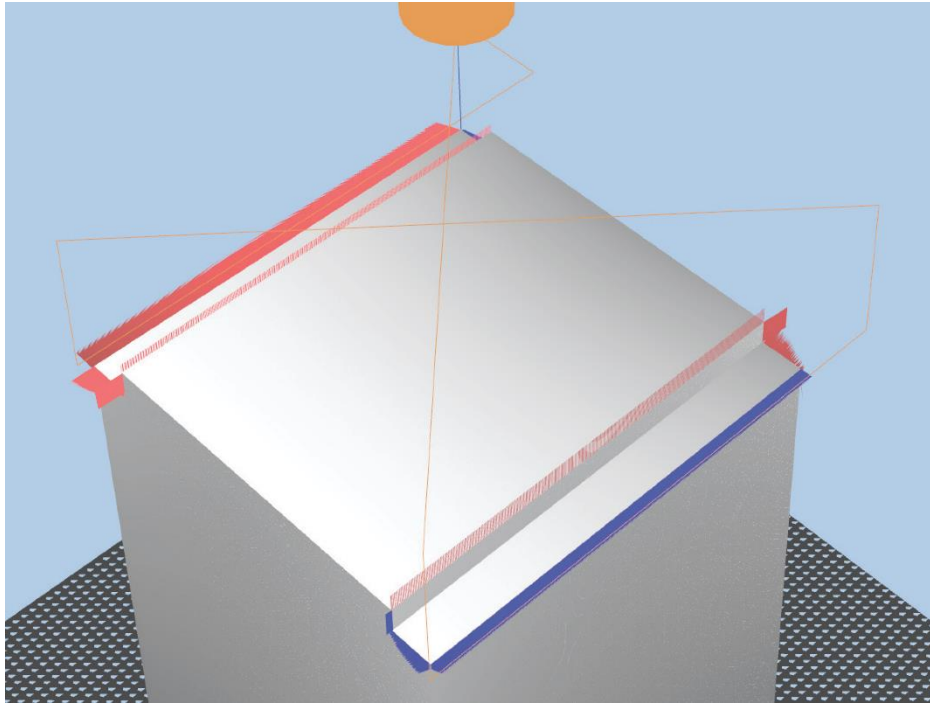
Fig. 4.18 Console window screen for system execution to predict burr location and size.
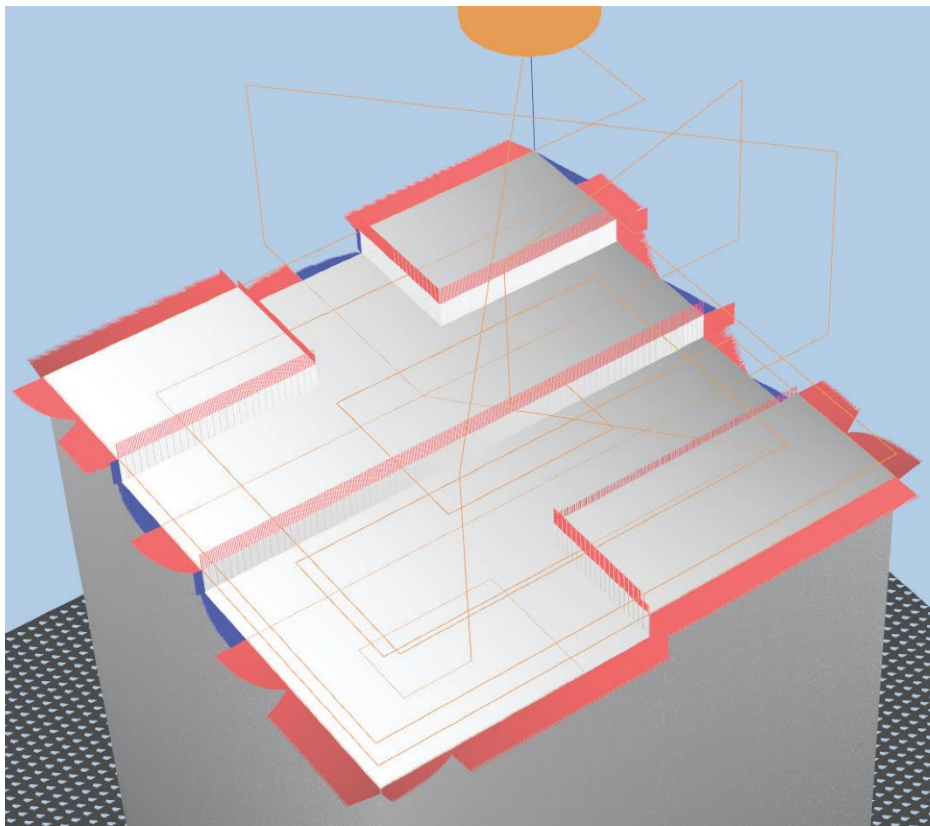
Fig. 4.19 Console window screen for system execution with complex shape.

4.6 Tool path planning for burr minimization

4.6.1 Basic tool path planning

A good way to minimize burrs is to avoid tool exit. According to this theory, if the tool cutter exits the workpiece edge while machining, large burrs result, but these do not occur when the cutter enters the workpiece edge. An exit here refers specifically to the tool cutting edge moving out of the workpiece at an edge while removing the material.

In this study, tool path planning for down milling and up milling were studied using the window framing scheme method, as shown in Fig. 4.20. In window framing or contour parallel milling the cutting tool constantly engages the workpiece. It is a secure and efficient process. Another tip to add to the window framing scheme method in this study is the roll-ending technique at the corner, which provides a gentle tool engagement. The roll-ending technique is also used when the tool first engages the workpiece. It is a golden rule in the milling process to make a thick chip at the entrance and a thin chip at the exit, because this results in less stress on the cutting tool, ensures a stable process, and saves machine time and money. The most important point is that no tool exit is produced by the window framing scheme method.

(a) Top view: Tool path A   (b) Top view: Tool path A
(Cutting tool engaged from outside)   (Cutting tool engaged from inside)
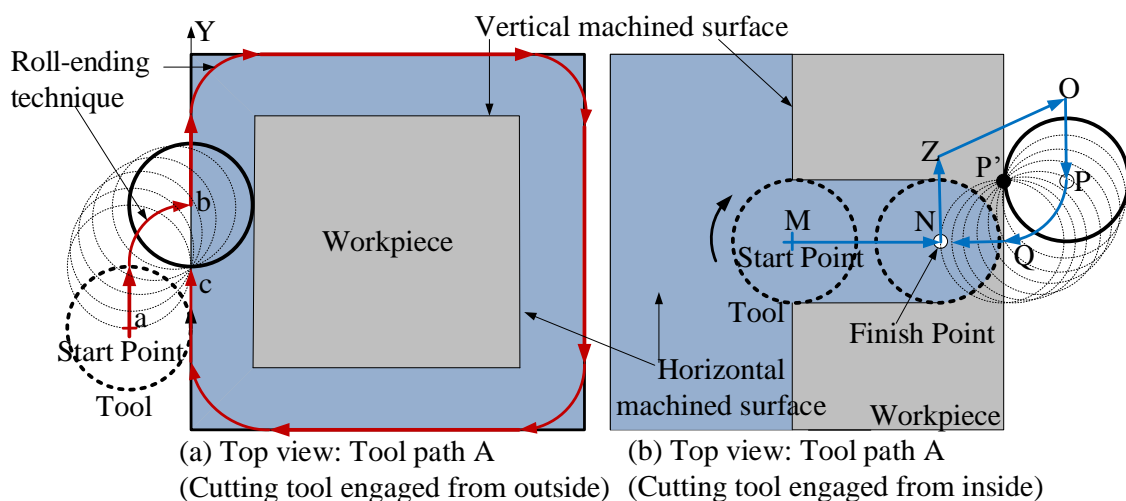
Fig. 4.20 Tool path planning in down milling adapted window frame method[26].

In addition to window framing, three tool path types are considered in this paper for up milling and down milling: tool path A, where the width of cut d_r = tool radius R; tool path B, where the width of cut d_r < tool radius R; tool path C, where the width of cut d_r > tool radius R, as shown in Fig. 4.23. Figure 4.20 (a) & (b) shows the tool path planning in down milling for tool path type A (width of cut = tool radius). In a case where the cutting tool engaged the workpiece from outside the workpiece edge, we adopted the tool path planning as shown in Fig.4.20 (a). Point b is defined by the center of the cutting tool moving from point a in a clockwise motion (G02) to center point c (bc = tool radius). Using this tool motion, only a Poisson burr was formed. This technique prevents rollover burrs from forming on the workpiece edges, as shown in Fig. 4.21.

Fig. 4.21 Tool path planning modified to avoid exit burr.

The red line in Fig. 4.20 (a) is the tool path planning for the workpiece. Assume that the cutting tool starts to engage at point a. After the tool approaches point b (bc = tool radius), it moves along the workpiece edge in a clockwise direction until point c. The blue line in Fig. 4.20 (b) is the tool path planning of the cutting tool before leaving the workpiece edge. Assume t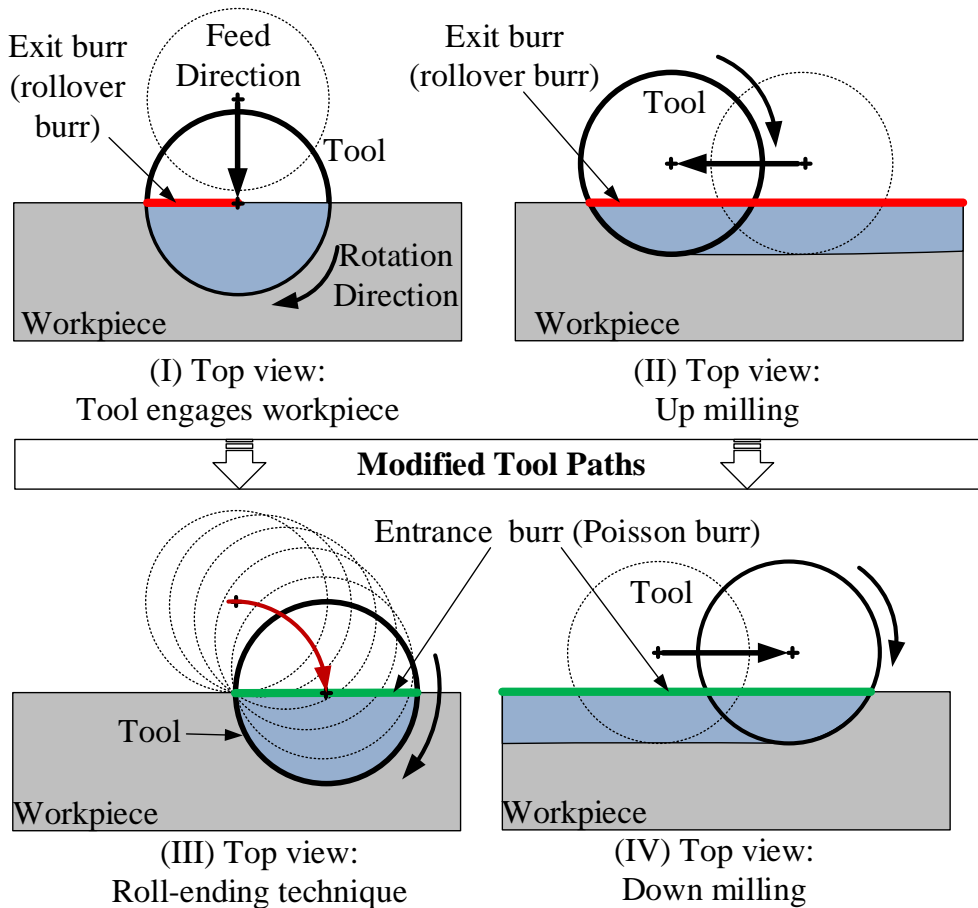hat the cutting tool starts at point M. After the cutting tool approaches point N (NQ = cutting tool radius + 1 mm), it moves up to point Z in the Z-direction and continues to point O. It then moves down to point P (PP' = cutting tool radius) and starts to engage the workpiece again from point P to point Q. The Z levels of points N, Q, and P are the same as shown in Fig. 4.22.

The tool path method in Fig. 4.20 (a) and (b) can be adapted for tool paths A and B but cannot be applied for tool path C, as shown in Fig. 4.23. Because the tool cutting edge still moves out of the workpiece at an edge while removing the material, the method used for tool paths A and B cannot be adapted for tool path C. The tool path method for tool path C has some modification as shown in Fig. 4.24. Assume that the cutting tool starts at point H. At point I, the cutting tool has changed direction toward point J and rolls counter clockwise to point K outside the workpiece edge. The tool starts to approach the workpiece again from point K to L.

(a) Side view   (b) Top view
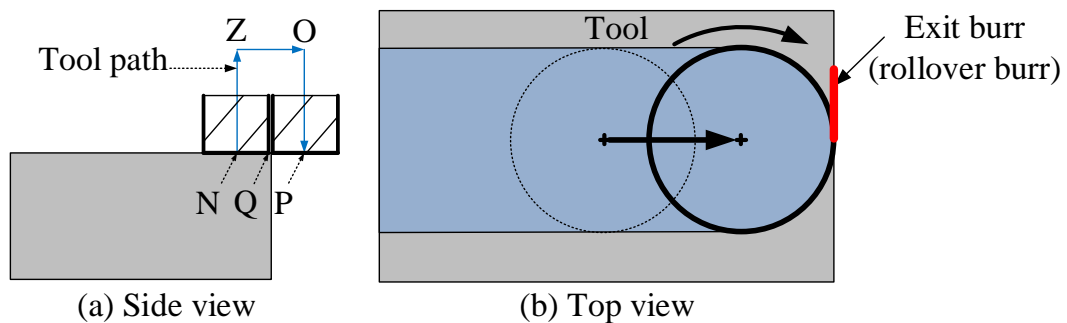
Fig. 4.22 Exit burr formed in case of cutting tool engaged from inside.
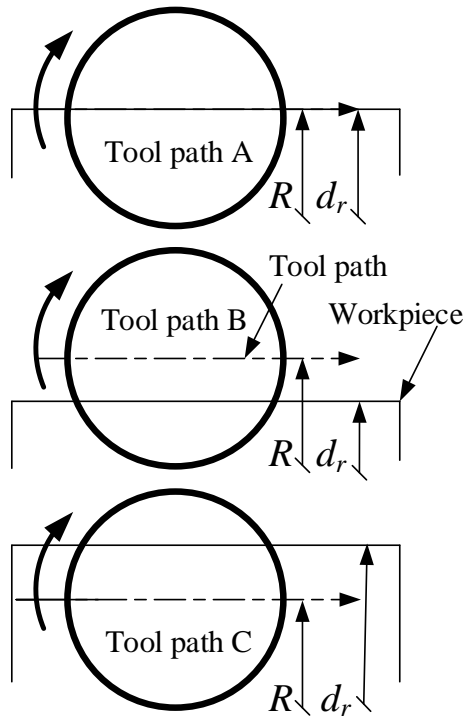
Fig. 4.23 Three types of tool paths in down milling[26].
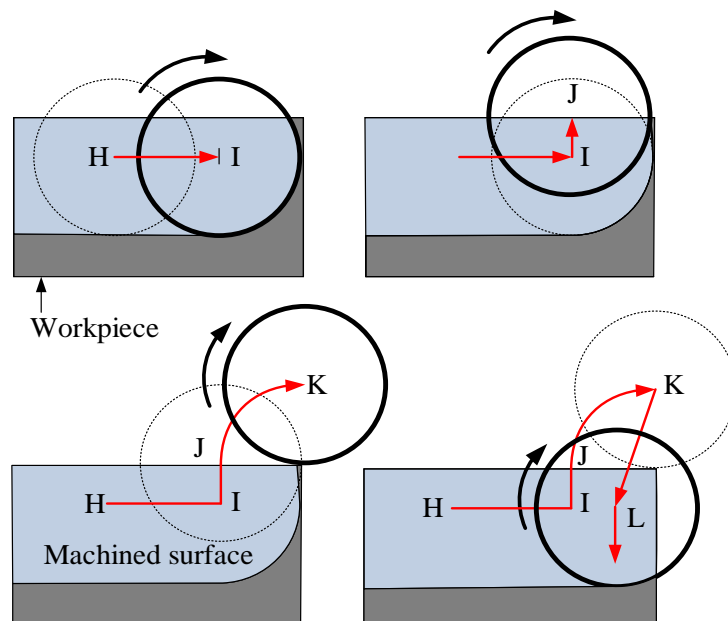
Fig. 4.24 Tool path method for tool path C[26].

4.6.2 Other tool path planning cases

Other tool path planning cases also consider burr minimization, such as the tool path plan in a case where workpiece width W_w is smaller than the diameter of the cutting tool, D, and a case where the workpiece has a round shape. To minimize the burr size in the first case, the diameter of the cutting tool needs equal to or larger than the workpiece width. Thus, the tool exit angle $\varphi_{exit} < 90^\circ$, and only a small burr can form[24], as shown in Fig. 4.25.
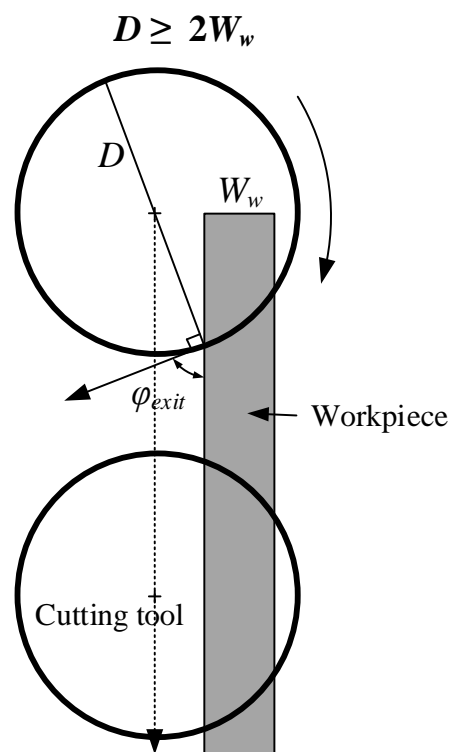
Fig. 4.25 Tool path method when workpiece width is smaller than tool diameter.
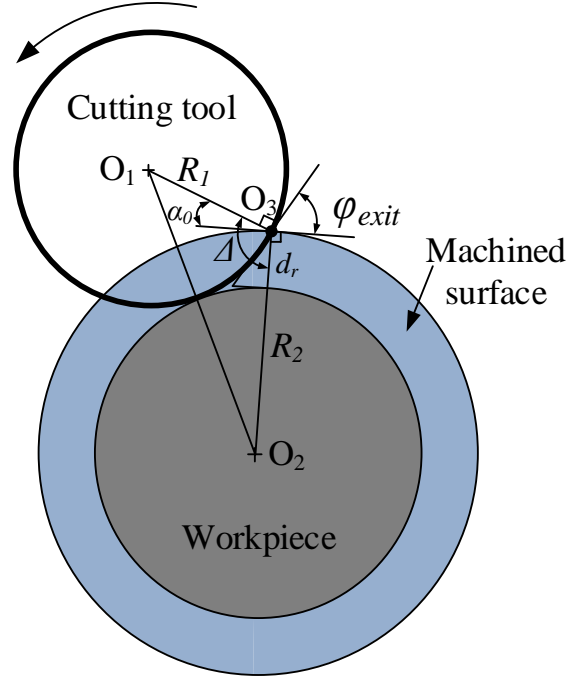
Fig. 4.26 Tool path method when workpiece has round shape.

In a case where the workpiece has a round shape, there is a critical need to define the radial depth of cut in order to reduce the burr size, based on the concept that a small burr forms only when the tool exit angle $\varphi_{exit} < 90°$ [24]. Thus, the modification of the tool path can be illustrated as shown in Fig. 4.26, and the following equation to define the radial depth of cut can be obtained.

In triangle $\Delta O_1 O_2 O_3$, we have

$$\Delta = \arccos\left(\frac{R_1^2 + R_2^2 - (R_1 + R_2 - d_r)^2}{2R_1 R_2}\right) \tag{4.36}$$

$$\alpha_0 = \Delta - \frac{\pi}{2} \tag{4.37}$$

$$\varphi_{exit} = \frac{\pi}{2} - \alpha_0 = \pi - \Delta \tag{4.38}$$

$$\varphi_{exit} < 90° \rightarrow \pi - \arccos\left(\frac{R_1^2 + R_2^2 - (R_1 + R_2 - d_r)^2}{2R_1 R_2}\right) < \frac{\pi}{2} \tag{4.39}$$

$$\frac{R_1^2 + R_2^2 - (R_1 + R_2 - d_r)^2}{2R_1 R_2} > 0 \tag{4.40}$$

$$d_r^2 - 2(R_1 + R_2)d_r + (R_1 + R_2)^2 + R_1^2 + R_2^2 > 0 \tag{4.41}$$

4.7 Burr prediction based on flank wear during end milling

A new model to understand the burr formation and tool wear behaviors of solid carbide tools during dry end milling is proposed. This model shows that the burr size varies based on the relationship between the tool flank wear CD and cutting edge radius wear R_w as shown in in Fig. 4.27. After machining for a period, the flank wears starts to form at point C to point D. The center of the sharp tool nose O moves to point O_w. The shear angle ϕ_w is larger than shear angle ϕ of a sharp tool.

The total cutting force in end milling is the result of the forces required for chip formation in the shear zone and the rubbing forces on the wear land. In order to calculate the cutting force in this case, the cutting edge radius wear needs to be calculated first. Thus, the following basic assumptions are made.

- The height of stagnation point h_s does not change after the cutting tool got dull, as shown in Fig. 4.27.
- The flank wear is considered, while other factors are not taken into account, including other forms of tool wear such as crater wear, and other factors such as the machine vibration and rigidity, the temperature change at the tool/workpiece interface, and thermal expansion of the cutting tool and workpiece.

Base on these assumptions and the tool geometry show in Fig. 4.27, the height of stagnation point h_s is

$$h_s = h_w = R_e \ (1\text{-}\cos\theta_s) \tag{4.42}$$

The stagnation or neutral point angle of a dull tool can be found as follows:

$$\cos \theta_w = \frac{\Delta r}{R_w - R_e} = \frac{R_w - h_s - \Delta r}{R_w} \tag{4.43}$$

where R_e is the effective cutting edge radius of a sharp tool, $\Delta_r = CD \times \tan\alpha_{cl}$, CD is the tool flank wear dimension, and α_{cl} is the clearance angle. Equation (4.43) can be written as

$$R^2_w - \left(h_s + 2 \times CD \times \tan\alpha_{cl} + R_e\right)R_w + R_e\left(h_s + 2 \times CD \times \tan\alpha_{cl}\right) = 0 \tag{4.44}$$

The effective rake angle at stagnation or neutral point S and shear angle ϕ_w can be found in Eq. (4.45) and Eq. (4.46), respectively.

$$\alpha_e = \tan^{-1}\left(\frac{R_w - h_s}{R_w}\right) = \tan^{-1}\left(1 - \frac{R_e\left(1 - \cos\theta_s\right)}{R_w}\right) \tag{4.45}$$

$$\phi_w = \frac{1}{2}\sin^{-1}\left[\frac{2\sigma_y}{\sigma_u}\sin\left(45 + \frac{\alpha_e}{2}\right)\cos\left(45 - \frac{\alpha_e}{2}\right) - \sin\alpha_e\right] + \frac{\alpha_e}{2} \tag{4.46}$$

After all of these parameters have been calculated, the cutting forces for this case can be defined and applied to the burr formation model for a burr prediction simulation.
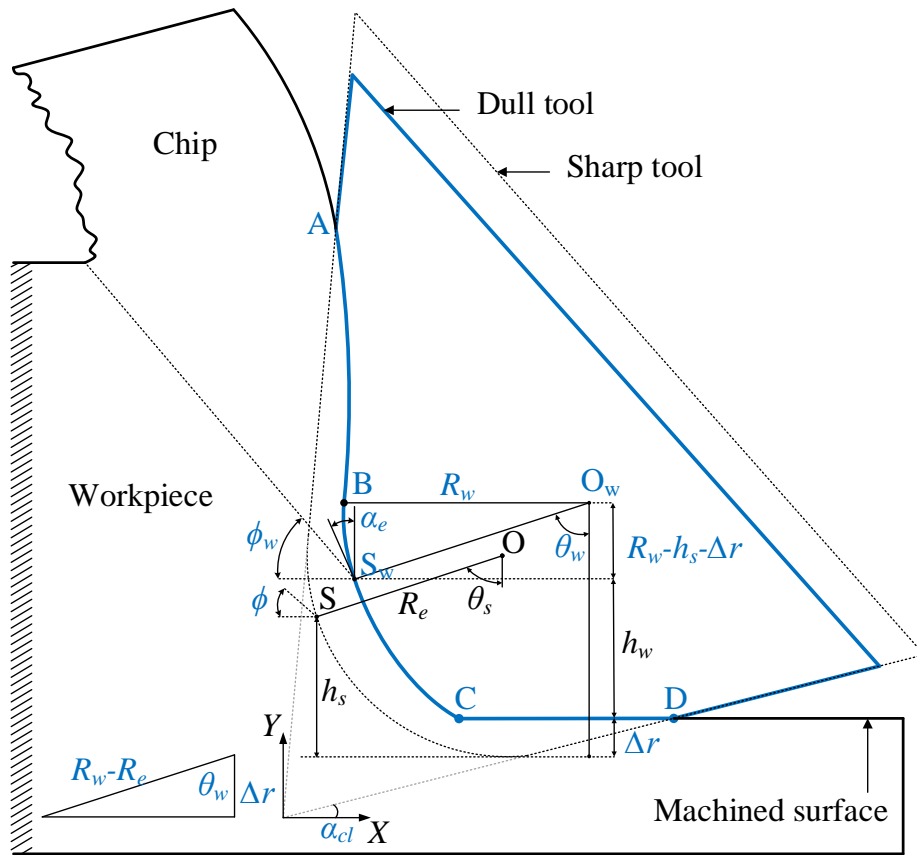
Fig. 4.27 Cutting force model due to flank wear.

4.8 Chapter summary

This chapter described the development of a burr prediction system for the end milling process. The NC program analysis, entrance burr, entrance side burr, exit burr, exit side burr, and top burr for both up milling and down milling have been discussed in detail. The cutting length, radial depth of cut, and axial depth of cut were also illustrated. The cutting force models used in the burr prediction model were also demonstrated. Types of burr identification and burr model applications have been shown. It was shown that the burr prediction process could be executed successfully. The system can also work with complex target shapes. The tool path planning processes for burr minimization were discussed. The system also includes a model of the tool flank wear effect on a burr based on cutting edge radius wear calculation. The system verification of the burr prediction system will be discussed in the next chapter.

CHAPTER 5

5. System Verification

5.1 Simulation of burr formation in end milling

The proposed approach was implemented in object-oriented software under Windows using C++ Builder[13] and the graphical library OpenGL[14]. The system showed the places where burrs occurred in different colors. The red and blue colors represent rollover and Poisson burrs, respectively. The tool path was also displayed in the system, showing the real size of the end mill cutting tool and workpiece. The cutting conditions used in this simulation test are listed in Tables 5.1 to 5.4. Four kinds of workpiece materials were used: steel C:0.45%, AlMg0.5Si, gray cast iron 250, and stainless steel 6. The workpiece materials are listed in Table 5.5.

Table 5.1 Different cutting conditions used in tests on steel C:0.45%.

Test number	d_a [mm]	d_r [mm]	Spindle speed [rpm]	Feed rate [mm/tooth]
1	2.0	2.0	1000	0.1
2	2.0	1.0	1000	0.1
3	2.0	3.0	1000	0.1
4	2.0	4.0	1000	0.1
5	2.0	2.0	1200	0.1
6	2.0	2.0	800	0.1
7	2.0	2.0	1000	0.05
8	2.0	2.0	1000	0.15
9	3.0	2.0	1000	0.1
10	4.0	2.0	1000	0.1

Table 5.2 Different cutting conditions used in tests on AlMg0.5Si.

Test number	d_a [mm]	d_r [mm]	Spindle speed [rpm]	Feed rate [mm/tooth]
1	2.0	1.0	2000	0.1
2	2.0	2.0	2000	0.1
3	2.0	3.0	2000	0.1
4	2.0	4.0	2000	0.1
5	2.0	2.0	1500	0.1
6	2.0	2.0	2500	0.1
7	2.0	2.0	2000	0.15
8	2.0	2.0	2000	0.2
9	3.0	2.0	2000	0.1
10	4.0	2.0	2000	0.1

Table 5.3 Different cutting conditions used in tests on gray cast iron 250.

Test number	d_a [mm]	d_r [mm]	Spindle speed [rpm]	Feed rate [mm/tooth]
1	2.0	2.0	700	0.1
2	2.0	1.0	700	0.1
3	2.0	3.0	700	0.1
4	2.0	4.0	700	0.1
5	2.0	2.0	900	0.1
6	2.0	2.0	500	0.1
7	2.0	2.0	700	0.05
8	2.0	2.0	700	0.15
9	3.0	2.0	700	0.1
10	4.0	2.0	700	0.1

Table 5.4 Different cutting conditions used in tests on Stainless steel 6.

Test number	d_a [mm]	d_r [mm]	Spindle speed [rpm]	Feed rate [mm/tooth]
1	2.0	2.0	400	0.1
2	2.0	1.0	400	0.1
3	2.0	3.0	400	0.1
4	2.0	4.0	400	0.1
5	2.0	2.0	500	0.1
6	2.0	2.0	300	0.1
7	2.0	2.0	400	0.05
8	2.0	2.0	400	0.15
9	3.0	2.0	400	0.1
10	4.0	2.0	400	0.1

Table 5.5 Workpiece material properties[25].

	Ultimate tensile strength σ_u [MPa]	Yield strength σ_y [MPa]	Young's modulus E [GPa]	Poisson's ratio v
Steel C: 0.45%	570	345	206	0.28
AlMg0.5Si	152	90	68.9	0.33
Gray cast iron 250	200	130	206	0.3
Stainless steel 6	520	205	197	0.3

5.2 Experimental verification

5.2.1 Evaluation method for burr generation using fresh cutting tool

This section discusses actual cutting experiments that were conducted to compare the actual burr size with the simulation results. The cutting tool that was used in this experimental test was 2SSD1000S10[12], as shown in Fig. 5.1.

Table 5.6 Cutting tool parameters.

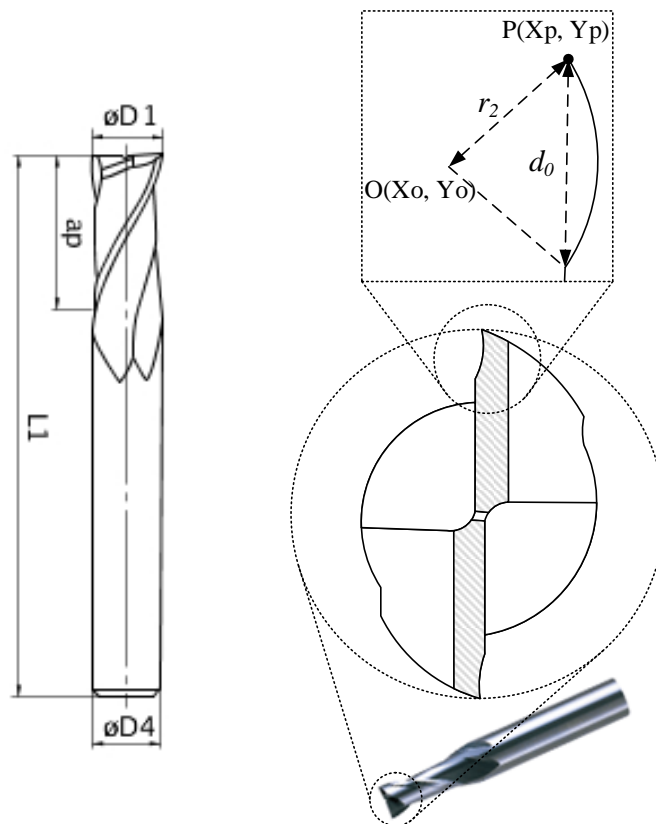|			
Chord length d_0	1.55 mm	ap	20 mm
Tool edge radius r_2	2.15 mm	Number of flute	2 flues
D1	10 mm	L1	75 mm
D4	10 mm		

Fig. 5.1 Cutting tool 2SSD1000S10 and its detailed geometry[12].

Fig. 5.2 Machine center MSA30 Seiki Makino.

In order to obtain highly accurate experimental test result, a Seiki Makino MSA30 machine center was used, as shown in Fig. 5.2. The NC program used in the burr prediction system was used in this machine for the experiment.

The workpiece materials in this study were steel with 0.45% carbon, AlMg0.5Si, gray cast iron 250, and stainless steel 6, in the form of 20×20×30-mm blocks, as shown in Fig. 5.3. The workpiece properties are listed in Table 5.5. Before conducting the experiment, the workpiece surfaces to be machined were prepared to prevent a different tool cutting direction from affecting the burr size. In this evaluation, ten experimental tests and ten simulation tests were conducted for up and down milling. The cutting conditions listed in Table 5.1 to Table 5.4 were set according to the cutting conditions recommended by a cutting tool company[12]. As an example, the axial depth of cut was increased from 2 mm to 4 mm using an increment setting of 1 mm, while the radial depth of cut was increased from 1 mm to 4 mm using the same setting. The spindle speed was increased from 800 rpm to 1200 rpm using an increment setting of 200 rpm. The feed rate was increased from 0.05 mm to 0.15 mm with an increment setting of 0.05 mm/tooth. These parameters were applied to tests 2-10. Test number 1 had the recommended
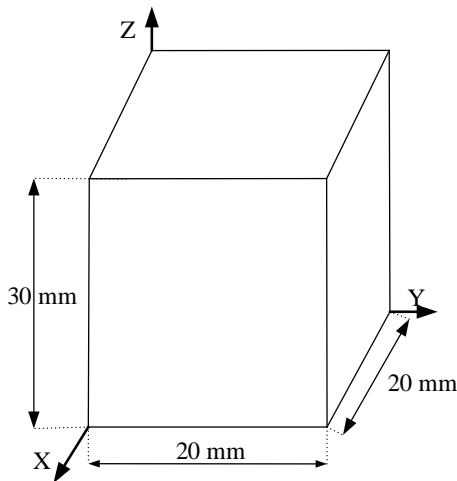
cutting condition, which was used for comparison with tests 2-10. By varying the cutting conditions, we could determine the effect of these parameters on the burr sizes.

(a) S45C Steel block before prepare machine surface.

(b) Steel C: 0.45% after preparing surface for machining.

(c) AlMg0.5Si after preparing surface for machining.

Fig. 5.3 Workpieces for testing.

In this evaluation, ten experimental tests and simulation tests were conducted for up- and down-milling. A digital microscope (KEYENCE: VHX-600) was used to measure the burr size. The burr height and burr thickness were determined by scale measurements using an enlarged 2D image. Images were obtained at angles of 60° from the vertical direction and 90° from the horizontal direction for the burr thickness and burr height, respectively. The cutting fluid was not considered in this study. Pictures for the burrs of steel C: 0.45 % workpiece are shown in Fig. 5.4.
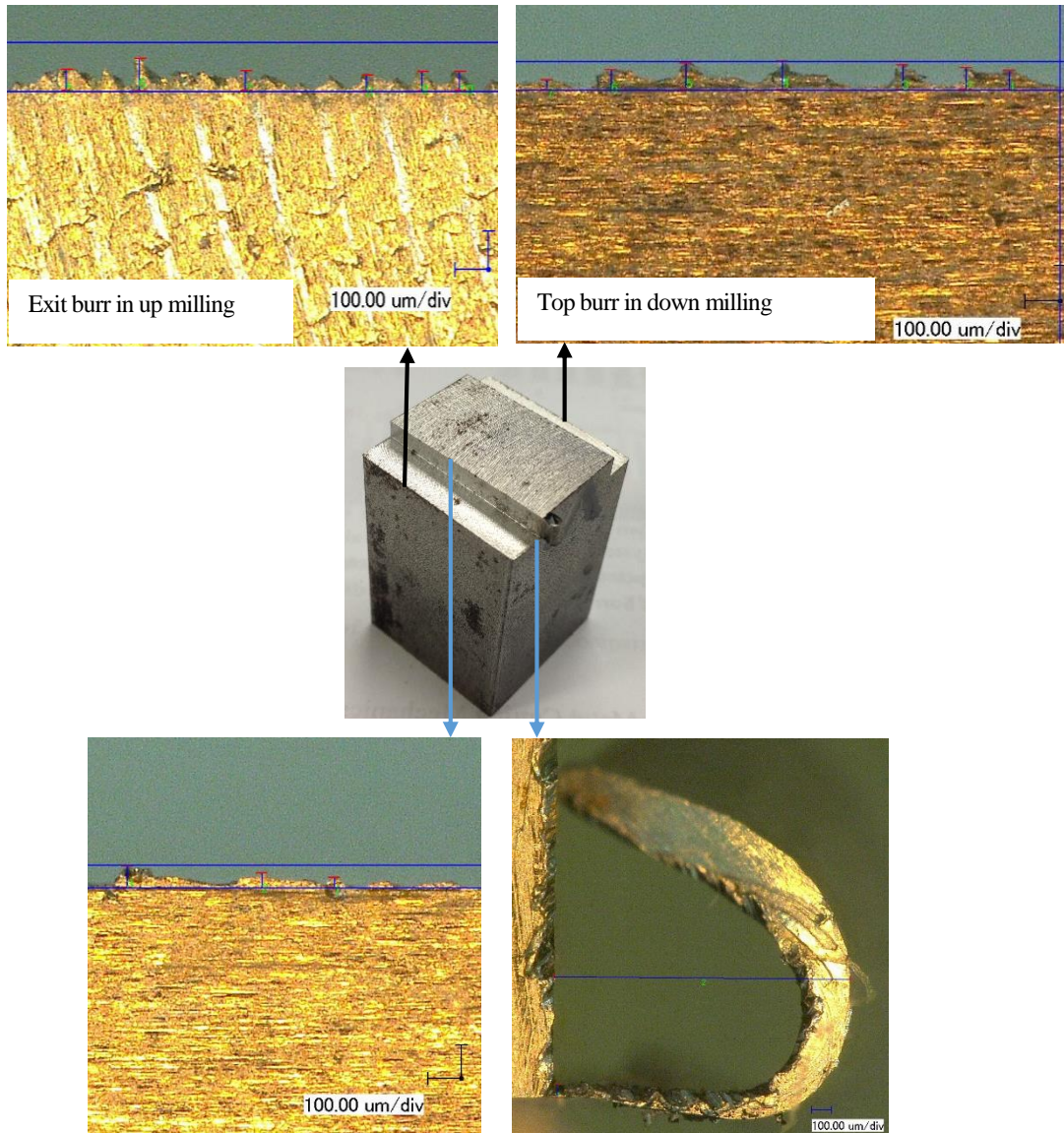
Fig. 5.4 Digital microscope (KEYENCE: VHX-600) was used to measure average exit burr size.

For most of the workpiece materials, the entrance burrs and entrance side burrs in down milling and up milling were found to have very small sizes (the burr height was around 10 μm), as shown in Fig. 5.5 to Fig. 5.8. However, for the entrance burr of the steel C:0.45% workpiece, the burr size seemed to be larger than those for the other materials (the burr height was around 20 μm), as shown in Fig. 5.9 and Fig. 5.10. These burrs are classified as secondary burr that is no much harm to the user because of their small sizes. In some application, those burr because they pose little harm to the user because of their small sizes. In some applications, such burrs are acceptable, without the need for a deburring process, which can be very expensive.
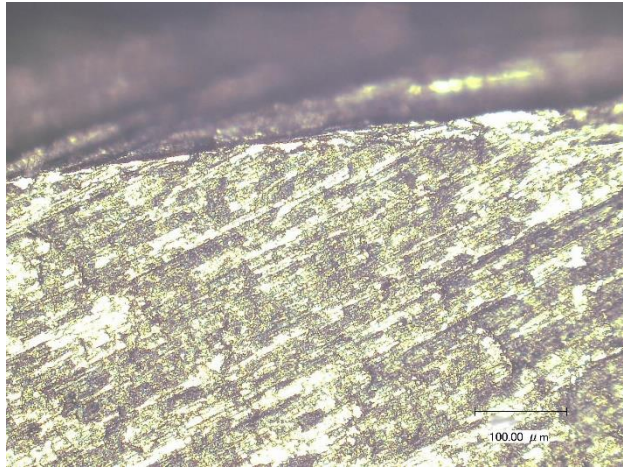
Fig. 5.5 Image of entrance burr in up milling for gray cast iron 250 enlarged by digital
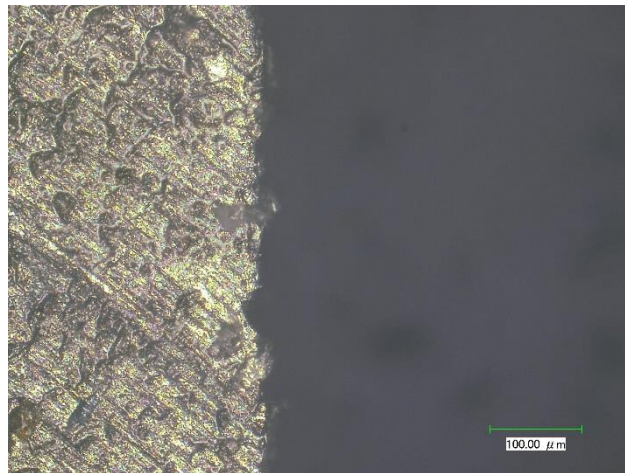microscope.

Fig. 5.6 Image of entrance side burr in up milling for gray cast iron 250 enlarged by digital
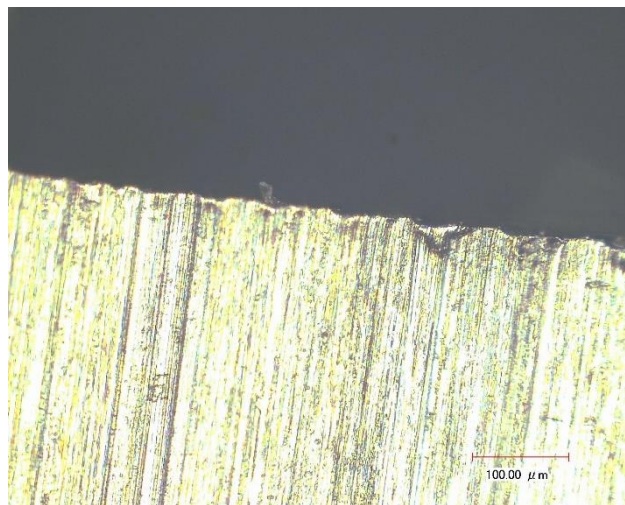microscope.

Fig. 5.7 Image of entrance burr in up milling for stainless steel 6 enlarged by digital
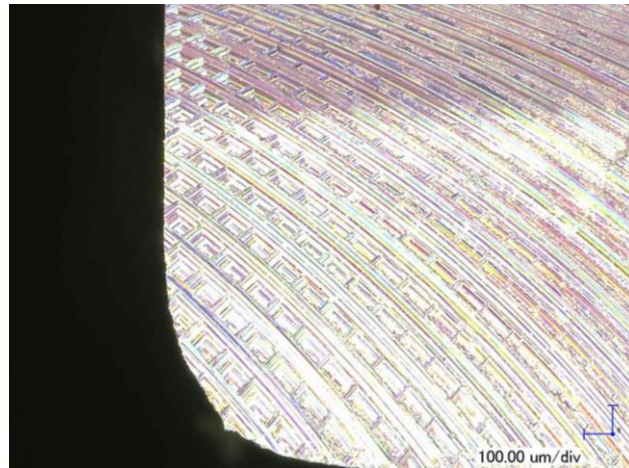microscope.

Fig. 5.8 Image of entrance burr in up milling for AlMg0.5Si enlarged by digital microscope.
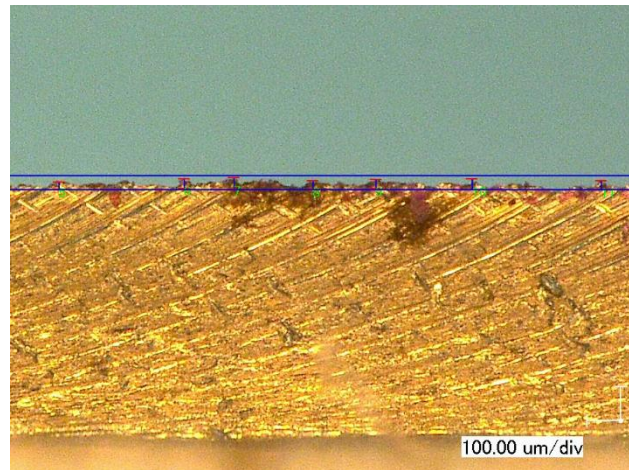

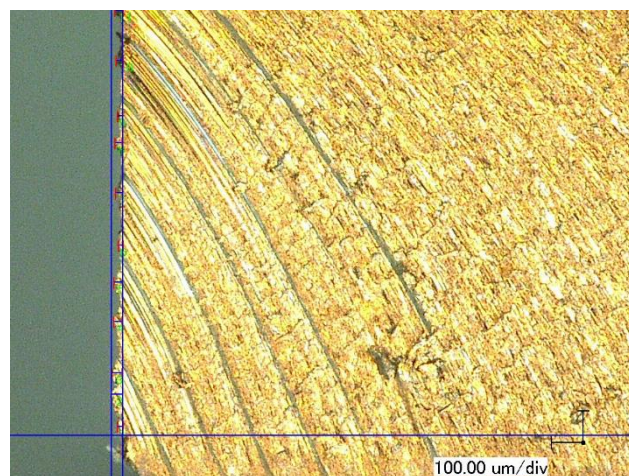Fig. 5.9 Image of entrance burr in down milling for steel C: 0.45 % enlarged by digital microscope.

Fig. 5.10 Image of entrance burr in up milling for steel C: 0.45 % enlarged by digital microscope.

Comparisons of the predicted burr sizes (using the first cutting force calculation method) and experimental burr sizes for the exit and top burrs in up milling and down milling are shown in Figs. 5.11-5.17.

Fig. 5.11 Comparison of top burrs in up milling of steel C : 0.45%.

Fig. 5.12 Comparison of top burrs in down milling of steel C: 0.45 %.

Fig. 5.13 Comparison of exit burrs in cutting direction of steel C: 0.45 %.

Fig. 5.14 Comparison of exit burrs in feed direction of steel C: 0.45 %.

Fig. 5.15 Comparison of top burrs in down milling of gray cast iron 250.
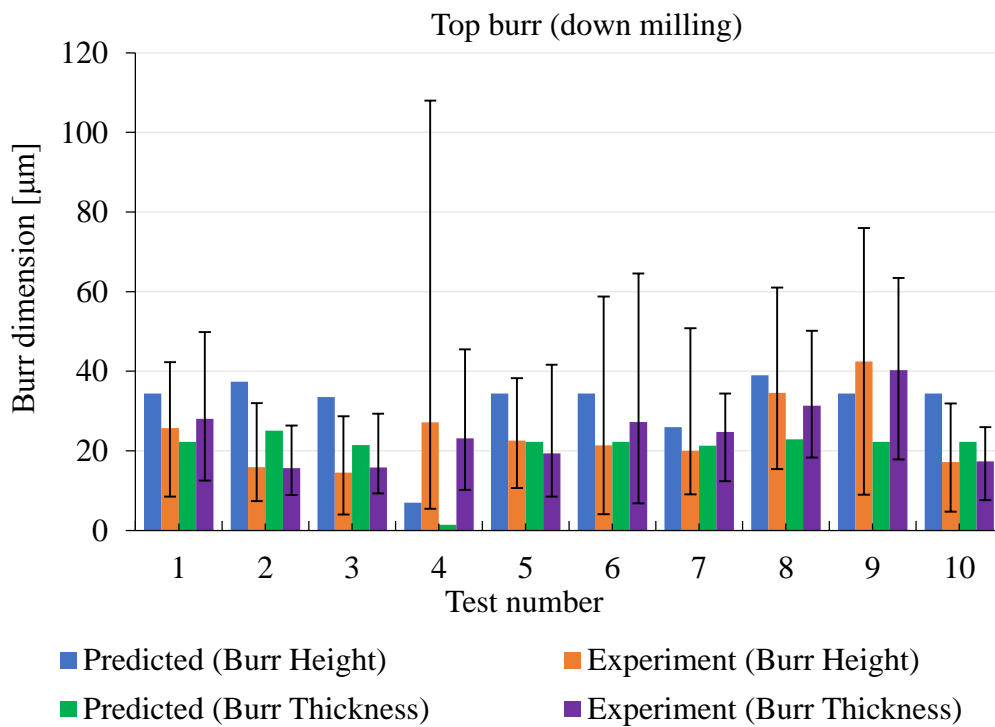
Fig. 5.16 Comparison of top burrs in down milling of stainless steel 6.
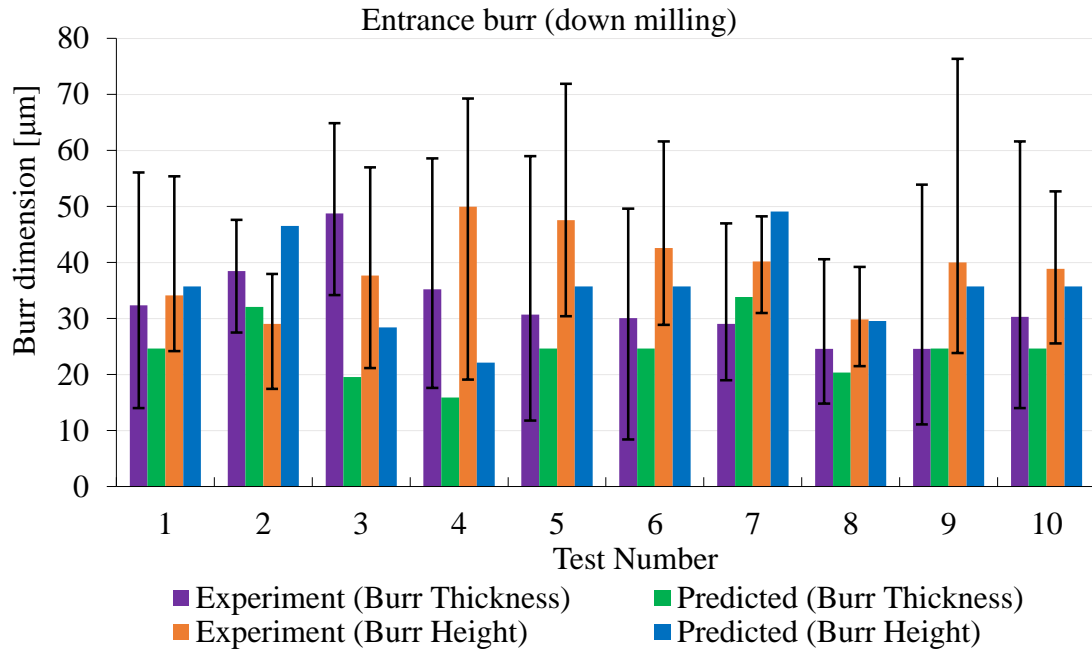
Fig. 5.17 Comparison of entrance burrs in down milling of steel C: 0.45 %.

Comparisons of the predicted burr sizes (using the second cutting force calculation method) and experimental burr sizes for the exit and top burrs in up milling and down milling are shown in Figs. 5.18-5.23.
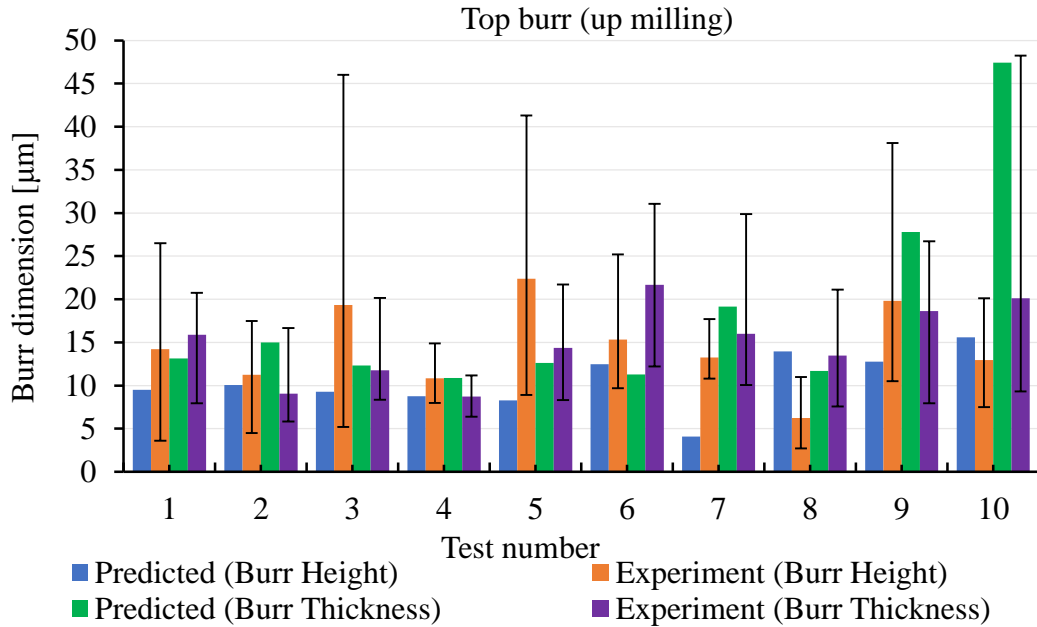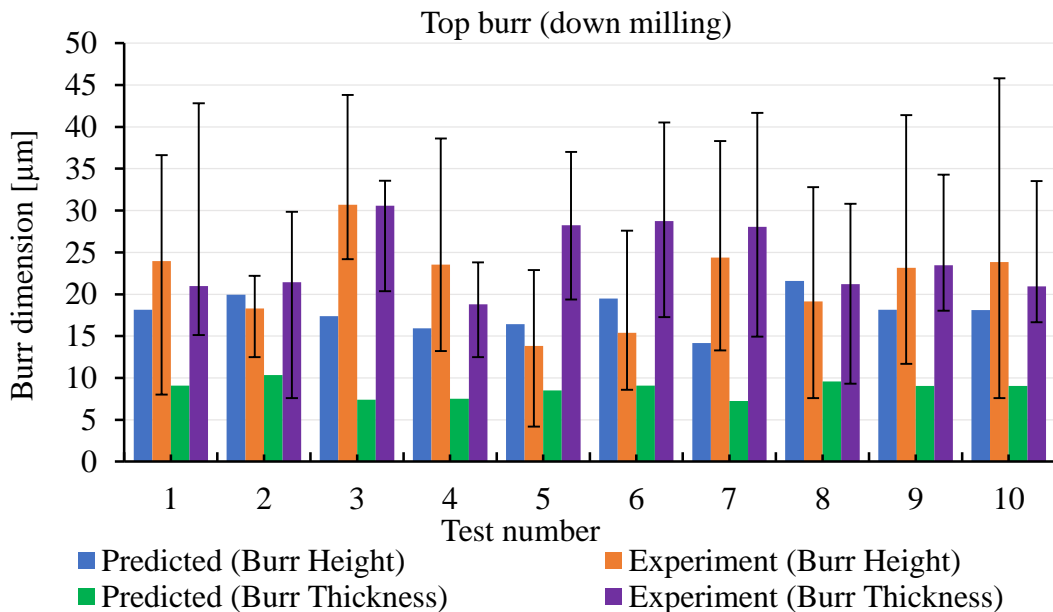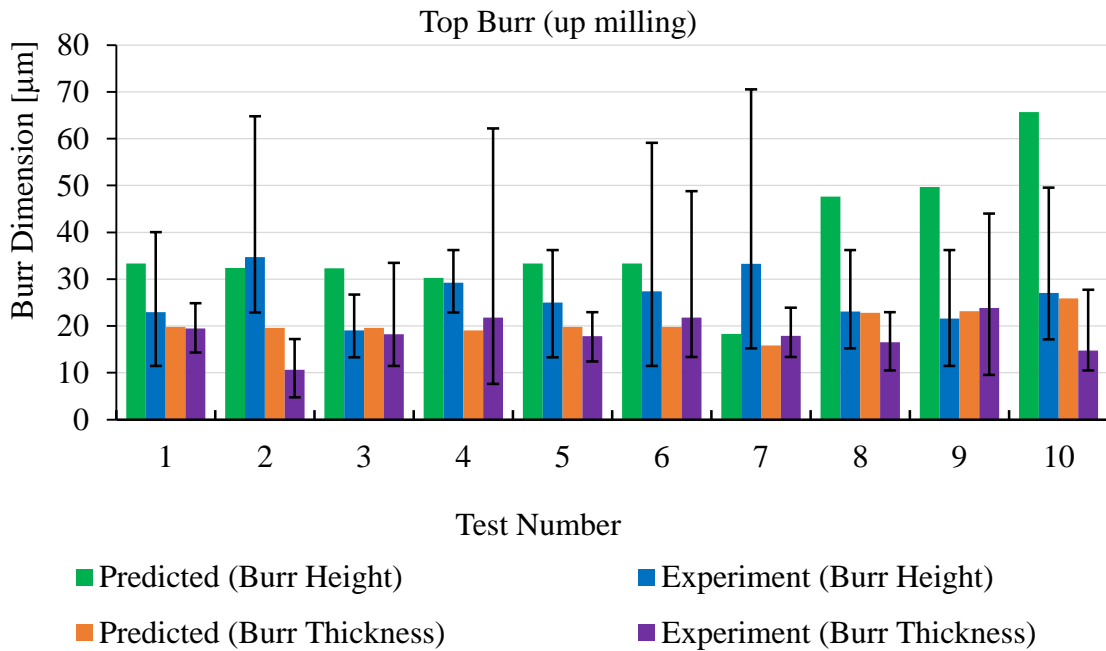

Fig. 5.18 Comparison of top burrs in up milling of steel C: 0.45 %.
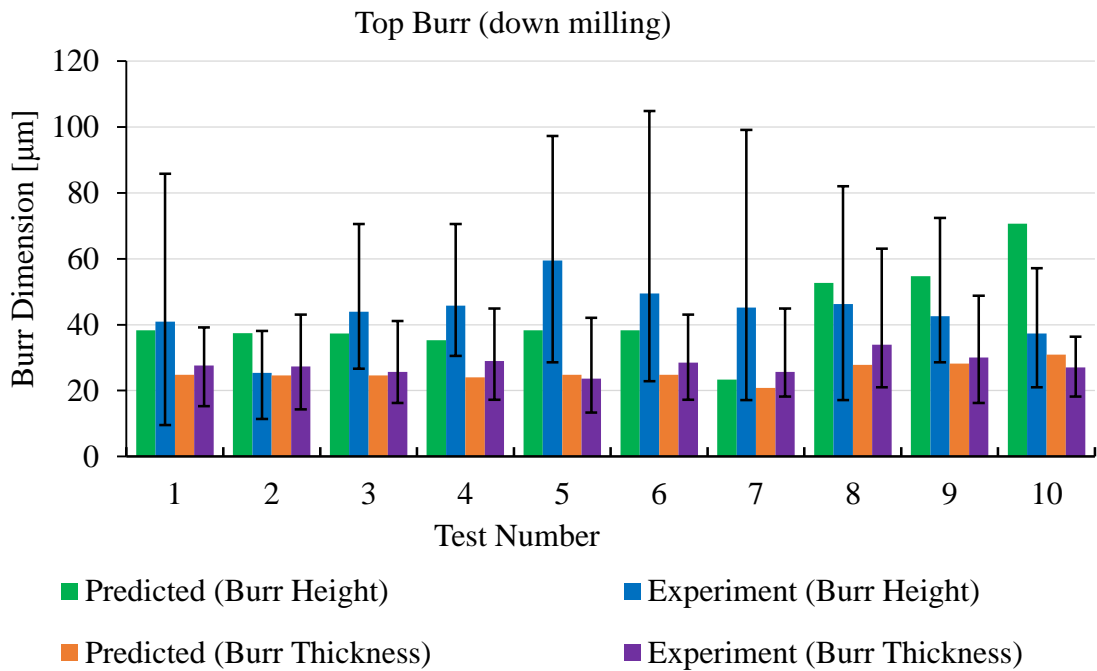
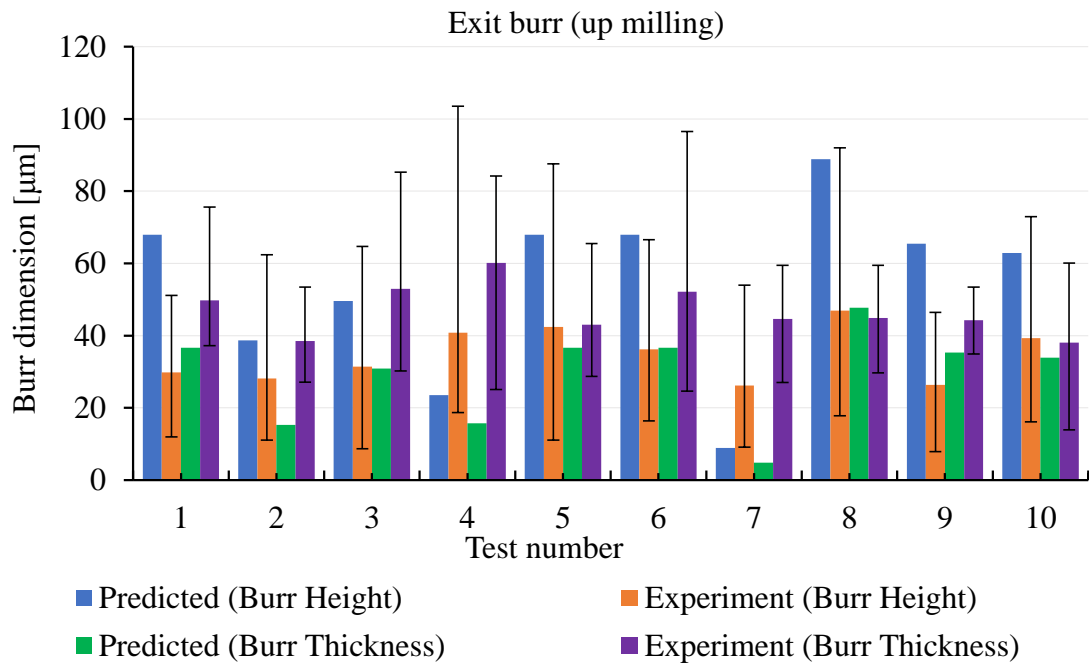Fig. 5.19 Comparison of top burrs in down milling of steel C: 0.45 %.
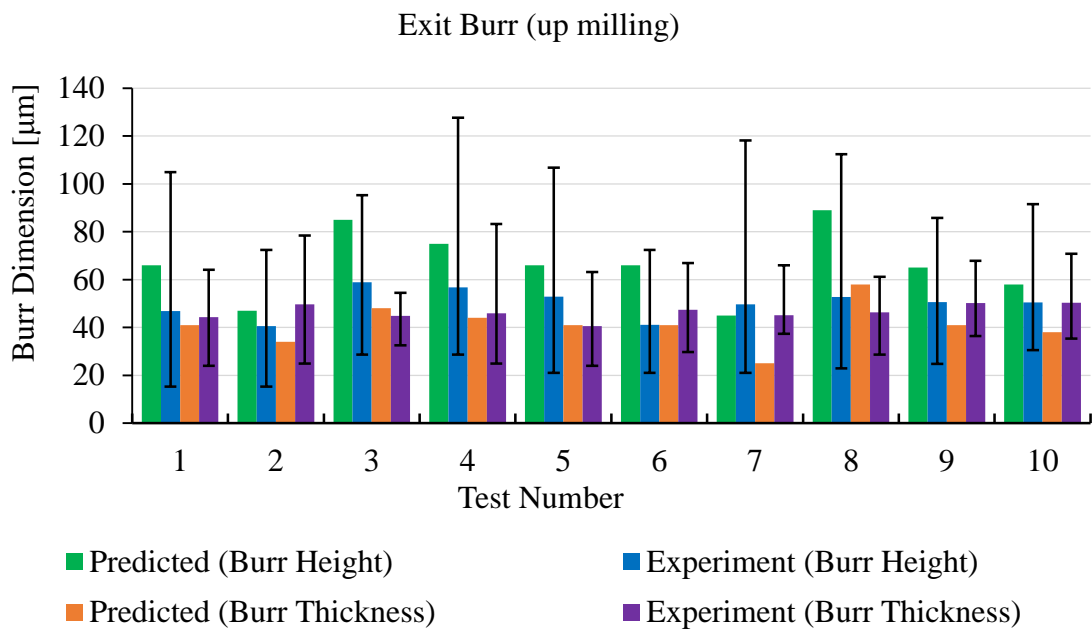
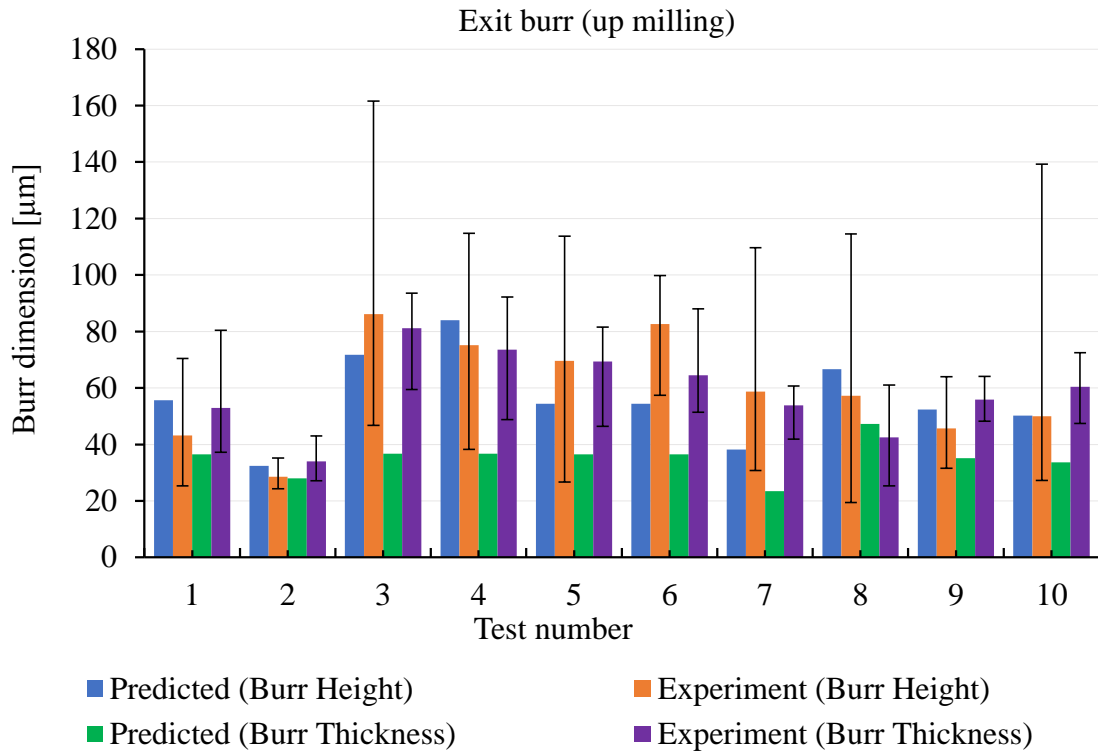Fig. 5.20 Comparison of exit burrs in up milling of steel C: 0.45 %.

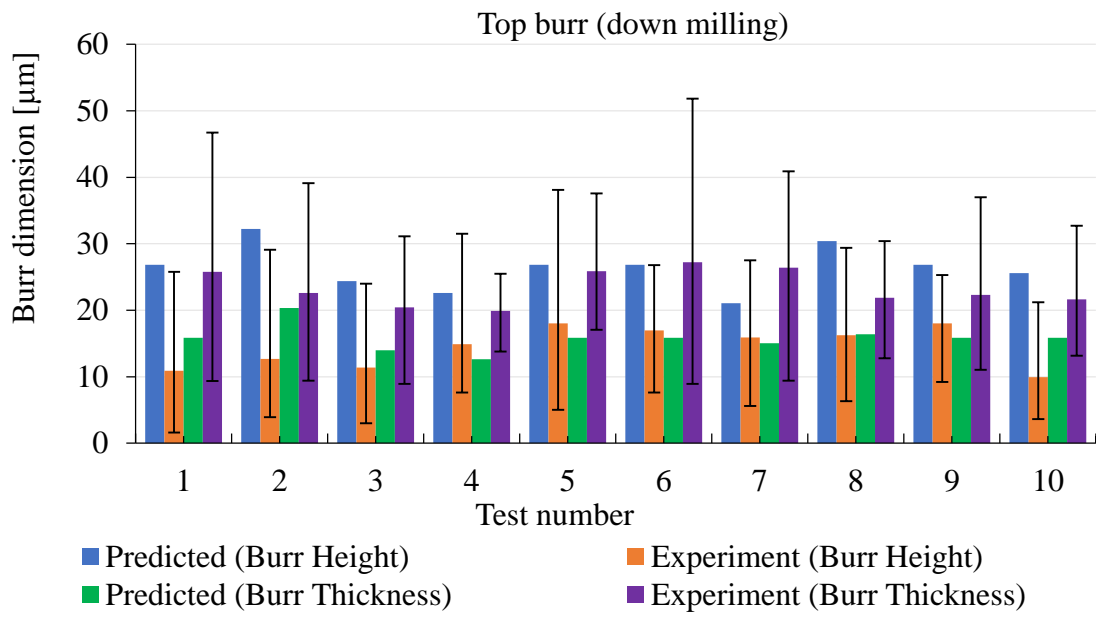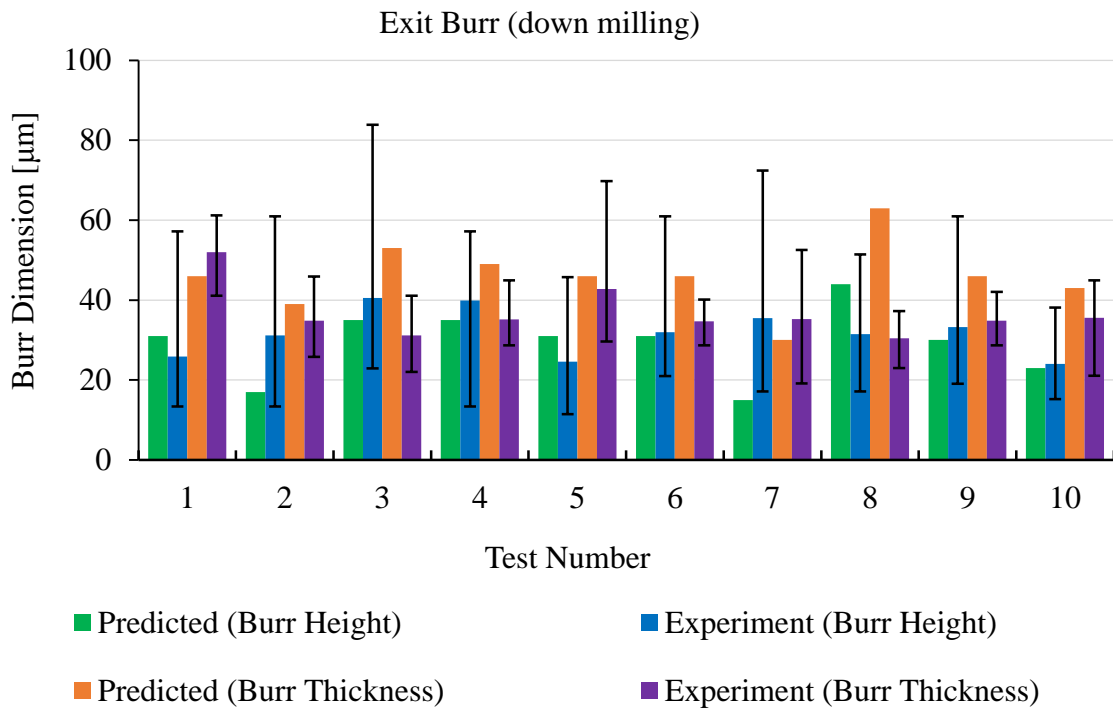Fig. 5.21 Comparison of exit burrs in down milling of steel C: 0.45 %.
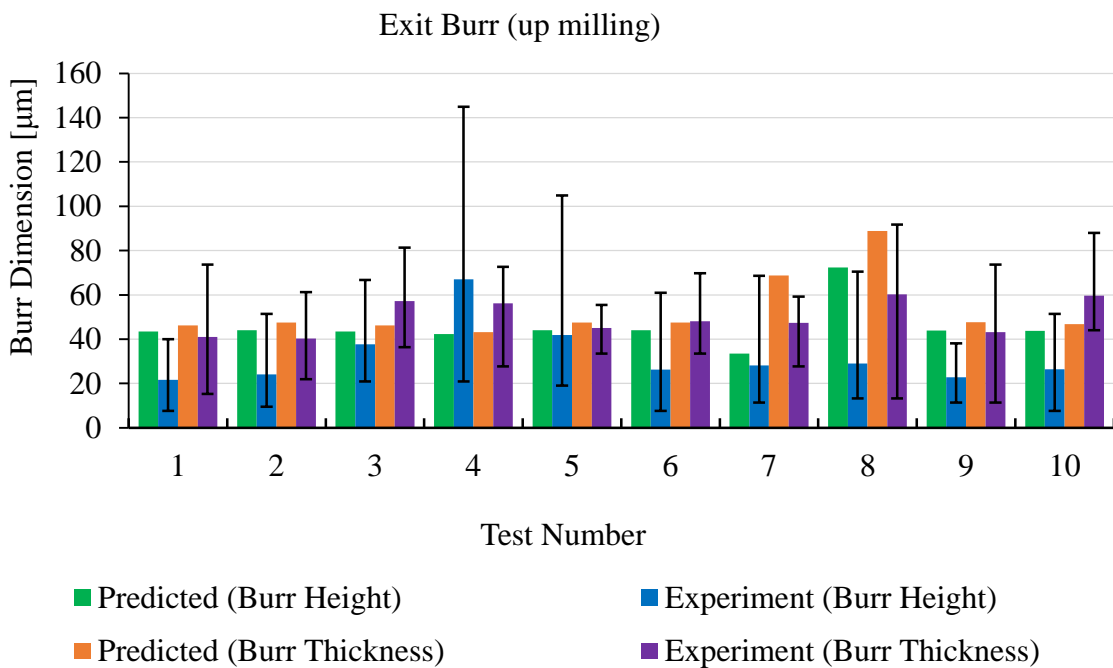
Fig. 5.22 Comparison of exit burrs in up milling of AlMg0.5Si.
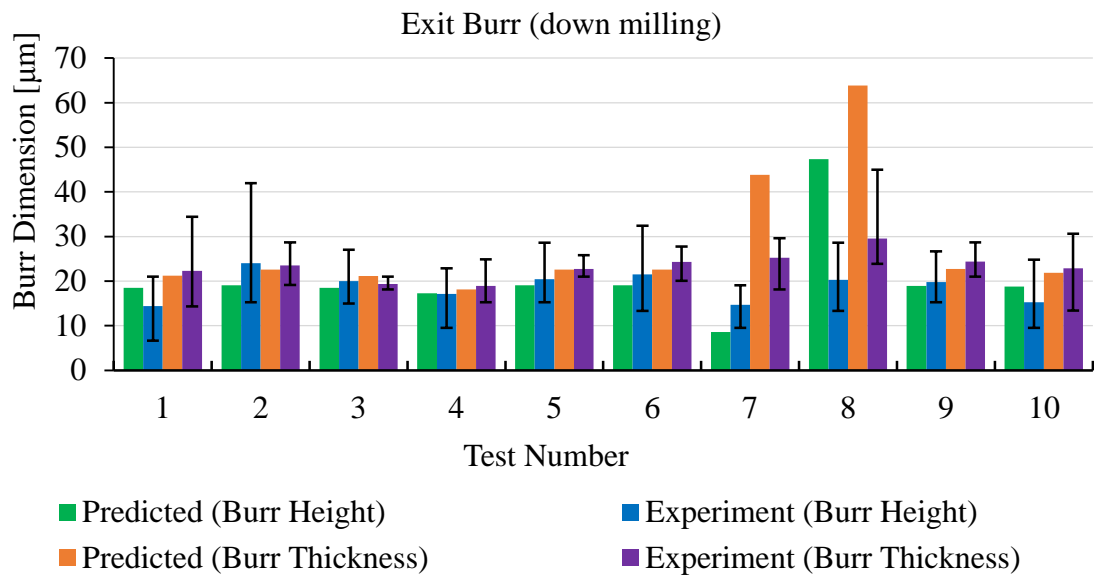
Fig. 5.23 Comparison of exit burrs in down milling of AlMg0.5Si.

The burr simulation result for a complex shape is shown in Fig. 5.24, and the planning results for three tool paths used in the up milling and down milling of a complex target shape are shown in Figs. 5.26-5.31.
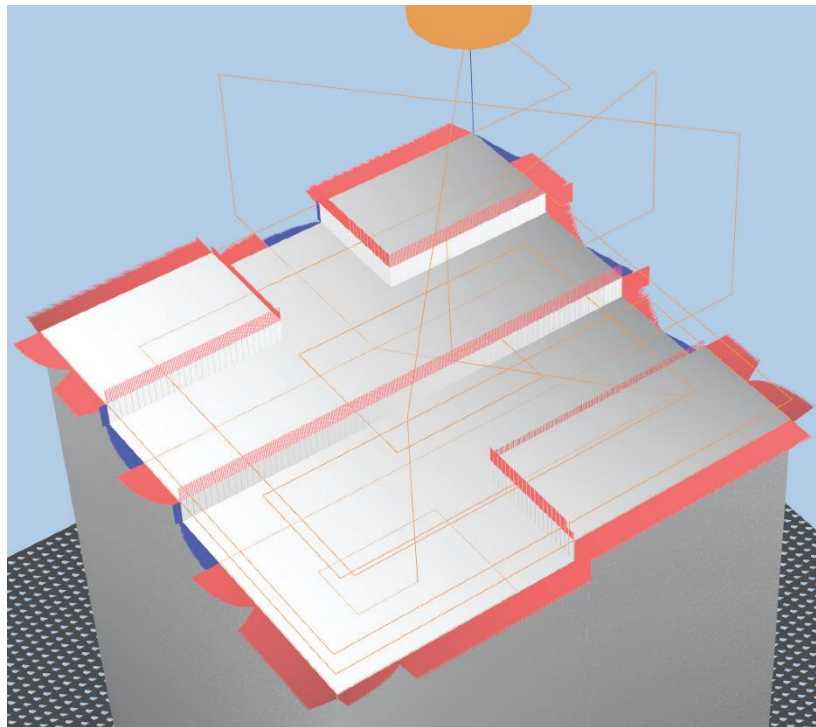
Fig. 5.24 Burr simulation for complex shape.

The details of the complex shape are shown in Fig. 5.25. All of the dimensions are in millimeters. Three layers were used to machine the complex shape.

- First layer: the cutting tool machined the first layer using a depth of cut of 2 mm. Thus, burrs were formed on the workpiece edges.
- Second layer: after finishing the first layer, the cutting tool machined the second layer using a depth of cut of 2 mm. Thus, burrs were formed on the workpiece edges in the second layer plan.
- Third layer: finally, the cutting tool machined the third layer using a depth of cut of 2 mm. Thus, burrs were formed on the workpiece edges in the third layer plan.

The tool paths that were used to machine the target shape were tool path types A, B, and C for up milling and down milling. The machine time and burr height results from the burr simulation system are listed in Table 5.7.

Table 5.7 Evaluation of three tool types.

Tool Path		A	B	C
Up milling (Rollover burr)	Time	3min 11s	3min 50s	2min 40s
	Burr height	1mm	0.8mm	1.5mm
Down milling (Poisson burr)	Time	3min 9s	3min 48s	2min 36s
	Burr height	0.2mm	0.05mm	0.5mm
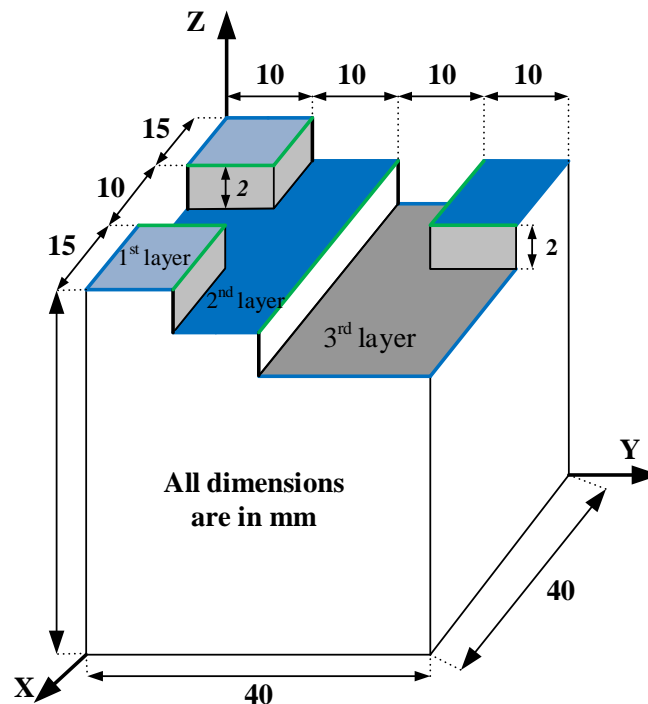
Fig. 5.25 Detailed dimensions of complex shape.
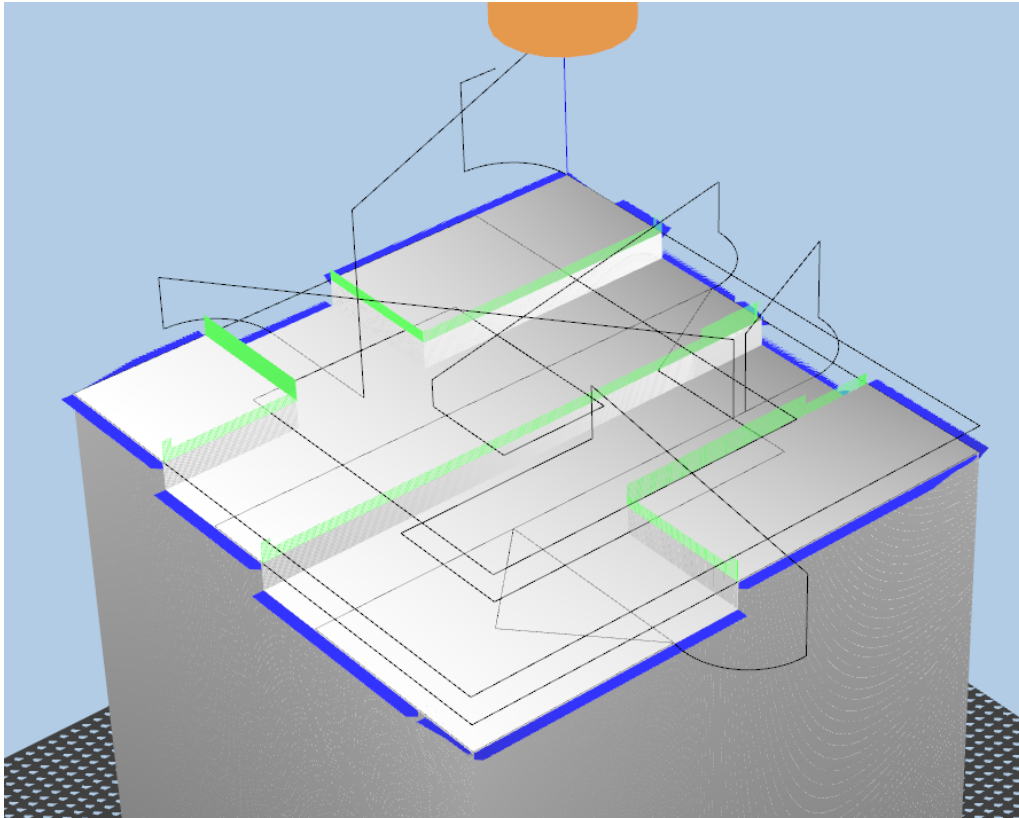
Fig. 5.26 Tool path A in down milling (burr height = 200 μm).
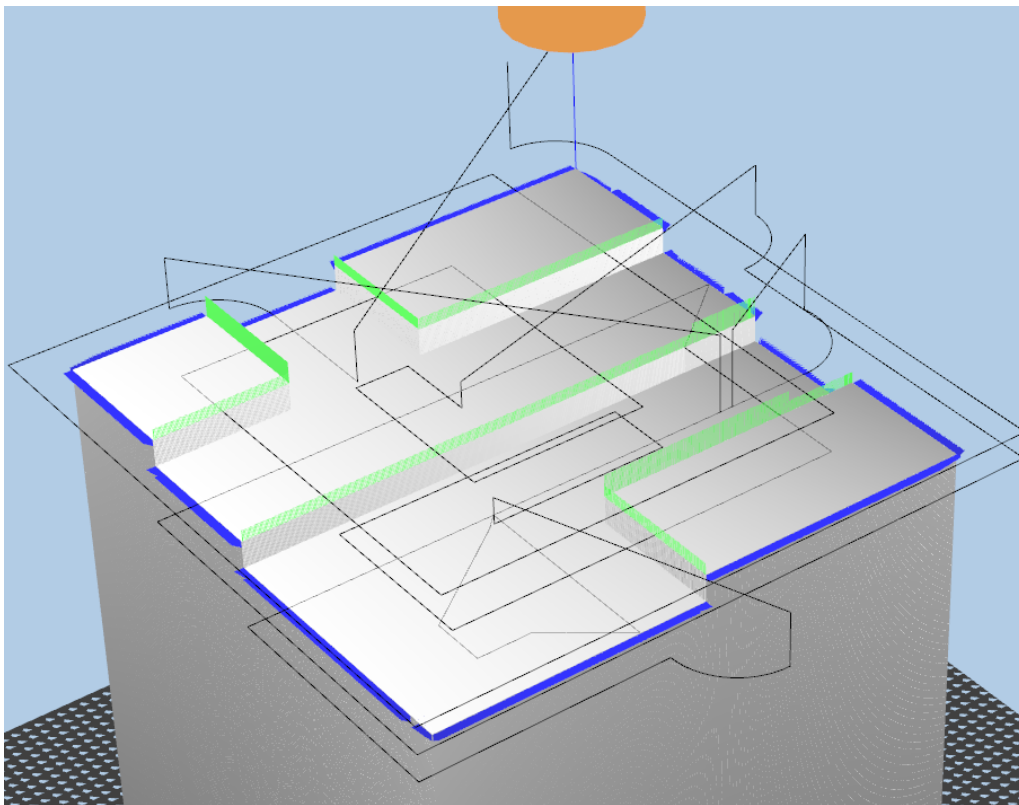
Fig. 5.27 Tool path B in down milling (burr height = 50 μm).
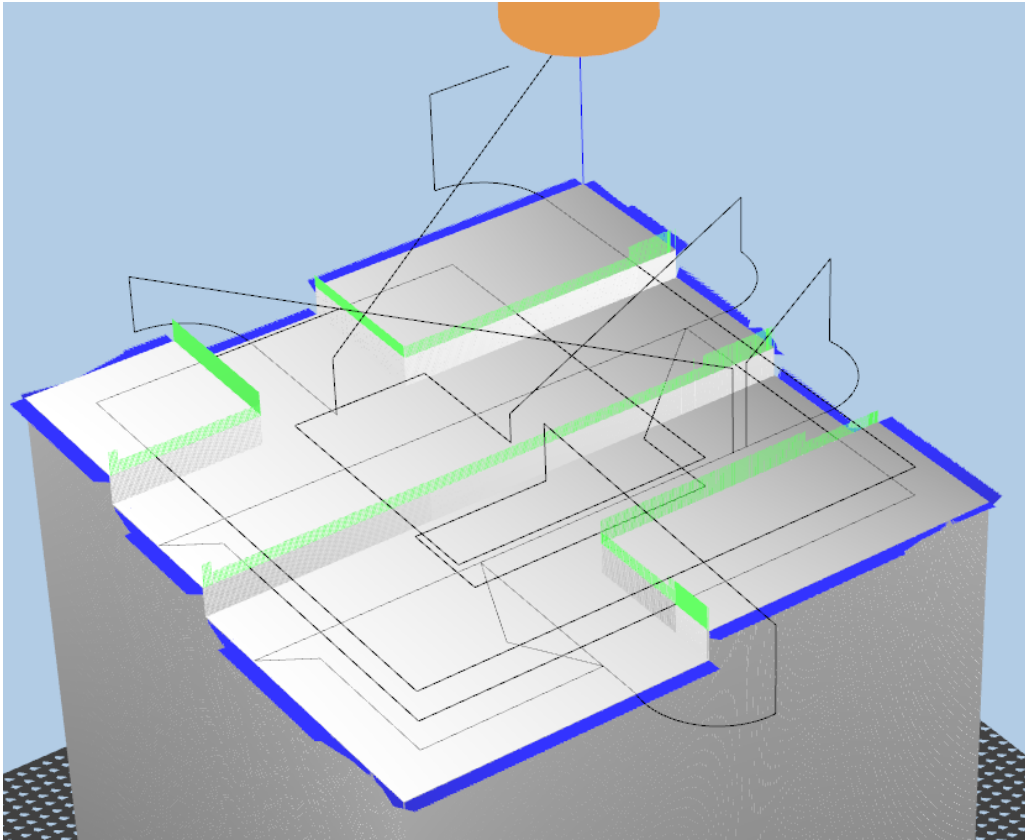
Fig. 5.28 Tool path C in down milling (burr height = 500 μm).
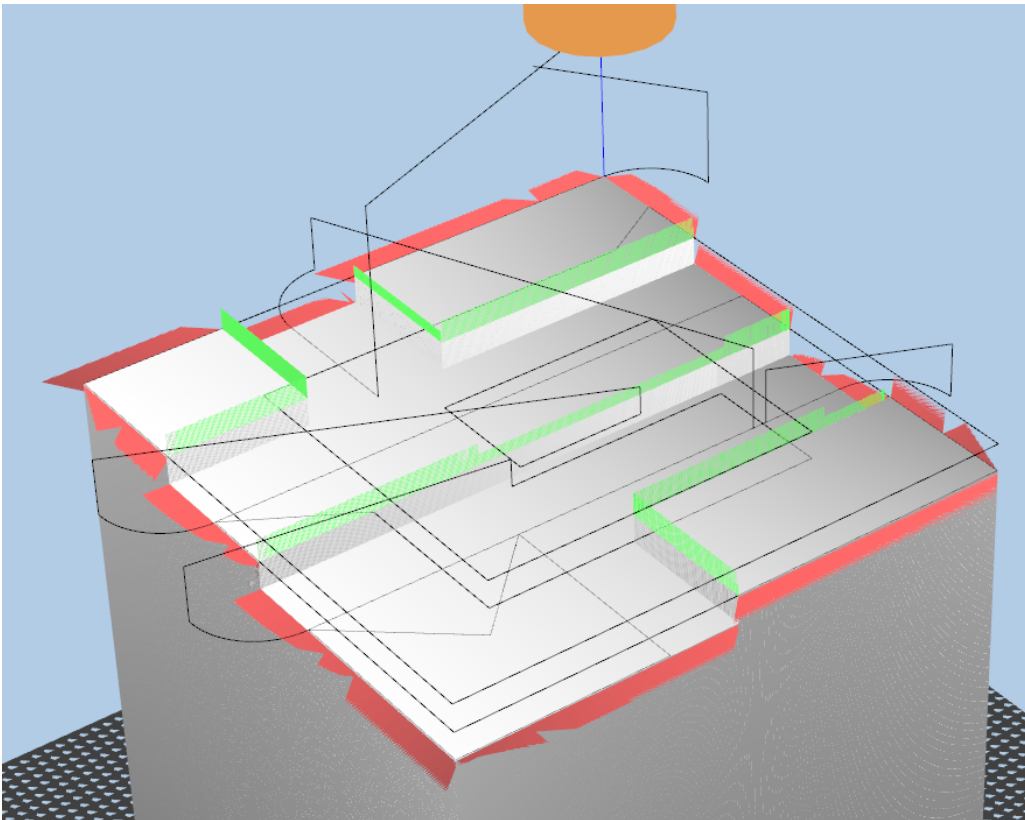
Fig. 5.29 Tool path A in up milling (burr height = 1000 μm).
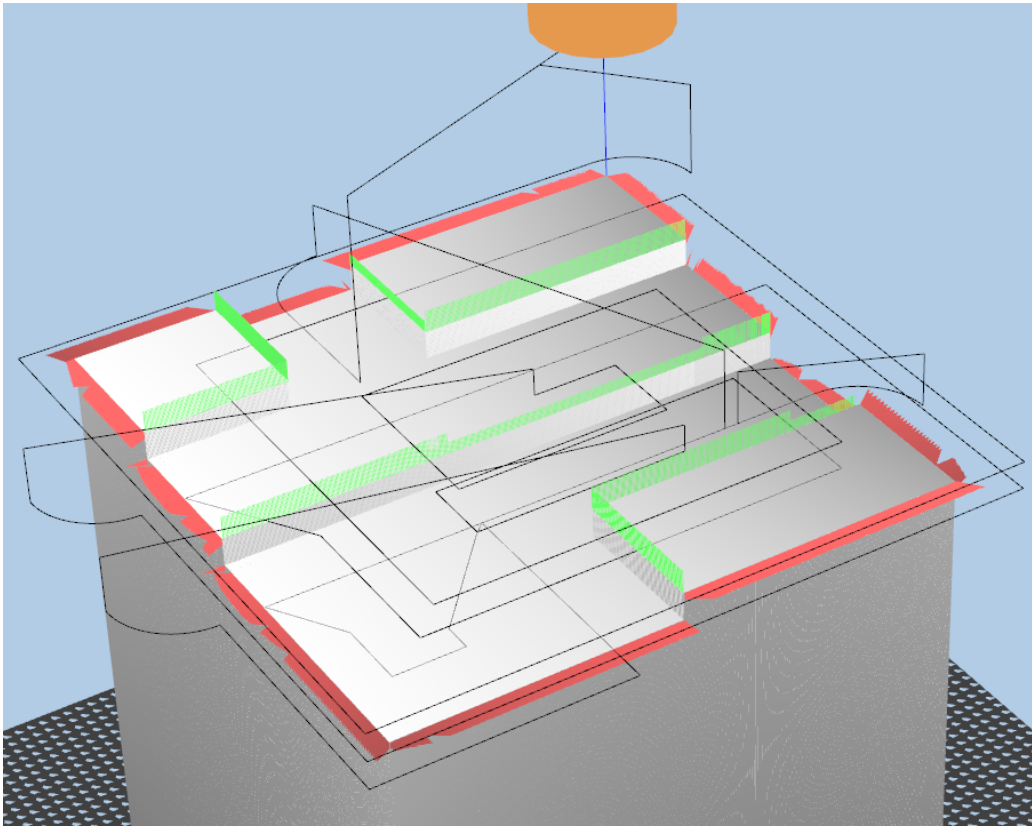
Fig. 5.30 Tool path B in up milling (burr height = 800 μm).
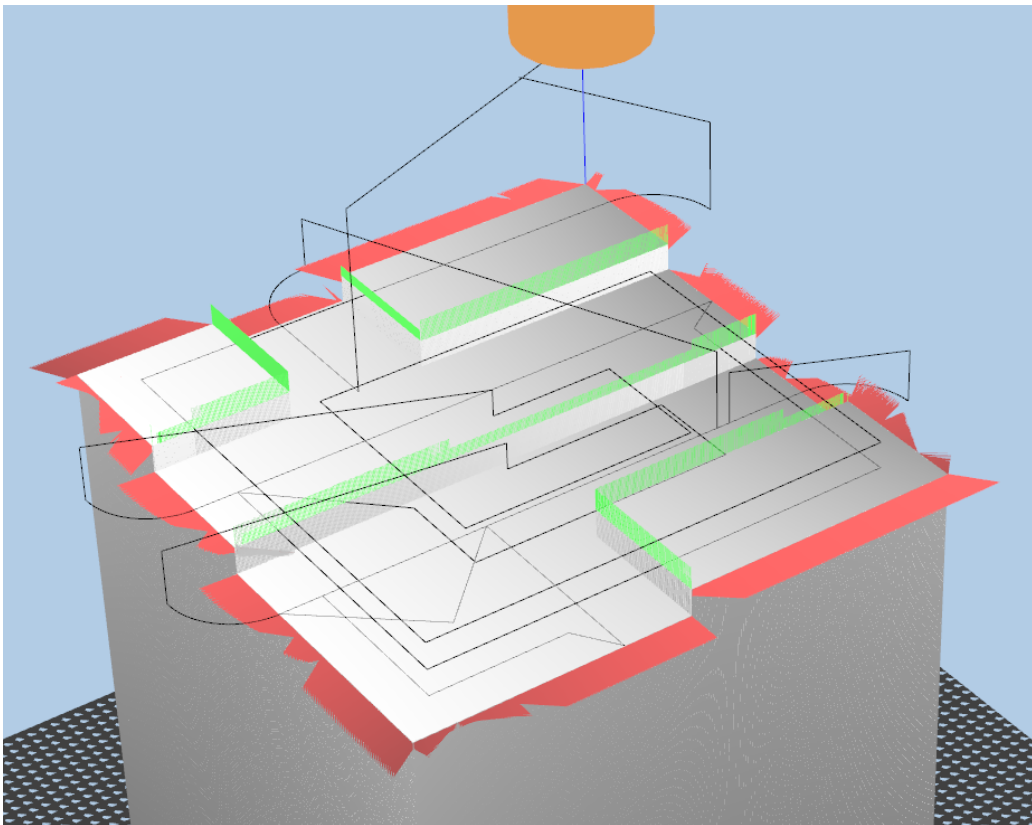
Fig. 5.31 Tool path C in up milling (burr height = 1500 μm).

5.2.2 Evaluation method for burr generation using cutting tool with flank wear

First, cutting tools were used for machining a block of steel in order to obtain three levels of flank wear (0.1 mm, 0.2 mm, and 0.3 mm), as shown in Fig. 5.32. For each flank wear leve, a cutting experiment was conducted to produce burrs based on ten cutting conditions, as listed in Table 5.8, for 20×20×30-mm blocks of steel with 0.45% carbon and aluminum alloy AlMg0.5Si, as shown in Fig. 5.33. The cutting conditions listed in Table 5.7 were set according to the cutting conditions recommended by a cutting tool company[12]. The axial depth of cut and radial depth of cut were both 2 mm. The spindle speed was increased from 800 rpm to 1200 rpm using an increment setting of 200 rpm for the steel with 0.45% carbon and from 1500 rpm to 2500 rpm using an increment setting of 500 rpm for aluminum alloy AlMg0.5Si. The feed rate was increased from 0.05 mm to 0.15 mm using an increment setting of 0.05 mm/tooth for both materials. By varying these cutting conditions, we could determine the effect of these parameters on the burr sizes. The workpiece properties are listed in Table 5.9. In this evaluation, ten experimental tests and ten simulation tests were conducted for up- and down- milling. A digital microscope (KEYENCE: VHX-600) was used to measure the burr size. The burr height and burr thickness were measured with scale measurements using an enlarged 2D image. The images were obtained at angles of 60° from the vertical direction and 90° from the horizontal direction for the burr thickness and burr height, respectively. The cutting fluid was not considered in this study. Comparisons of the predicted and experimental burr sizes of the exit burrs in up milling for steel with 0.45% carbon and aluminum alloy AlMg0.5Si are shown in Figs. 5.34 -5.39.
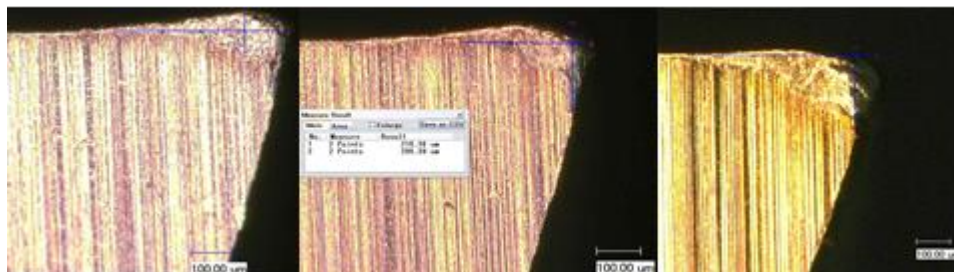
Fig. 5.32 Tool flank wear left to right 0.1 mm, 0.2 mm, and 0.3 mm.

Table 5.8 Different cutting conditions used in tests on tool with flank wear.

Test number	d_{ai} (mm)	d_r (mm)	Spindle speed (rpm)	Feed rate (mm/tooth)
Steel with 0.45% carbon				
1	2.0	2.0	1000	0.1
2	2.0	2.0	800	0.1
3	2.0	2.0	1200	0.1
4	2.0	2.0	1000	0.05
5	2.0	2.0	1000	0.15
Aluminum alloy AlMg0.5Si				
1	2.0	2.0	2000	0.1
2	2.0	2.0	1500	0.1
3	2.0	2.0	2500	0.1
4	2.0	2.0	2000	0.05
5	2.0	2.0	2000	0.15
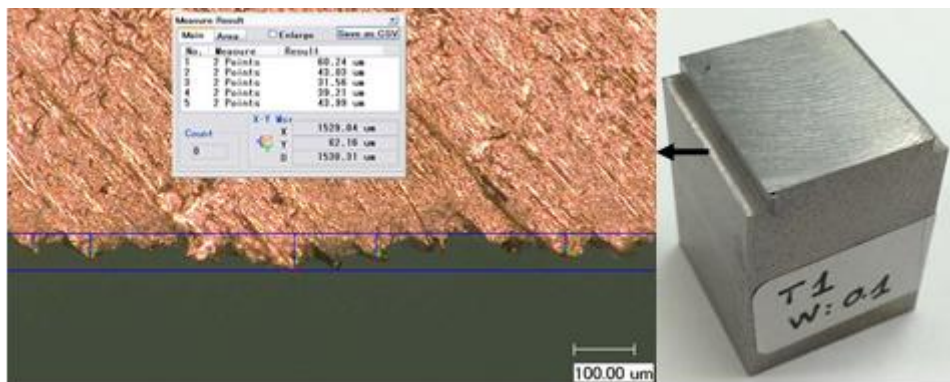
Fig. 5.33 Measurement of exit burr for steel C: 0.45 % workpiece material in test number 1 using tool with 0.1 mm of flank wear.

Table 5.9 Workpiece material properties[25]

	Ultimate tensile strength σ_u (MPa)	Yield strength σ_y (MPa)	Young's modulus E (GPa)	Poisson's ratio v
Steel C: 0.45%	569	343	205	0.29
AlMg0.5Si	152	90	68.9	0.33

Fig. 5.34 Comparison of exit burrs of steel after tool wear of 0.1 mm.

Fig. 5.35 Comparison of exit burrs of steel after tool wear of 0.2 mm.

Fig. 5.36 Comparison of exit burrs of steel after tool wear of 0.3 mm.

Fig. 5.37 Comparison of exit burrs of AlMg0.5Si after tool wear of 0.1 mm.

Fig. 5.38 Comparison of exit burrs of AlMg0.5Si after tool wear of 0.2 mm.
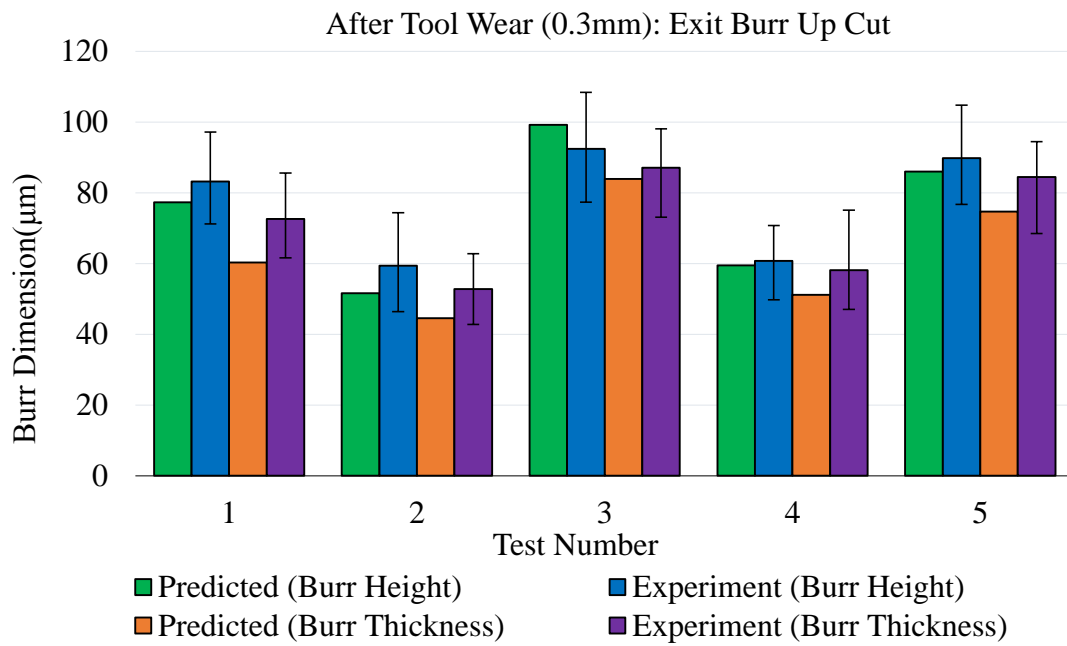
Fig. 5.39 Comparison of exit burrs of AlMg0.5Si after tool wear of 0.3 mm.

5.3 Discussion

5.3.1 Burr results using first method of cutting force calculation

The predicted and experimental values of the top burr size (thickness and height) for steel with 0.45% carbon in up milling and down milling were found to agree under most cutting conditions as shown in Fig. 5.11 and Fig. 5.12. According to the top burr results for steel with 0.45% carbon, when the depth of the cut increased, the burr thickness and height also increased in up milling. The exit burr heights in up milling in the cutting direction and feed direction for steel with 0.45% carbon were in the range of the experimental results under most cutting conditions and the exit burr thickness was also found to agree under most of cutting conditions as shown in Fig. 5.13 and Fig. 5.14. It was noticed that the radial depth of the cut had an important role on the exit burr in the feed direction. Figure 5.14 shows that the exit burr sizes increased with an increase in the radial depth of the cut. This was because the cutting tool cut in the same position numerous times before leaving the workpiece edge, where a rollover burr occurred. At this workpiece edge, the plastic deformation increased with the ductile workpiece material (steel with 0.45% carbon), causing the exit burr to grow. It was also noticed that the top burr size increased with an increase in the axial depth of the cut as shown in Fig. 5.11. With a large axial depth of cut, the cutting force was also large, which caused the top burr size to grow. The thickness and height values for the top burr in down milling for gray cast iron 250 and stainless steel 6 were also generally found to be in the experimental range, as shown in Fig. 5.15 and Fig. 5.16. Based on the results shown in Figs. 5.11-5.16, we can say that the predicted and experimental results agreed under most of the cutting conditions. As an example, the results of tests 1-6, and 8-10 in Fig. 5.11 show good agreement for both the burr height and burr thickness in comparisons of the predicted and experimental results. However, test 7 showed a small disagreement between the predicted burr height and the experimental result. Thus, about 90% of the results had good agreement. Similarly, good agreement was found in comparisons of the results for exit burrs in up milling, as shown in Figs. 5.13-5.14, and top burrs in down milling, as shown in Figs. 5.12, 5.15, and 5.16. In addition, the system was also tested with a complex target shape. The different types of burrs were recognized automatically at the different locations, as shown by different colors in Fig. 5.24. The red and blue colors represent rollover and Poisson burrs respectively. The workpiece for the target shape was steel with 0.45% carbon, and the cutting conditions were the same as those for test 1. The system could predict

and display the burr size and burr direction in different positions. Thus, the system is also useful for process planning to avoid and minimize exit burrs.

5.3.2 Burr results using second method of cutting force calculation

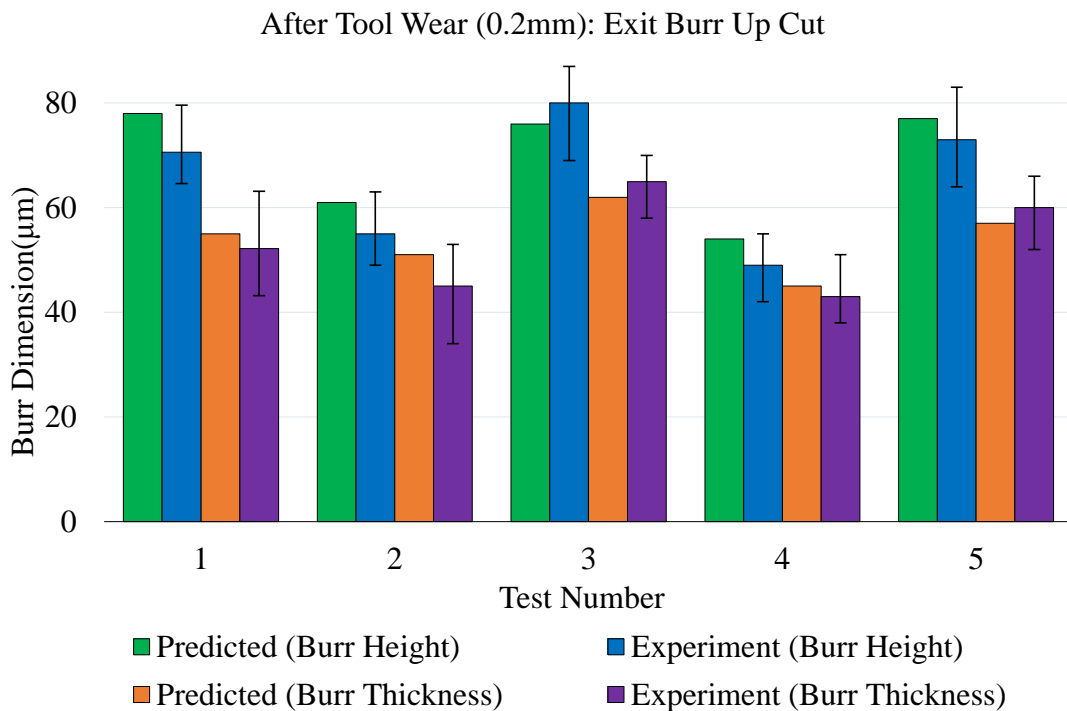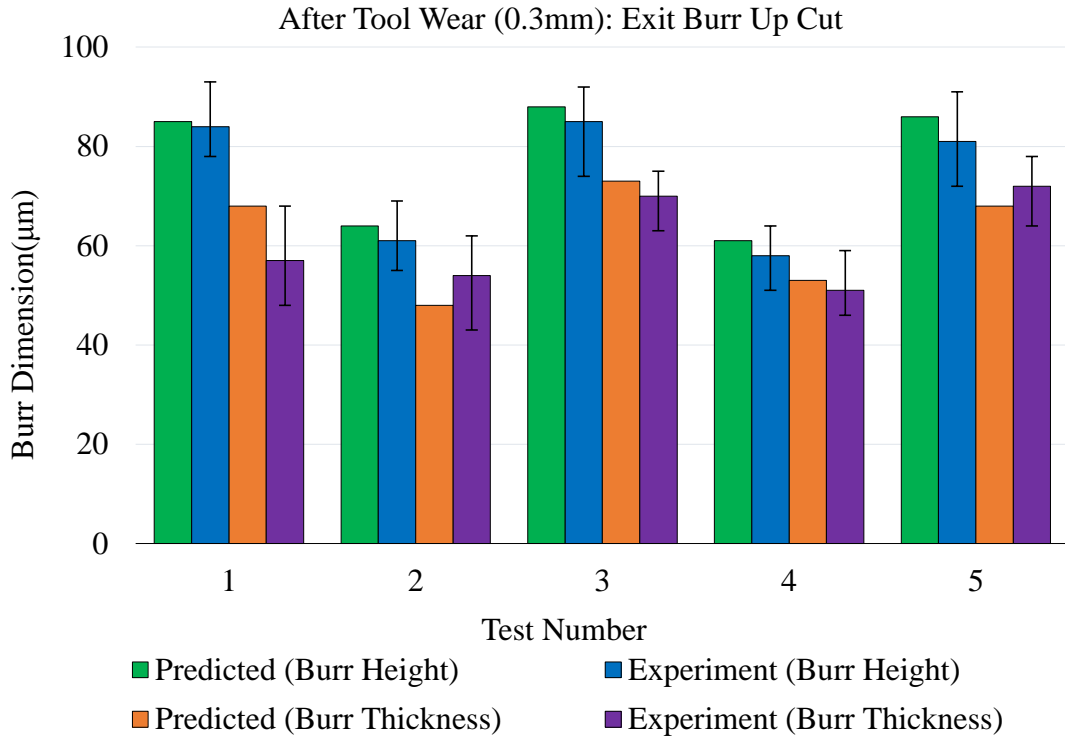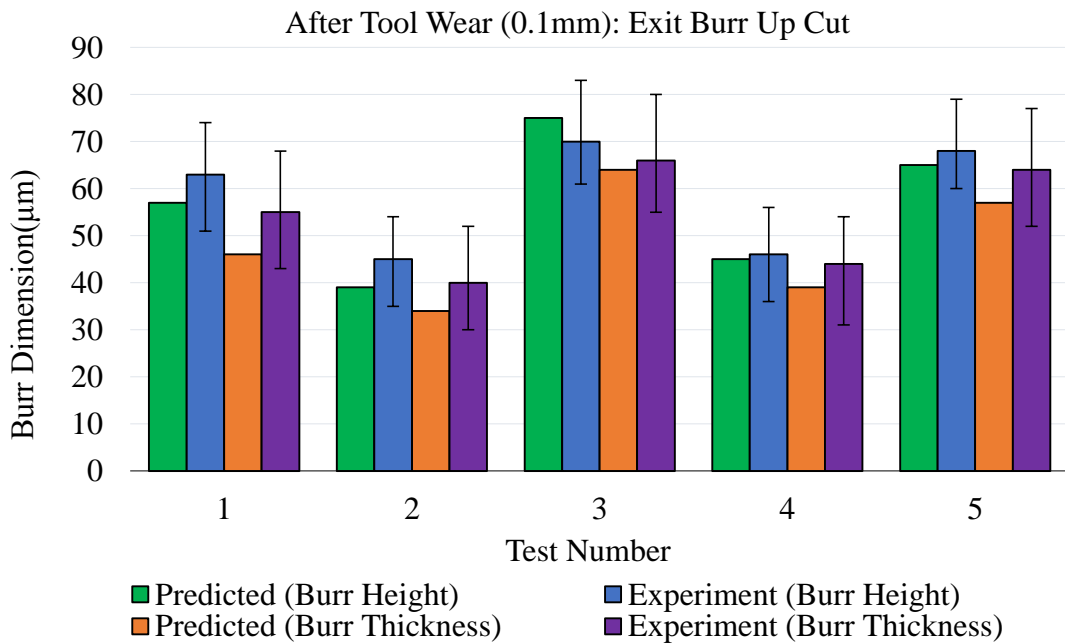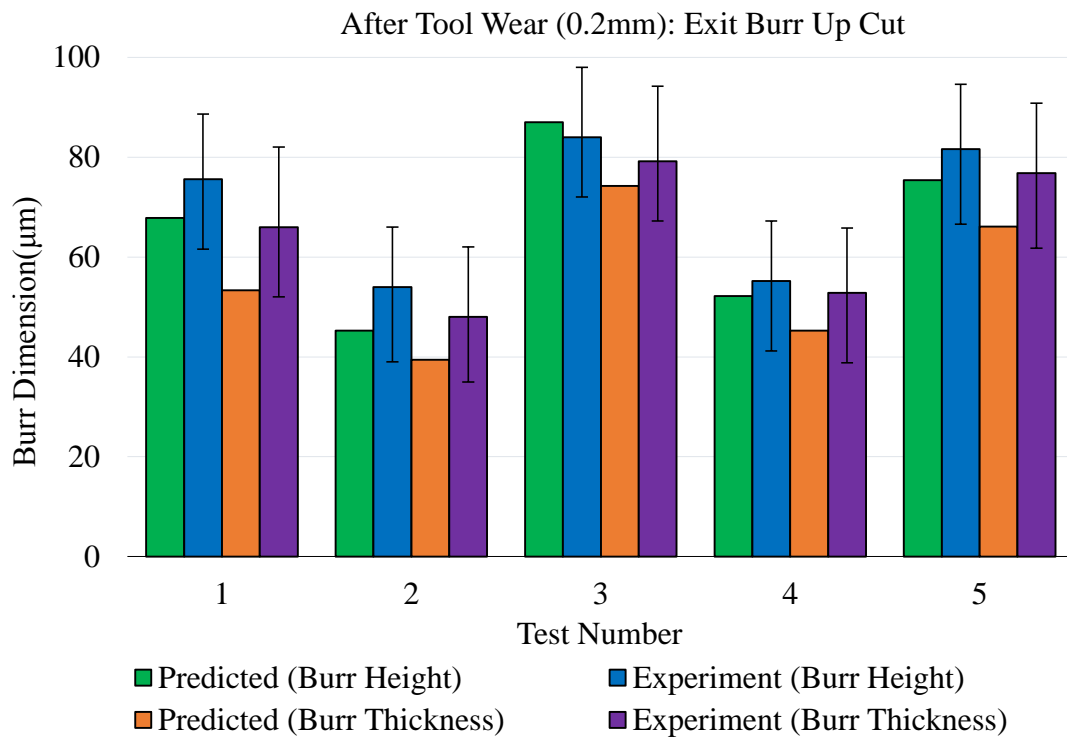The predicted and experimental values of the top burrs and exit burrs (height and thickness) for steel with 0.45 % carbon and aluminum alloy AlMg0.5Si in up milling and down milling were found to agree under most of cutting conditions, as shown in Fig. 5.18 to Fig. 5.23. It was noticed that the axial depth of cut had an important effect on the top burr and exit burr. When the axial depth of cut increased, the top burr size increased, whereas the exit burr size decreased. The radial depth of cut and spindle speed had less effect on burr growth. The feed rate per tooth also had an important effect on both the top burr and exit burr for both materials. The burr size grew linearly with an increase in the feed rate. The exit burr in up milling is always large compared to the entrance burr in down milling. In up milling, tool path B gave a small exit burr height, but increased the machine time, while tool path C decreased the machine time but gave a large exit burr. In down milling, tool path B gave the smallest entrance burr height but the largest machine time, while tool path C decreased the machine time but increased the entrance burr height. The tool path in down milling completely avoided the tool exit, and thus generated the smallest burr. Based on the simulations for tool paths A, B, and C, as shown in Figs. 5.26-5.31, the exit burr increases with an increase in the in-plane exit angle.

5.3.3 Comparison between first method and second method of cutting force calculation

It is noticed that the burr simulation results based on the first and second method are not so different. The second method is saves time because it does not require any experimental test to define the cutting constant as the first method.

5.3.4 Burrs results using cutting tool with flank wear

The predicted and experimental values of the exit burr size (thickness and height) for S45C in up milling and down milling were found to agree under most cutting conditions (Figs. 5.34 -5.39). It was noticed that the spindle speed had an effect on the burr growth. The feed rate per tooth also had an important effect on the exit burrs for both materials. The burr size grew linearly with increases in the feed rate and spindle speed. When the tool flank wear increased, the size of the exit burr also increased.

5.3.4 Effects of radial depth of cut, axial depth of cut, and feed rate on exit side burr and top burr

The radial depth of cut had the most significant influence on the exit side burr. When the radial depth of cut increased, the height of the exit side burr increased, as shown in Fig. 5.40. This was a rollover burr, and grew because the cutting tool made multiple cuts before it exited the workpiece edge. Thus, a larger radial depth of cut will cause the height of the exit side burr to grow.
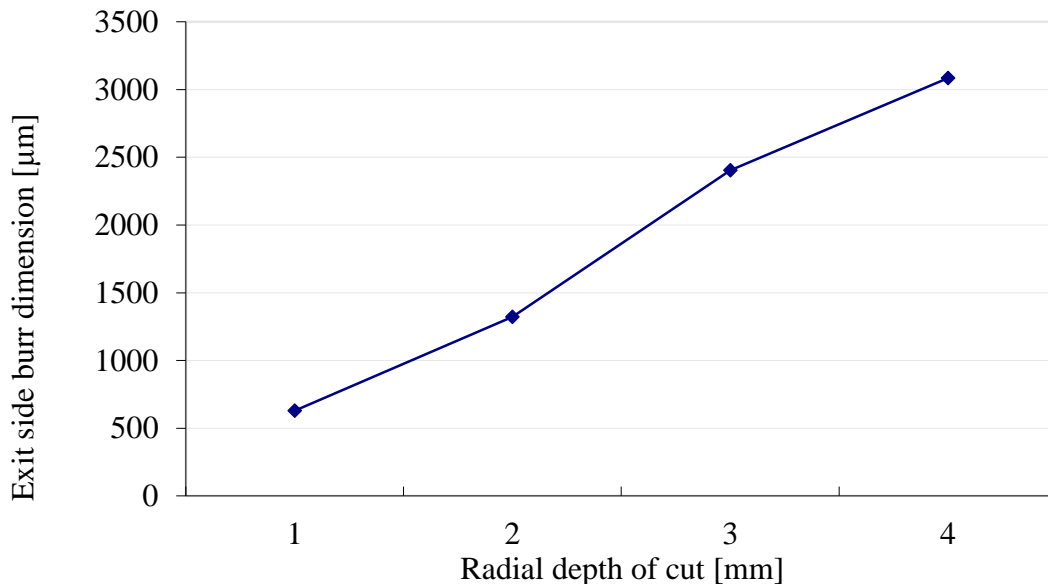
Fig. 5.40 Effect of radial depth of cut on exit side burr for workpiece material steel C: 0.45 % .

The axial depth of cut had a great influence on the top burr. Because the rollover burr model was applied for a top burr, the initial tool distance had a great effect on the cutting force. A larger axial depth of cut required a larger cutting force. Thus, the burr thickness of the top burr grew as shown in Fig. 5.41.
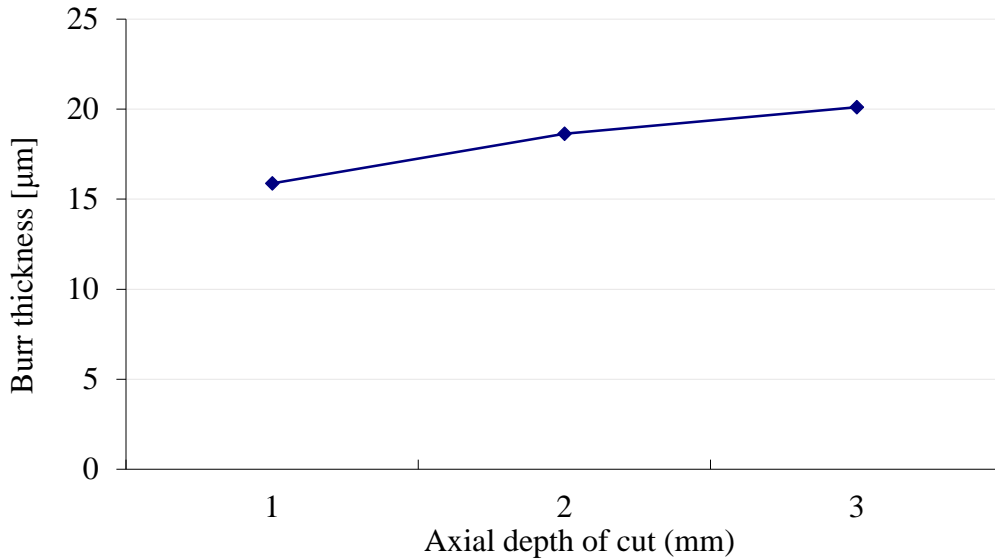
Fig. 5.41 Effect of axial depth of cut on burr thickness of top burr for workpiece material steel C: 0.45 % .

The effect of the feed rate per tooth on the top burr thickness was considered. An increase in the radial depth of the cut decreases the size of the initial tool distance is shown in Eq. (2.13) and Eq. (2.14). Thus, an increase in the feed rate per tooth decreases the burr thickness of the top burr, as shown in Fig. 5.42.
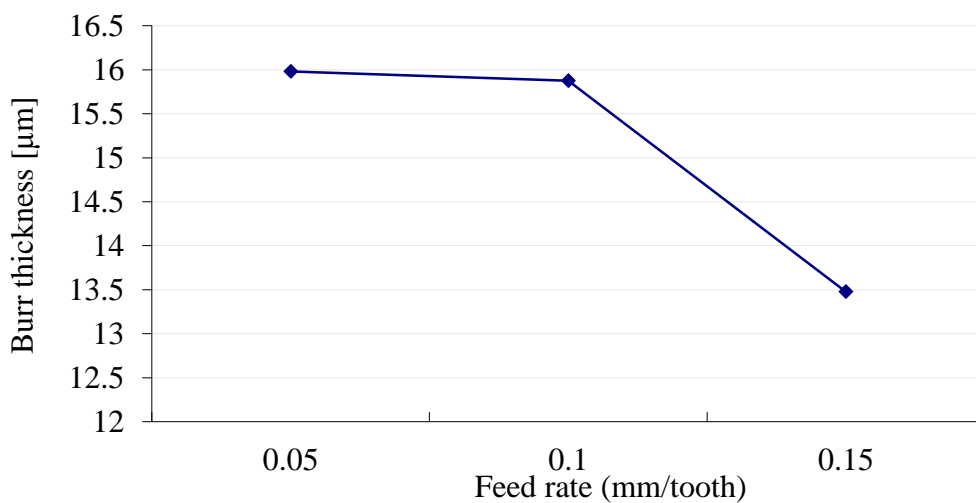
Fig. 5.42 Effect of feed rate on burr thickness of top burr for workpiece material steel C: 0.45 % .

5.4 Chapter summary

In this chapter, the burr prediction system proposed in Chapter 4 was demonstrated to have the ability to estimate the size of burrs in peripheral end milling and for a complex target shape. An evaluation of the burr prediction system, which involved many experiments, was conducted for various cutting conditions and workpiece materials. Experimental machining tests using a fresh tool and tool with flank wear were conducted to generate burrs in the end milling process and compare the results from the burr prediction simulation. The effects of the cutting conditions were also discussed.

Chapter 6

6. Conclusion

6.1 Conclusion

The most dominant factor limiting automated production in end milling is the generation of burrs during cutting. The current manual deburring method is a workable solution; however, there are several limitations. It is tedious, time-consuming and produces undesirable part dimensions. Burr prediction is an effective method and can be used as a preventive method with practical applications.

In this thesis, a system of burr prediction for end milling has been derived using burr formation models, an analytical cutting force model, the tool geometry, the tool wear, and experimental validation. A burr prediction system for end milling has been developed using two analytical cutting force models: cutting constants obtained from an experiment and from basic calculations. In addition, a method for minimizing burrs generation using tool path planning was developed. The effects of tool flank wear on burr formation have also been examined. Finally, the proposed method of the burr prediction system for end milling was evaluated. Each chapter can be summarized as follows.

Chapter 2 discussed basic burr formation and the parameters that influence burrs. The definition of a burr was given, and the types of burrs formed in end milling were described. Two kinds of burr models (Poisson burr and rollover burr models) were described in detail with cutting processes, orthogonal cutting and oblique cutting. The burr measurement method was also illustrated.

Chapter 3 described the classification of burrs in end milling and the application of the burr model for each burr type. The burrs in end milling were classified as entrance burrs, entrance side burrs, top burrs, exit burrs, and exit side burrs. This classification was based on the tool motion while engaging the workpiece edges. Two kinds of burr models were used in

this study. The Poisson burr was used when the cutting tool tip was pushing into a workpiece edge, while the rollover burr was used when the cutting tool tip was leaving the workpiece edge. The orthogonal and oblique cutting methods were applied based on the tool geometry motion and workpiece edge position. A summary of this application can be found in Table 3.1.

Chapter 4 described the development of the burr prediction system. There were four main parts to this chapter. The first part discussed the system architecture, which consists of two main functions: geometric simulation and physical simulation. The geometric simulation is a simulator for the machining process to represent the real cutting process. It shows the cutting tool, workpiece, tool path, real cutting movement, and especially the burr formation location with color representation. The blue and red colors represent Poisson burrs and rollover burrs respectively. A Z-map model was used in the system. By using C++ builder and graphical library OpenGL, any solid object can be represented in the simulation. In addition, the physical simulation is used as a calculation simulator for defining burr sizes. The main objective of this physical simulator is to define the cutting forces and apply the right burr model when the cutting tool engages the workpiece edge. Two methods were used for defining cutting forces: the use of cutting constants obtain from an experiment or from basic calculations. The details of these processes were described in section 4.3.4. The second part showed the method used by the geometry simulation to identify the types of burrs and apply the burr models. The geometry simulation uses the judgment rule for the Z-map height at each point of the grid coordinates to classify the types of burrs formed and apply the correct burr model formulas. The third part showed how the system was tested by executing a peripheral end milling process and simulation a workpiece with a complex shape. Tool path planning for burr minimization was also developed. The entrance burr for tool path B in down milling seemed to be reduced burr size, but machine time was increased, while tool path C in down milling gave the minimum machine time but large entrance burr. The tool path plannings were adopted a window framing scheme with a roll-ending technique in down milling, which is a good method for avoiding tool exit, thus minimizing burr formation and providing better cutting conditions than other window-framing methods. In the fourth part, burr prediction in relation to flank wear in end milling was discussed. A cutting edge wear was developed for predicting the cutting edge radius of a tool with flank wear. The cutting forces were calculated based on the prediction of the cutting edge radius wear and were used to define burr sizes.

In Chapter 5, the burr prediction system proposed in Chapter 4 was shown to have the ability to estimate the sizes and locations of burr in the end milling process. The system verification was discussed. Ten simulation and ten experimental tests were conducted using several types of workpiece materials and an end mill tool with two flutes. An evaluation of the burr prediction model was also conducted for a two-flute end milling tool with flank values of 0.1, 0.2, and 0.3 mm, using steel C:0.45% and AlMg0.5Si as the workpiece materials. The results from all the cases were discussed in section 5.3. Comparisons of the burr prediction results were made for all the cases, and the predicted and experimental results were found to agree under most of the cutting conditions. In addition, a comparison of the results of the burr prediction with flank wear showed that the proposed model could help in predicting the burr size under the effect of tool flank wear with high accuracy. The tool flank wear was shown to have significant influence on the cutting force, and an increase in cutting force resulted in a substantial increase in the burr size.

The ability to predict the sizes and locations of burrs for a given set of cutting conditions will be useful for burr control and lead to advances in manufacturing engineering.

6.2 Future research

The development of burr prediction system for end milling has several future works as follows:

1. The effect of workpiece temperature on burr formation during end milling need to consider because the temperature can change workpiece properties, which have great influence on burr mechanism.
2. The cutting speed has significant effect on cutting force in some workpiece materials, and an increase in cutting force resulted in a substantial increase in the burr size. Thus, the consideration of cutting speed in burr prediction system is necessary.
3. Some other parameters such as crater wear, machine vibration and rigidity, and thermal expansion of the cutting tool, are also important factors, which have an influence on burr formation.

BIBLIOGRAPHY

1) Gillespie, L. K. and Blotter, P. T., The Formation and Properties of Machining Burrs, Journal of Engineering for Industry, Transactions of the ASME, Vol. 98 (1), No. 75, (1976), pp. 66-74, DOI: 10.1115/1.3438875.

2) Chern, G.L. and Dornfeld, D.A., Burr/Breakout Model Development and Experiment Verification, Journal of Engineering Material and Technology, Transactions of the ASME, Vol. 118 (2), (1996), pp. 201-206, DOI: 10.1115/1.2804887.

3) Ko, S.L and Dornfeld, D.A., Burr Formation and Fracture in Oblique Cutting, Journal of Materials Processing Technology, Elsevier Science S.A., Vol. 62 (1-3), (1996), pp. 24-36, DOI: 10.1016/0924-0136(95)02125-6.

4) Hashimura, M., Chang, Y. P., and Dornfeld, D. A., Analysis of Burr Formation Mechanism in Orthogonal Cutting, Journal of Manufacturing Science and Engineering, Transactions of the ASME, Vol. 121 (1), (1999), pp. 1-7, DOI: 10.1115/1.2830569.

5) Park, I. and Dornfeld, D. A., A Study of Burr Formation Processes Using the Finite Element Method: Part I, Journal of Engineering Material and Technology, Transactions of the ASME, Vol. 122 (2), (2000), pp. 221-228, DOI: 10.1115/1.482791.

6) International Standard ISO 13715:2000, Technical Drawing - Edge of Undefined Shape - Vocabulary and Indications, ISO, Second Edition, (2000), pp. 1-13.

7) Aurich, J.C., Dornfeld, D. A., Arrazola, P.J., Franke, V., Leitz, L, and Min, S., Burrs-Analysis, Control and Removal, CIRP Annals Manufacturing Technology, Vol. 58 (2), (2009), pp. 519-542, DOI: 10.1016/j.cirp.2009.09.004.

8) Hashimura, M., Hassamontr, J., and Dornfeld, D. A., Effect of In-Plane Exit Angle and Rake Angles on Burr Height and Thickness in Face Milling Operation, Journal of Manufacturing Science and Engineering, Transactions of the ASME, Vol. 121 (1), (1999), pp. 13-19, DOI: 10.1115/1.2830566.

9) Kruy, S., Aoyama, H., Ota, K., and Sano, N., Prediction of Thickness and Height of Burr Based on Burr Formation Mechanisms in End Milling, Journal of Advance

Mechanical Design, System, and Manufacturing, Vol. 8, No. 4, (2014), pp. 1-11, DOI: 10.1299/jamdsm.2014jamdsm0045.

10) Woon, KS, Rahman, M., Neo, K.S., and Liu, K., The Effect of Tool Edge Radius on the Contact Phenomenon of Tool-Based Micromachining, International Journal of Machine Tool & Manufacture, Elsevier Ltd., Vol. 48 (12-13), (2008), pp. 1395-1407, DOI: 10.1016/j.ijmachtools.2008.05.001.

11) Yen, Y.-C., Jain, A., Altan, T., A Finite Element Analysis of Orthogonal Machining using Different Tool Edge Geometries, Journal of Materials Processing Technology, Elsevier B.V., Vol. 146 (1), (2004), pp. 72-81, DOI: 10.1016/S0924-0136(03)00846-X.

12) Mitsubishi Materials Corporation:
http://www.mitsubishicarbide.net/mmc/ja/solid_end_mills/10000184/20058434 (accessed on 10 May, 2013).

13) Oualline, Practical C++ Programming, O'Reilly, Second Edition, (2003), pp. 1-531.

14) Wright, H., et al., OpenGL SuperBigle, Addison Wesley, Sixth Edition, (2011), pp. 1-773.

15) Smid, P., CNC Programming Handbook, Industrial Press, Third Edition, (2008), pp. 1-529.

16) Armarego, E.J.A. and Brown, R.H., The Machining of Metals, Prentice-Hall, First Edition, (1969), pp. 1-437.

17) Ohta, K. and Aoyama, H., A Study on Development of Burr Prediction System in Endmilling, Master Thesis, Keio University, (2012), pp. 1-157.

18) Altintas, Y., Manufacturing Automation Metal Cutting Mechanics, Machine Tool Vibrations, and CNC Design, Cambridge University Press, Second Edition, (2012), pp. 1- 363.

19) Grzesik, W., Advanced Machining Processes of Metallic Materials, Elsevier, First Edition, (2008), pp. 1-472.

20) Abdelmoneim, M.E.S. and Scrutton, R.F., Tool Edge Roundness and Stable Build-Up Formation in Finish Machining, Journal of Engineering and Industrial, Transactions of the ASME, Vol. 96 (4), (1974), pp. 1258-1267, DOI: 10.1115/ 1.3438504.

21) Merchant, M.E., Mechanics of the Metal Cutting Process. II. Plasticity Conditions in Orthogonal Cutting, Journal of Apply Physic, Vol. 16, (1945), pp. 318-324, DOI: 10.1063/1.1707596.

22) Wright, P.K., Predicting the Shear Plane Angle in Machining from Work material Strain-Hardening Characteristics, Journal Engineering for Industry, Transactions of the ASME, Vol. 104 (3), (1982), pp. 285-292, DOI: 10.1115/1.3185832.

23) Lee, H.U., Cho, D.W. and Ehmann, K.F., A Mechanistic Model of Cutting Forces in Micro-End-Milling with Cutting-Condition-Independent Cutting Force Coefficients, Journal of Manufacturing Science and Engineering, Transactions of the ASME, Vol. 130 (3), (2008), pp. 031102-031102-9, DOI: 10.1115/1.2917300.

24) Kim, Y.J., Ko, S.L., Kim, J.H., and Kim, B.K., Development of Intelligent System to Minimize Burr Formation in Face Milling, International Journal of Advanced Manufacturing Technology, Vol. 29, (2006), pp. 879-884, DOI: 10.1007/s00170-005-2586-0.

25) Workpiece properties: http://www.matweb.com/index.aspx (accessed on December 3, 2013).

26) Kruy, S., Aoyama, H., and Sano, N., Tool Paths Planning under Window Framing Scheme for Burr Minimization, Journal of the Japan Society for Precision Engineering, Vol. 81, No. 6, (2015), pp. 598-603, DOI: 10.2493/jjspe.81.598.

LIST OF ACHIEVEMENTS

Articles on periodicals (related to thesis):

1) <u>Sothea Kruy</u>, Hideki Aoyama, Kentaro Ohta, and Noriaki Sano, "Prediction of Thickness and Height of Burr Based on Burr Formation Mechanisms in End Milling," JSME Journal of Advance Mechanical Design, Systems, and Manufacturing, Vol. 8, No. 4, (2014), pp. 1-11.

2) <u>Sothea Kruy</u>, Hideki Aoyama, and Noriaki Sano, "Tool Paths Planning under Window Framing Scheme for Burr Minimization," Journal of Japan Society on Precision Engineering, Vol. 81, No. 6, (2015), pp. 598-603.

2. Other articles on periodicals

1) Mean Vathna, Nor Suliani Abdullah, Siti Zawiah Md Dawal, Hideki Aoyama, and Sothea Kruy, "Investigation on Musculoskeletal Symptoms and Ergonomic Risk Factors at Metal Stamping Industry," Advanced Engineering Forum, Vol. 10, (2013), pp. 293-299.

3. Articles on international conference proceedings (reviewed full-length articles)

1) <u>Sothea Kruy</u>[*], Nik Fazil, Mohd Hamdi Bin Abd Shukor, and Hideki Aoyama, "Development of a Crush and Mix Machine for Composite Brick Fabrication," Proceeding of the International Conference on Advances in Materials and Processing Technologies, Paris, France, 24-27 October 2010, pp. 1437-1442.

2) <u>Sothea Kruy</u>[*], Hideki Aoyama, Kentaro Ohta, and Noriaki Sano, "Burr Prediction Method in End Milling," Proceeding of the 7th International Conference on Leading Edge Manufacturing in 21st Century, Matsushima, Japan, 7-8 November 2013, pp. 117-122.

3) <u>Sothea Kruy</u>[*], Hideki Aoyama, and Noriaki Sano, "Development of System to Predict and Minimize of Burrs in End-Milling," Proceeding of the 15th International Conference on Precision Engineering, Kanazawa, Japan, 23-25 July 2014, pp. 518-523.

4. Presentations at international conferences

1) <u>Sothea Kruy</u>[*], Mohd Hamdi Bin Abd Shukor, and Hideki Aoyama, "Development of Brick from Paper, Composite Wood and Plastic Waste Material," Proceeding of the 11th Asia Pacific Industrial Engineering & Management Systems, Melaka, Malaysia, 7-10 December 2010, pp. 1-3.

Presentations at international conferences:

Not applicable

Others:

Not applicable